Dry Manufacturing of Lithium-ion Battery Cathodes by Direct Powder Compaction in a Two-roll Calender

Zur Erlangung des akademischen Grades eines

Doktors der Ingenieurwissenschaften (Dr.-Ing.)

von der KIT-Fakultät für Maschinenbau
des Karlsruher Instituts für Technologie (KIT)

angenommene

Dissertation

von

M.Sc. Andreas Gyulai

Hauptreferent:	Prof. Dr. Michael J. Hoffmann
Korreferent:	Prof. Dr. rer. nat. Helmut Ehrenberg
Prüfungsvorsitz:	Prof. Dr.-Ing. Frederik Zanger

Tag der mündlichen Prüfung: 13.11.2023

Affidavit

I hereby confirm that this thesis is the result of my own work. All sources and/or materials applied and used in and for this thesis are listed and quoted. The statutes for Safeguarding Good Research Practice of the KIT have been respected and followed.

Furthermore, I confirm that this thesis has not yet been submitted as part of another examination process neither in identical nor in similar form.

Karlsruhe, 26.07.2023

Kurzfassung

In dieser Arbeit wird die direkte Pulververdichtung in einem Kalanderwalzwerk als alternatives trockenes Produktionsverfahren für die Herstellung von Lithium-Ionen-Batterieelektroden untersucht. Relevante Prozess- und Materialparameter, die das mechanische Verhalten der Pulver während der Verarbeitung beeinflussen, werden vorgestellt und anhand von Literatur aus der Pulvermetallurgie und Bodenmechanik qualitativ bewertet, um ein grundlegendes Verständnis für die Prozessgestaltung zu schaffen.

Die Prozessparameter wurden auf ihren Einfluss auf die mechanischen Vorgänge bei der Pulververdichtung und die daraus resultierende Elektrodendicke und Porosität untersucht. Zur Herstellung von Elektroden war eine Walzentemperatur erforderlich, die etwas unter der Schmelztemperatur des Bindemittels oder darüber lag. Das Schmelzen oder Erweichen des Binders ist notwendig, um eine ausreichende mechanische Festigkeit der Elektrode zu erreichen. Die anfängliche Walzspaltbreite hat sich als weitgehend irrelevant erwiesen. Ein niedriger, aber ausreichender Walzendruck ist erforderlich, um die notwendige mechanische Festigkeit der Elektroden zu erreichen, während ein hoher Walzendruck nur Nachteile in Bezug auf den Bruch des aktiven Materials und die geringe Porosität der Elektroden aufweist. Der Unterschied in der Umfangsgeschwindigkeit zwischen den Walzen wurde als der einflussreichste Prozessparameter identifiziert. Mit zunehmendem Geschwindigkeitsunterschied zwischen den Walzen konnte die Elektrodendicke deutlich im Bereich von über 1000 μm auf 80 μm reduziert werden, während die Porosität von ca. 20 % auf 35 % erhöht werden konnte.

Die Aufbereitung der Pulvermischung wurde als wesentlicher Prozessschritt identifiziert, um die reproduzierbare Herstellung von Elektroden mit verbesserter elektrochemischer Leistung zu ermöglichen. Die Deagglomeration des leitfähigen Kohlenstoffzusatzes durch intensives Mischen führt zu einer verbesserten elektrischen Leitfähigkeit in der Pulvermischung, die sich auf die resultierende Elektrode überträgt und die Leistung der Batteriezelle verbessert. Die Deagglomeration und homogene Umverteilung des PVDF-Bindemittels auf der Oberfläche des aktiven Materials verringert die innere Reibung in der Pulvermasse und verbessert die Verarbeitbarkeit beim Kalandrieren. Das Bindemittel erleichtert die Scherverformung der Pulvermasse, indem es unter hohen Druckbedingungen als Schmiermittel wirkt. Das Bindemittel bildet bei der Scherverformung Fäden, wodurch die mechanische Festigkeit der Elektrode erhöht wird, während gleichzeitig die Porosität zunimmt, was die Ratenleistung der resultierenden Elektrode verbessert. Die Deagglomeration und homogene Umverteilung sowohl des CB als auch des PVDF verbessern die elektrochemische Leistung der resultierenden Elektrode, aber auch die Schereigenschaften der Pulver, was eine vielseitigere und reproduzierbarere Herstellung von Elektroden ermöglicht.

Die schmierende Wirkung des PVDF-Bindemittels bei der direkten Kalandrierung von Pulvern wurde durch die Verwendung von Bindemitteln mit unterschiedlichem Molekulargewicht und unterschiedlicher Schmelzviskosität weiter untersucht. Eine Verringerung der Schmelzviskosität

des Bindemittels führte zu einer zähflüssigeren Reaktion des Pulvers auf Scherverformung, was zur Herstellung von dünnen Elektroden mit bis zu 30 µm Dicke und niedrigen Dichten von ca. 20 % führte. Die Verwendung von PVDF mit sehr hohem Molekulargewicht führte zur Bildung von PVDF-Filamenten zwischen den Aktivmaterial Partikeln. Diese Pulver zeigten einen höheren Widerstand gegen Scherverformung und führten zur Herstellung von Elektroden mit einer minimalen Dicke von ca. 30 µm, aber höheren Porositäten zwischen 28 - 35 %. Die Bindemitteleigenschaften haben also einen erheblichen Einfluss auf die mechanischen Eigenschaften der Elektrodenpulvermischung, und je nach den gewünschten Elektrodeneigenschaften muss die Auswahl des Bindemittels angepasst werden.

Schließlich ergab die Untersuchung des direkten Pulververdichtungsverfahrens eine komplexe Wechselbeziehung zwischen den Prozess- und Materialparametern, die die Schermechanik der Pulvermischung beeinflussen. Niedriger Walzendruck und hohe Geschwindigkeitsunterschiede zwischen den Walzen fördern die Scherverformung des Elektrodenpulvers und ermöglichen eine höhere Flexibilität bei der Verarbeitung. Durch die Verbesserung des Scherverhaltens der Pulvermischung durch den Einsatz von Materialien mit niedrigen inneren Reibungskoeffizienten oder niedriger Schmelzviskosität der Binder kann die Elektrodenbildung erleichtert werden. Diese Zusammenhänge können somit als Werkzeugkasten genutzt werden, um den Prozess entsprechend den gewünschten Elektrodeneigenschaften anzupassen.

Abstract

This work investigates the direct powder compaction in a calender roll mill as an alternative dry production process for the manufacturing of Lithium-ion-battery electrodes. Relevant process and material parameters influencing the mechanical behavior of the powders during processing are introduced and qualitatively evaluated using literature originating from powder metallurgy and soil mechanics to establish a basic understanding of the process design.

Process parameters have been analyzed for their influence on the mechanical processes during powder compaction and resulting electrode thickness and porosity. A roll temperature slightly below the melting temperature of the binder or higher was necessary to produce electrodes. Melting or softening of the binder is necessary to achieve sufficient mechanical strength in the electrode. Initial roll gap width has been identified as mostly irrelevant. A low but sufficient roll pressure is needed to achieve the necessary mechanical strength of the electrodes, but high roll pressure shows only disadvantages in terms of active material (AM) breakage and low electrode porosity. A difference in circumferential speed between the rolls has been identified as the most influential process parameter. With increasing speed difference between the rolls, electrode thickness could be reduced significantly in the range of over 1000 μm to 80 μm, while porosity could be increased from approx. 20 % to 35 %.

Powder mixture preparation has been identified as a significant process step to enable the reproducible production of electrodes with improved electrochemical performance. The deagglomeration of the conductive carbon additive by high-intensity mixing leads to improved electric conductivity in the powder blend, which translates to the resulting electrode, improving battery cell rate performance. Deagglomeration and homogeneous redistribution of the polyvinylidene fluoride (PVDF) binder on the active material surface reduces the internal friction in the powder bulk, improving processibility during calendering. The binder facilitates the shear deformation of the powder bulk by acting as a lubricant under high-pressure conditions. The binder forms filaments upon shear deformation, increasing the mechanical strength of the electrode while also increasing the porosity, and improving the rate performance of the resulting electrode. The deagglomeration and homogeneous redistribution of both, the carbon black (CB) and PVDF improve the electrochemical performance of the resulting electrode, but also improve the shear properties of the powders, enabling a more versatile and reproducible production of electrodes.

The lubricating effect of the PVDF binder in direct powder calendering has further been investigated by the use of binders with varying molecular weights and melt viscosities. A reduction in binder melt viscosity led to a more viscous response of the powder upon shear deformation, resulting in thin electrodes of down to 30 μm and low densities of approx. 20 %. The use of PVDF with very high molecular weight led to the formation of PVDF filaments between the active material particles. These powders showed higher resistance to shear deformation and resulted in

electrodes with a minimum thickness of approx. 30 µm but higher porosities between $28 - 35$ %. Thus, the binder properties significantly influence the mechanical properties of the electrode powder mixture, and depending on the desired electrode properties, the selection of the binder has to be adjusted.

Finally, the investigation of the direct powder compaction method revealed a complex interrelation between the process and material parameters that influence the shear mechanics of the powder blend. Low roll pressure and high speed differences between the rolls promote the shear deformation of the electrode powder, enabling higher versatility during processing. By improving the shear behavior of the powder blend through the introduction of materials with low internal friction coefficients or low binder melt viscosity, the electrode formation can be facilitated. These interrelations can thus be used as a toolbox to adjust the process according to the desired electrode properties.

Table of Contents

List of Figures

List of Tables

Preface

This dissertation was created during my work as a research associate at the Institute for Applied Materials (IAM) at the Karlsruhe Institute of Technology (KIT) and contributes to the research work of the Center for Electrochemical Energy Storage (Celest) of Karlsruhe and Ulm. The successful completion of this work was only possible due to the positive and productive environment in the research group for Energy Storage Systems (ESS). Therefore, I want to thank all the colleagues, students, and partners, who were part of this environment and accompanied me on my way.

My special thanks go to Dr. Werner Bauer, the group leader of the ESS research group, who was my supervisor during the completion of this work. He has always left freedom and encouraged me to conduct my research work the way it appeared best to me while offering advice and guidance whenever needed. I also want to thank Dr. Marcus Müller for all the discussions that helped the progress of this work and his steady help in the laboratories.

I thank Prof. Helmut Ehrenberg for the possibility to work at his Institute and conduct my work leading to this dissertation. I also thank Prof. Michael Hoffmann from the Institute for Applied Materials – Ceramic Materials and Technologies (IAM-KWT) for taking over the examination of this work.

My final thanks go to my colleagues in the research group of the ESS. They not only helped me with the many productive discussions we had but also made working in the group very enjoyable and fun.

Karlsruhe, July 2023,

Andreas Gyulai

1 Introduction

The on-road transportation is the only sector predicted to increase in greenhouse gas (GHG) emissions in the future due to a significant increase in passenger vehicle fleet until 2050 [1]. Nevertheless, already in 2019, it accounted for 28.8 % of total energy consumption and 25.8 % of GHG emissions in the EU [2]. Therefore, the incentive to replace combustion engine vehicles with electric vehicles, which can be powered by renewable energy, is high and drives the demand for energy storage solutions, especially for the high energy density Lithium-Ion batteries [3]. With the production capacity steadily increasing, cost reduction and energy savings during the production of batteries remain an important topic despite the many advances that have been made in recent years [4].

The standard electrode production method is a slurry-based coating process with the use of liquid solvents, which have to be evaporated and recycled in a consecutive drying step [5]. Although many developments in the process have led to significant improvements in product quality, throughput, and cost reduction [4, 6], electrode production still accounts for up to 25 % of total battery cell production costs [7] of which $19-22$ % are due to the highly energy intensive solvent evaporation and recovery step [8]. In an effort to further decrease costs and improve sustainability in electrode production, alternative manufacturing methods have been investigated that avoid the use of liquid solvents, reducing material costs and rendering drying and solvent recycling obsolete [6, 9].

Several approaches to dry electrode manufacturing processes exist, such as the electrostatic spray deposition of the electrode material on the current collector [10-14] or uniaxial compaction methods [15-17]. While their disadvantages and benefits will be discussed, the method used and investigated in this work is the direct powder compaction using a calender roll mill [9, 18, 19]. With a simple and continuous process design, low equipment requirement, and high potential for upscaling by upnumbering, direct powder calendering is one of the most promising dry processes [9]. Not only is the solvent and its evaporation avoided but equipment and plant space can be significantly reduced. Challenges yet to overcome in direct powder calendering, that prevent its large-scale application in industry, are the inferior electrode quality compared to slurry-based electrodes and difficulties achieving good reproducibility [9]. The reduction of the process design to a single powder calendering step makes electrode formation for multicomponent battery materials a very complex task. Thus, a better understanding of the powder calendering process is necessary to further develop the method, making it competitive with slurry-based methods in terms of product quality.

Since direct powder calendering is a quite new approach to electrode manufacturing, literature on this exact topic is limited. Therefore, in this work literature from powder metallurgy and granular mechanics is reviewed to establish a basic understanding of the macroscopic and mi-

croscopic processes during powder compaction in a calender roll mill. Process and material parameters are introduced and their influence on the mechanical behavior of the powders during compaction is evaluated qualitatively. Subsequently, the direct powder calendering method has been experimentally investigated.

First, the influence of the process parameters of a two-roll mill on the electrode properties has been investigated. According to the electrode properties, the conclusion could be drawn on the mechanical behavior of the powders in dependence of the investigated process parameters. Second, the influence of electrode mixture preparation in terms of dry powder mixing has been investigated. By the variation of mixing intensities, electrode powder blends have been prepared with varying degrees of additive deagglomeration and distribution. Differences in the mechanical behavior and processibility, as well as the electrochemical performance of the resulting electrodes, have been analyzed. Third, the influence of the binder material properties has been investigated. Differences in melt viscosity and molecular weight have been analyzed and correlated to powder blend processibility and the resulting electrode morphology. Finally, this work concludes with highlighting the major process and material parameters influencing the direct powder calendering process. Practices on how to utilize process parameters and material selection for process design and resulting electrode morphology are suggested.

2 Theoretical Background

In this chapter, the theoretical background for all relevant topics concerning this work is reviewed and summarized. Lithium-Ion-Battery structure and functionality are summarized to give a rough understanding of the role of the different battery components and their influence on the battery performance. The state-of-the-art electrode manufacturing process is introduced with its benefits and disadvantages. The summary of these topics is done quite briefly since they are typically well known to most of the readers. More detailed investigations on the processes inside a LIB or works about different chemistries are referenced for the interested reader. Moving on from this baseline, dry electrode manufacturing, which is the main subject of this work, is presented. Various dry manufacturing methods are reviewed for their benefits, disadvantages, and fields of application. The herein-detailed investigated method of direct powder calendering is then introduced. Following a summary of the method's history, a detailed analysis of the process is presented. The mechanical processes taking place in the material during processing are summarized and evaluated with respect to all possible process parameters, material parameters, and additional influences through feed material preparation. The interrelation of these parameters is qualitatively presented and their influence on process and product characteristics is given. This part of the presented work spans from topics such as pure mechanics, granular shear, and tribology up to polymer rheology. Therefore, the evaluation of the relevant parameters and their influence on the microscopic processes during dry electrode manufacturing are presented mostly qualitatively in the just necessary detail. The given references should give a good starting point to further deepen the understanding of the specific parameters.

2.1 The Lithium-Ion-Battery (LIB)

2.1.1 Fundamentals

A lithium-ion battery is a secondary battery, where Lithium ions are the charge transferring ions in the applied battery chemistry. While the chemical composition of a LIB can vary, they are made of five main functional components, the cathode, anode, separator, electrolyte, and cell case. Depending on cell format complementary parts such as spacers and springs are used to provide the necessary mechanical stability of the main components. Fig. 1 schematically represents a typical LIB in a coin cell and pouch cell format.
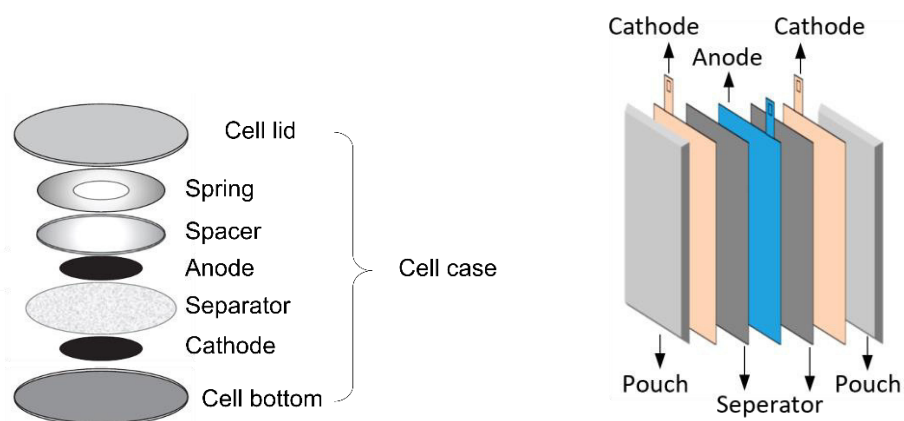
Fig. 1: Components and schematic of a coin cell (left) [20]. Schematic of stacked electrodes in a pouch cell (right) [21].

The cathode and anode form the main body of a LIB. They consist of the electrochemically active material (AM), which are the hosts for the lithium ions. They are the reactants for the characteristic redox reaction for the lithium intercalation. The electrodes are connected to metal foils as current collectors, that are in contact with the cell case, enabling electric charge transfer between the electrodes if an external device provides the connection. Inside the cell, the electrodes are separated by an electrically insulating separator, avoiding short-circuiting of the electrodes. Finally, the cell interior is filled with electrolyte. This liquid is ionically conductive and allows the migration of the positively charged lithium ions between the electrodes during charge and discharge of the battery cell. The spring and spacer are parts used in coin cell formats to maintain and evenly distribute the pressure on the electrodes. The cell case dimensions, as well as the used active material for the cathode and sometimes the anode, can vary significantly from battery to battery, but the cells always consist of these five main components [22].

The charge transfer mechanism by which a battery functions as an energy storage system is governed by the two redox reactions taking place at the cathode and anode of the battery. For rechargeable lithium-ion batteries typically intercalation active materials are used. Here, the positively charged lithium ions are either intercalated into or released from the active material crystal structure following a rocking chair mechanism. The electric charge that is either needed or is released by the redox reaction is transferred through the external connection between the cathode and anode, where the electric consumer or the charging device is connected. In parallel, the positively charged lithium ions migrate through the electrolyte and separator to the other electrode where the reduction of the lithium ions can take place. During charging, in most typical LIBs, the reduction takes place at the graphite anode. During discharge, the reduction of the Lithium ions takes place at the cathode, respectively. The exact reactions are strictly dependent on the used active materials and their standard free Gibbs energy, which also determines the voltage of the generated current. The mechanism is displayed for a system consisting of a $LiCoO_2$ cathode and graphite anode in Fig. 2 and the reactions are summarized for a generalized metal oxide cathode and graphite anode in equations 1-3, where M represents the metallic species [22, 23].
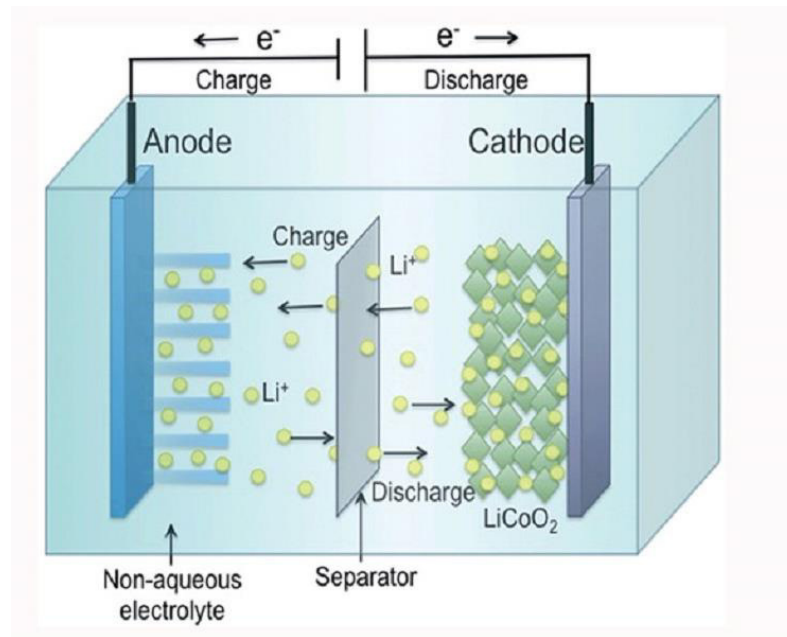
Fig. 2: Schematical display of the charge transfer mechanism during electric charge and discharge of a LIB [24].

Cathode charge reaction: $\quad LiMO_2 \quad\qquad\qquad \rightarrow\ Li_{1-x}MO_2 + x\,Li^+ + x\,e^-$ (1)

Anode charge reaction: $\quad C_6 + y\,Li^+ + y\,e^- \rightarrow\ Li_yC_6$ (2)

Overall charge reaction: $\quad LiMO_2 + \frac{x}{y}C_6 \qquad \rightarrow\ \frac{x}{y}Li_yC_6 + Li_{1-x}MO_2$ (3)
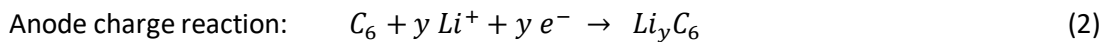
The energy (more precisely potential), that is necessary to charge the battery, thus, to intercalate the lithium ions into the anode, is governed by the standard free Gibbs energy of the redox reaction couple. On the other hand, the same energy (in case of minimal overpotentials) is released during the discharge of the battery. Therefore, a high difference in standard free Gibbs energy between the cathode and anode reaction offers the potential to store more energy [22].

2.1.2 Electrode Structure

The electrode layer on the current collector is typically made of three main components: the electrochemically active material, an electrically conductive additive, and an adhesive binder. The AM is as previously described the host of the lithium ions. The charge transfer reaction takes place upon intercalation of the Lithium-ion into the crystal structure of the AM. The electrically conductive additive is introduced to the system, to electrically connect the separate AM particles with each other and finally to the current collector. By this, an electrically conductive pathway is established that enables the delivery of electrons to the reaction sites where the charge transfer takes place. The materials used as conductive additives are mostly carbon blacks (CB) and graphites with very low particle size and/or high surface area. Finally, the adhesive binder is added to the electrode to form a mechanically stable connection between the AM, conductive

additive, and the current collector [6, 25]. A schematic representation of such an electrode is presented in Fig. 3
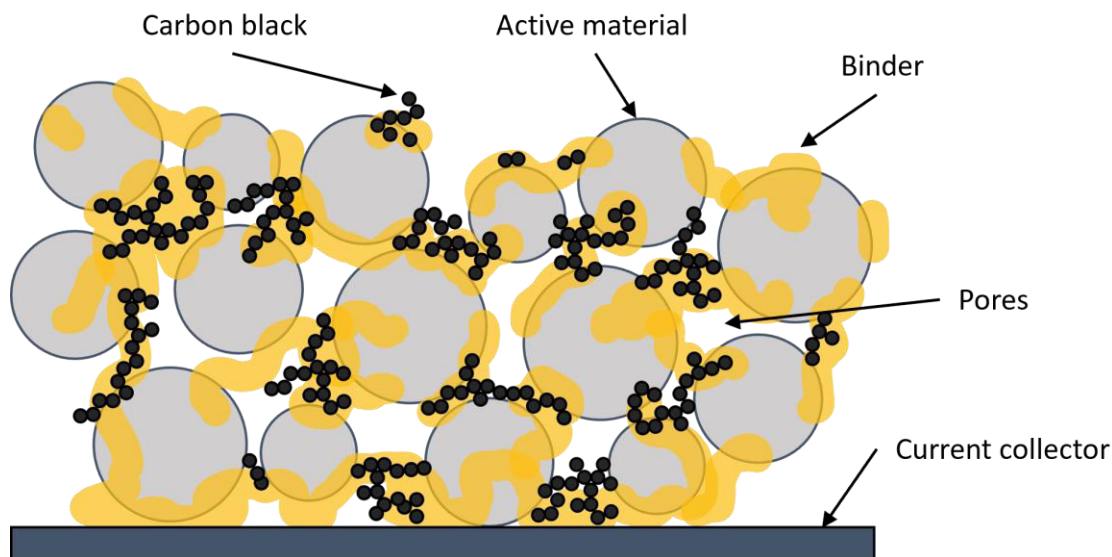
Fig. 3: Schematic representation of an electrode structure with AM, CB, and binder on a current collector.

While many polymeric binders are electrically insulating, by the incorporation of the conductive carbon in the binder a so-called carbon-binder domain (CBD) is established. With a sufficient and well-distributed amount of conductive carbon, this network is rendered electrically conductive, while supplying mechanical strength to the particle bed. Parallely, the typically high surface area of the CB soaks up and occupies a high amount of binder, reducing the availability of the binder to connect the AM particles. The introduction of high amounts of conductive CB and binder is leading to the reduction of the porosity, reducing the ionic conductivity in the electrode layer. Therefore, a balance in the used amount of CB and binder is necessary to offer high mechanical strength as well as sufficiently high electric conductivity [26].

2.1.3 State-of-the-art Electrode Production

All main cell components are essential and heavily influence battery performance, therefore all of them have been intensively researched in recent years. In this work though, only the electrode manufacturing and its state of the art is evaluated since the focus of this work lies on this specific process step.

The standard manufacturing method for electrodes is a slurry-based coating process, that has been optimized for many years but has remained almost unchanged in terms of process design [5]. A schematic representation of the process is given in Fig. 4.
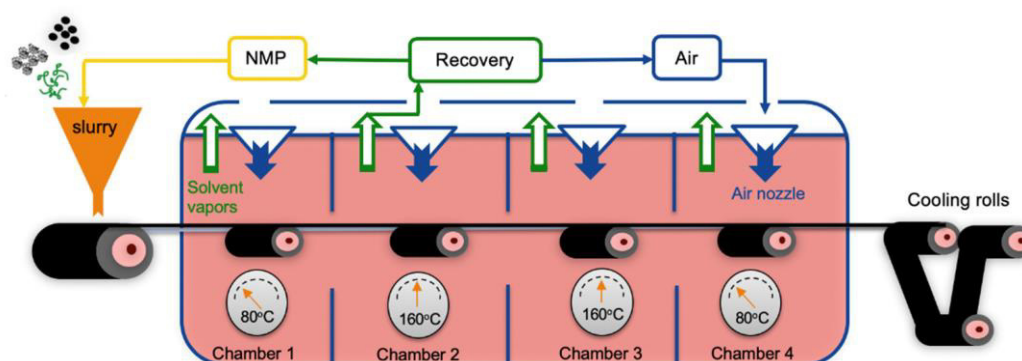
Fig. 4: Schematic representation of standard slurry-based electrode coating including drying and winding [6].

The process starts with the preparation of the slurry, where the polymeric binder is typically dissolved in an organic solvent, most commonly toxic N-Methyl-2-Pyrrolidon (NMP), to improve and homogenize its distribution in the slurry [5]. Then, all the solid components are dispersed in the polymer solution, resulting in a viscous slurry. Either by slot die extrusion or by doctor-blade casting this slurry is coated onto a current collector in a roll-to-roll continuous coater. The coater is followed by a convector drying oven, where the solvent is evaporated, and the coating is dried [6, 27].

This process design has been optimized to reduce manufacturing costs, improve quality, and finally increase production speed [27]. The highest electrode quality is achieved with slot die coaters, where process speeds between 30 m/min to 100 m/min can be achieved [5, 28]. At such high conveying speeds, long drying ovens are necessary to evaporate the solvent at an uncritical speed, avoiding defects such as crack formation or binder migration [29]. The major disadvantage of this technique is the requirement of often toxic solvents for the dissolution of the binder and the high energy consumption due to the necessary evaporation of the solvent [8]. While much work has been done to substitute the toxic organic solvent with aqueous systems, these solutions remain slightly inferior in product quality and do not reduce the intensive energy input for drying [30, 31]. For very efficient high-capacity battery cell production plants, the drying of the electrodes still contributes 19% of the total energy consumption for battery cell production [32]. At smaller production scales, the electrode drying energy can even account for 48% of the total required energy of battery cell production [33]. Therefore, alternative electrode manufacturing methods such as the dry production by direct powder calendering have received increased attention in the last five years. They allow the removal of the liquid solvents, thus also the energy-intensive drying step, leading to significant cost reduction in electrode manufacturing [8].

2.2 Dry Electrode Manufacturing

With the strong economic motivation to reduce electrode production costs by removing the energy-intensive drying step in standard electrode manufacturing processes, many different approaches to solvent-free processes have been attempted. They each have their disadvantages

and challenges, as well as their benefits, which make them viable solutions for the production of specific electrode types. Therefore, in the following, the major dry manufacturing methods are shortly presented with their benefits, disadvantages, and their typical field of application to give an overview of the possibilities in dry electrode manufacturing. This aims to provide the reader with a state-of-the-art overview of dry electrode manufacturing.

2.2.1 Electrostatic Spray Deposition (ESD)

Electrostatic spray deposition (ESD) is probably the most investigated dry electrode production method up to date [9]. Depending on electrode composition the particulate components are premixed in either a single-step or multi-step approach to homogenize the mixture and establish the desired distribution of CB and binder in a homogeneous particle blend [12, 34]. Then, the powder is fluidized by a fluidized bed, pneumatic conveying, or similar method and is conveyed through an electrostatic spray gun. Here, the particles become electrically charged by a strong electric field in the gun nozzle, from which they are sprayed onto the current collector [6, 9, 34]. The initial adhesion between the particles and the current collector is achieved by their opposite charge caused by the electrostatic gun and serves only as a way to homogeneously distribute the material and fixate it on the current collector. This primarily soft coating has to undergo a consecutive tempering step to activate the binder, thus improving the cohesion in the electrode layer and its adhesion to the current collector [34]. This step is similar to a standard calendering step with the exception of the use of rolls heated above the melting temperature of the binder. By melting the binder and the additional densification of the electrode layer, proper contact between the particles and the now liquid binder, as well as to the current collector is established to achieve a good adhesion, cohesion, and low contact resistance [34]. A schematic representation of the method is shown in Fig. 5.
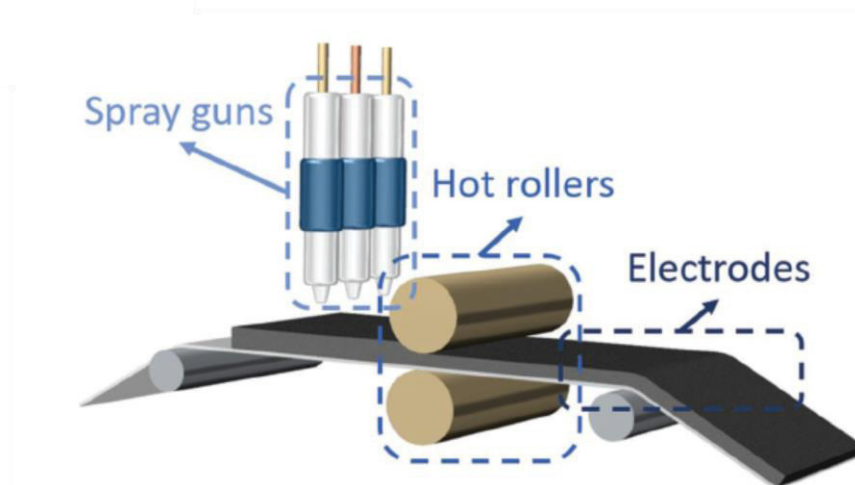
Fig. 5: Schematic process setup of an ESD coating line with subsequent hot rolling of the electrode for adhesion maximization [14].

This method has received the most attention of all the dry electrode processing methods due to the similarity of the resulting electrode microstructure when compared to conventional slurry-based electrodes, especially regarding the thickness, porosity, and pore microstructure [9]. While the absolute values for the thickness and porosity can be controlled quite precisely with ESD, a major difficulty is in achieving the necessary homogeneity [12]. With the powder mixture being a multicomponent mixture of very different types of materials (metal oxide, polymeric binder, low-density conductive carbon), homogeneous charging of the powder in the electric field of the spray gun nozzle proves to be difficult [12]. Further on, a more homogeneous distribution onto the current collector is necessary [35]. Additionally, difficulties in the upscaling of the process lie in maintaining a constant material flow through the spray gun nozzle due to clogging of the very cohesive and partly polymeric powder blend. Thus, spray coating is limited to low process speeds so that an upnumbering of spray guns would be necessary to obtain speeds that are competitive to slurry-based methods [6]. Furthermore, a high explosion risk is generated due to the aeration of the fine particulate and carbonaceous system.

2.2.2 Extrusion

Extrusion describes a process, where material is typically pressed through a sort of die by the application of high pressures. Related to electrode production, most commonly twin-screw extruders are used [36]. The screws consist of small elements, that can be precisely designed and adjusted to fulfill specific tasks during the extrusion of the material. The material feed can be premixed to achieve sufficient homogeneity or can be mixed during extrusion by the use of specifically designed screw elements that promote shearing [37]. The implementation of convection and high shearing zones is possible, making it a very versatile, but also complex method of processing. This versatility has made extrusion a very important and sophisticated method used in many industry applications and has gained more attention in battery production as well [36, 38, 39].

It has been introduced to slurry-based electrode manufacturing in slot-die coating, where recent developments enabled the reduction of the solvent content by 50%. Thus, electrode production efficiency in terms of costs and solvent usage could be improved. Nevertheless, subsequent drying steps are still necessary, excluding this application from dry electrode manufacturing [39, 40].

Further on, the production of solid-state battery (SSB) electrodes is a common application of extrusion, where the plasticity of the melted solid polymer electrolyte facilitates the extrusion process significantly and a high volume content of the electrolyte is needed. In general, the method leads to electrodes with a high density, low porosity, and the potential for particle breakage [39, 41]. Also, the volume content of the plasticizing material has to be sufficiently high to reduce friction during extrusion, thus potentially reducing the energy density of the electrode. These consequences are mostly beneficial for SSB electrodes but are disadvantages for typical liquid electrolyte-based electrodes. Other than that, melt extrusion is used commercially for the production of solid polymer electrolytes that are used for SSBs [42, 43].

Very recently, the use of completely dry materials has been investigated in extruders, where typically polytetrafluoroethylene (PTFE) is used as the polymeric binder in the electrode composition. Here, the ability of the extruder to achieve high shear forces in the particulate system is used to finely fibrillate the PTFE and distribute it in the particle mixture. In this case, the extrusion process substitutes other dry mixing methods, such as jet mills, to introduce high shearing into the particulate system [44]. In a second step, typically direct powder calendering in a roll mill, the powder is compacted to a thin film. The fibrils then can form a fine network in the particulate system, giving high mechanical strength to the electrode. This method is still under development and not much information is available yet on the produced electrodes [19, 45]. Nevertheless, in these cases, the extrusion is a preparative step and not the electrode manufacturing method. Whether this powder mixture can be directly processed to an electrode through a die is yet to be investigated.

2.2.3 Direct Powder Compaction

A variety of methods can be included in this category, where the used materials as well as the final application of the electrode can vary significantly. Albeit these methods have in common, that at least one material component undergoes either melting or pressure sintering to form a mechanically stable electrode body. Which material is to be melted in the respective process varies and strictly depends on the melt properties, that are needed to realize the electrode manufacturing process. These processes form a wide palette of methods, where some of them differ only minimally in terms of process steps, used materials, or the resulting electrode application [17, 35, 41, 46-48]. Although these changes can be minimal, the final application of the methods can vary significantly but concerning their advantages and disadvantages, they can be viable methods for their respective purpose. In the following, major powder compaction methods are presented that are generally investigated for the production of electrodes used in standard or SSB cells.

Uniaxial Compaction

In uniaxial compaction, or often called hot pressing, the powder mixture is typically premixed, then pressed batch-wise under high pressure to form a thin electrode layer or a pellet of a certain shape using a die. The process is schematically displayed in Fig. 6. With changing temperature and pressure, a wide range of material compositions can be formed to electrodes. The most common use of the method is the production of SSB electrodes with solid polymer electrolytes, that typically have low melting temperatures and high plasticity [16, 47, 48]. Since the polymer electrolyte is to substitute the liquid electrolyte in the final battery cell, it is aimed to replace the porosity in the electrodes, thus the volume content of the polymer typically lies between 20 and 50 vol.% [16]. With a relatively low melting temperature of the polymer and a good plasticity of its melt phase, the polymer facilitates the pressing process so that it is easy to form very dense and low porosity electrodes with hot pressing [35]. If the volume content of soft materials is low, AM particle breakage often reduces electrode quality Therefore, this method is disadvantageous for the production of electrodes with higher porosity [35].
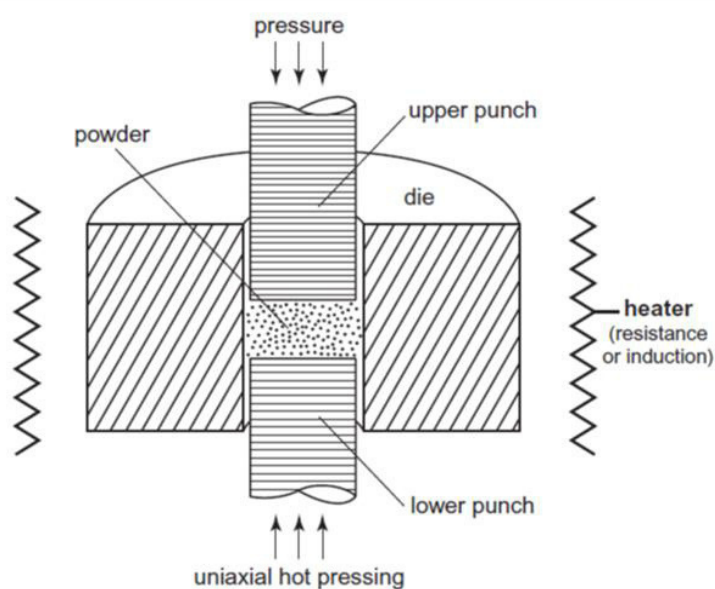
Fig. 6: Schematic process design of hot pressing with a heated die [49].

The same method can be applied at high temperatures (>600°C) for material compositions with ceramic electrolytes or standard electrode compositions comprised of metal oxide active materials. In this case, sintering of the active materials takes place, which results in good contact between the particles and high mechanical strength of the electrode. While ceramic electrolytes with sufficiently high diffusion rates are possible, a combination of good ionic diffusion rates and high electric conductivity is the main challenge of SSB electrodes of this category [50, 51]. Hot pressing and sintering of standard compositions without the use of solid electrolytes additionally has the disadvantage, that maintaining a high porosity for the liquid electrolyte is difficult. Attempts have been made to retain high porosity by introducing polymeric binders or wax-like materials to the green body that can be burned out during the sintering step [46, 52]. However, the use of such sacrificial materials as processing aids contradicts the primary goal of reducing material costs and energy consumption since it would be equivalent to using liquids as solvents and lubricant, thus no economic benefit is to be expected. Additionally, a high energy input is necessary for the sintering of the materials, while the process speed is limited to batch processing speeds.

While hot pressing and sintering methods are economically and qualitatively disadvantageous for the manufacturing of porous electrodes intended for standard battery cells, the method is beneficial for the production of solid polymer electrolytes, where no porosity is desired and low temperatures are sufficient to enable the plastic deformation of the electrode material blend [15].

<u>Direct Powder Calendering</u>

With this method, premixed electrode powders are continuously compacted between two rolls of a calender to form a thin electrode layer. While it is a compaction method where either melting of the binder or sintering of other materials is necessary, the process has no uniaxial character, thus introduces more complex mechanical processes to the compaction of the powder. This method has been increasingly adopted in research and industry for the manufacturing of LIB electrodes [9, 19, 53]. Since direct powder calendering is the investigated method of this work, it is introduced in high detail in the following.

2.2.4 Direct Powder Calendering

Direct powder calendering or roll milling generally describes a process where a material is brought through a gap between two cylindrical rolls. The device used is called calender and is essentially the same as a roll mill. The use of calenders or roll mills is spread through many different industrial applications. The nomenclature of calendering and roll milling often changes between their different fields of application. The first uses of roll mills were for the milling of sugarcane or grain [54] or later the milling of rocks and agglomerates in the mining industry [55]. While these applications relate to the name by the process of milling, thus downsizing of a material, in more advanced applications of roll mills this relation is not anymore given. Roll mills were introduced to fabric production [56], papermaking [57], and later to metal foil [58] and plastic foil fabrication [59]. These processes do not follow the aim of milling a material down to smaller sizes, but to compress the material fed through the roll mill gap. In fabric production and papermaking, a densification of the material is achieved through which the thickness of the product can be adjusted and the surface gets a smooth finish, while additives such as glue are more efficient due to increased contact with the fibers [60]. In metal and plastic foil production the use of a roll mill is often accompanied by a heating step prior to the roll mill gap. The metal or polymer typically enters the gap as a melt phase and is then plastically deformed in the roll mill gap to a certain shape or thickness [61, 62]. These processes often include several pairs of roll mill cylinders through which the material is fed to achieve the final shape or thickness. According to these applications, a separation into size reduction processes, which are called roll milling, and other shape-giving processes, which can be referred to as calendering can be made. Although this distinct separation would be possible, in modern literature and also industry, the use of calender and roll mill became interchangable, so that one might be misled when first being introduced to one of these processes. While calendering is typically used in papermaking and polymer foil production, the expression of roll milling is used often in metal shaping or foil production processes.

A more recent application of roll milling is the calendering of battery electrodes, which became a standard process step in the slurry-based electrode production process [63-66]. The slurry-based electrodes exit the drying step typically with a porosity between $40 - 60\,\%$ and potentially have an uneven surface morphology due to inhomogeneities caused during solvent evaporation [29, 64, 67]. Thus, a calendering step is introduced after the drying of the electrodes to densify

the electrode layer and to reduce surface roughness for a more homogeneous electrode thickness. This process has been analyzed in several works for its benefits and disadvantages. It was found, that not only the energy density of the electrodes was increased but also the adhesion to the current collector and the electric conductivity was improved through better contacting between the conductive carbon additive aggregates throughout the carbon binder domain [63, 67]. Also disadvantages, such as crack formation, stress build-up through the electrode and in some cases, delamination through stress propagation have been reported [67-69]. Although the calendering of slurry-based electrodes has still some room for improvement, the process is quite well understood and is generally considered a standard process to improve the electrochemical performance and energy density of electrodes.

Using roll mills to compact powder directly to electrodes is a new approach originating from powder metallurgy, where metal powders were compressed to form green bodies for metal plates and films [70]. A translation of the method from powder metallurgy to electrode manufacturing seems reasonable due to similar process design and educt and product morphology but is not easily done due to the increased complexity of electrode material composition, as well as specific morphological demands of the final product, e.g. composite layer thickness and porosity [67]. While calendering is typically used for either downsizing of particles or densification of the feed, in the case of electrode manufacturing both effects must be precisely controlled since active material particle breakage is to be avoided and very specific demands for the final electrode porosity are desired [67]. Additionally, the powder feed is a complex mixture of components with very different morphologies and properties [64], such as various active materials, high surface conductive CB, graphite, various polymeric binders, and potentially other additives, which all can influence the behavior of the powder feed during compaction in the calender gap, thus affecting the whole manufacturing process [9, 71, 72].

The first attempts to use direct powder calendering for the manufacturing of battery electrodes have been made by Maxwell Industries, that has been acquired by Tesla in 2018 to repurpose their direct powder calendering technique from supercapacitors to LIB electrodes [53]. In parallel, Robert Bosch GmbH and Fraunhofer IWS developed and patented techniques for electrode manufacturing by direct powder calendering [18, 19]. Technology solutions such as Drytraec® by Fraunhofer IWS show the possibilities of direct powder calendering, but there is a big gap in understanding the process, due to a lack of scientific and published work on the topic. The relationship between material parameters, process parameters, and electrode morphology and performance has not been systematically investigated, and almost no real data on functioning electrodes have been published [73].

To advance this method to a state, where it becomes competitive with slurry-based methods in terms of product quality, a thorough understanding of the powder calendering process is necessary. Therefore, this work investigates direct powder calendering for electrode manufacturing in a high detail, to gain a better understanding of possible influencing parameters. This begins with the understanding of the mechanical processes during powder densification in the calender

gap including all the influencing process parameters, which is addressed in the following chapter. Once a basic understanding of the process is gained, further influencing parameters such as material morphology and properties, state of the powder mixture, and binder characteristics are investigated, and resulting electrodes are electrochemically characterized.

2.3 Roll Compaction Theory

The main process taking place during direct powder calendering is the compaction of the powder in the roll mill gap. While at first glance it seems to be easily explained, it turns out to be a very complex process to understand in the necessary detail for dry electrode manufacturing. A subdivision of the compaction process into macroscopic and microscopic processes is necessary to investigate the different parameters and influences of the equipment and used materials. Therefore, first, the compaction process is described macroscopically with the introduction of the compaction and friction forces acting on the bulk of the material. This involves the explanation of several simplifying assumptions, that are necessary for a macroscopic view. After a critical evaluation of these assumptions, it becomes obvious, that the processes taking place in the powder bulk cannot be explained by macroscopic effects only, thus a microscopic view into the process becomes necessary. The main processes of interest are the shear mechanics of the powder, as well as cohesion and potential particle and agglomerate fracture. Therefore, process and material parameters are investigated separately for their influence on the mechanical processes inside the powder bulk. Due to the multitude of parameters, their complexity, and the different scientific fields of origin, most parameter influences are described only qualitatively in this section. The parameters, that could be investigated with the existing equipment, have been analyzed in this work and are presented in the results and discussion of this work.

2.3.1 Mechanics in the Roll Mill Gap

The mechanical analysis of the powder calendering process originates mainly from powder metallurgy in the 1960s [58, 72, 74], where compaction is the main goal of the process. Attempts have been made to establish methods to calculate and predict the forces acting on the powder feed, the corresponding compaction of the material in terms of strip thickness and density, as well as plane stresses and pressure distribution along the roll surface [74-76]. Typically, a small volume element of the powder in the calender gap is analyzed and several other simplifications have to be assumed to find a solution to the calculations of the compaction process. In Fig. 7, a cross-section of such a volume element is presented with its characteristic parameters and the forces acting on it. The mechanical fundamentals are briefly explained and an attempt to find a solution from previous literature is reviewed. The exact derivation of the mechanics of these attempts is not discussed in detail, since, at a closer look at the necessary simplification, they are not applicable to the powder calendering in electrode manufacturing [72]. Nevertheless, a qualitative understanding of the acting forces, and especially the reasons why certain simplifications cannot be made are key factors in understanding the powder calendering process to an

extent, where the influence of process and material parameters can be understood and used to enable a successful calendering process for electrode manufacturing.

The assumptions and simplification made in literature when analyzing the mechanics of direct powder rolling are the following [71, 74, 77-79]:

1. The powder bulk is treated as a continuum in the nip zone (equal pressure distribution, $\frac{\partial P}{\partial x} = 0$).
2. Roll mill rigidity is infinite
3. Temperature and friction coefficients are constant.
4. Mass forces and inertia are negligible compared to applied pressure and friction forces
5. Steady-state compaction in plane strain – no changes over time and constant roll strip width ($\frac{\partial u_i}{\partial t} = 0$; $u_z = 0$).
6. Planes in the powder bulk perpendicular to the feed direction always remain parallel to each other. $\frac{\partial u_y}{\partial x} = 0$. (Minimum surface inclination, no shearing)
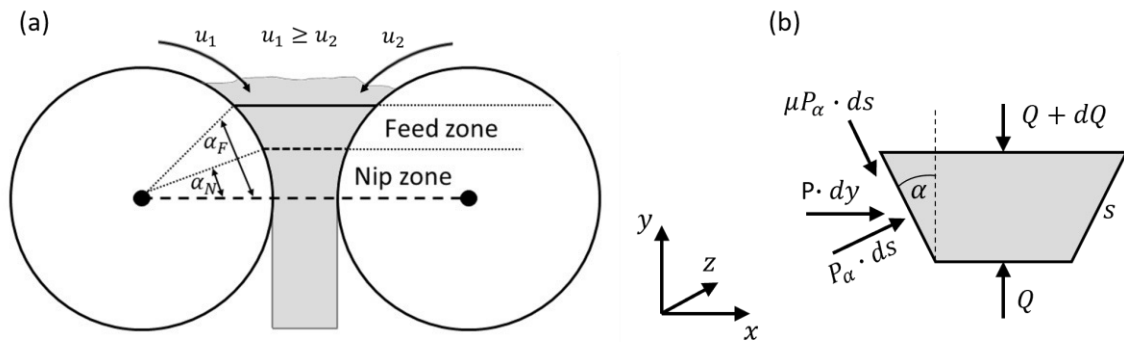
Fig. 7: Schematic representation of the powder calendering process (a) and of the acting forces on a simplified volume element (b).

Fig. 7 shows a two-roll mill with vertical powder feed and a free body diagram of a volume element of the powder in the nip zone of the roll mill gap. The simplifications allow the transformation into a two-dimensional problem. The powder material is fed vertically into the roll mill gap, the two rolls of the mill rotating in opposite directions with circumferential speeds u_1 and u_2 (for now $u_1 = u_2$). Two zones are typically defined for the compaction process, the feed zone between the angles α_F and α_N and the nip zone between α_N and the exit of the roll mill gap [58, 72, 80]. In the feed zone, the powder particles are gripped by the roll mill surface through friction forces and are pulled along the circumference of the roll towards the exit of the roll mill gap ($y = 0$). In the feed zone, densification of the powder bulk only takes place through the rearrangement of the particles due to relative movement, thus the resulting density at the interface between the feed and the nip zone is the tap density of the powder [72]. As the powder enters the nip zone, relative movement of the particles is not observed anymore. Instead, pure compaction of the powder takes place by introduction of pressure forces to the powder bulk, which is treated as a continuum in the nip zone [72]. The calculations done in the literature to

describe the compaction process strictly focus on volume elements in the nip zone. After the simplifications, the only acting forces on the volume element are introduced through the static friction between the roll surface and powder particles and the stresses introduced by the pressure of the roll surface, as shown in Fig. 7(b). A force equilibrium in y direction and compaction forces in x direction can be formulated as follows.

Simplified force equilibrium in y-direction:

$$dQ = 2(-\mu P_\alpha \, ds \, \cos\alpha + P_\alpha \, ds \sin\alpha) \tag{4}$$

Simplified force equilibrium in x-direction:

$$P \, dy = \mu P_\alpha \, ds \sin\alpha + P_\alpha \, ds \, \cos\alpha \tag{5}$$

Here, Q is the resistance of the powder against compaction in y-direction, μ is the friction coefficient between roll surface and powder, P_α is the roll pressure perpendicular to the roll surface, s is the length of the volume element and P is the absolute roll pressure. Thus, the main forces during compaction are the compaction forces due to the roll pressure, the friction forces between the roll surface and the powder, and in specific cases the forces needed to maintain constant feeding.

Based on these force equilibria, given the simplifications mentioned earlier, the calculation of many process and product parameters has been attempted and models have been developed [74-76, 80]. The derivation of these models can be found in the given literature but is not further discussed, because they are not applicable for the direct powder calendering process used in this work. Since pure compaction is not desired for electrode manufacturing, where a reasonably high strip porosity is required, process and material parameters are adjusted to minimize the nip zone in the roll mill, thus, maximizing the feed zone. The calculations done in previous works focus strictly on processes in the nip zone, additionally, the assumptions and simplifications have to be reviewed in context of the updated calendering process. Quickly it becomes obvious, that a translation of the derived calculations to electrode calendering is not applicable. For this, the simplifications shall be reviewed one by one in detail.

1. *The powder feed is treated as a continuum*

    Battery powders have a fine particulate size, typically below 20 µm. A powder bed as it exists in the roll mill gap thus consists of millions of individual particles. These can vary in size, shape, surface morphology, and even chemistry or crystal structure [71, 81]. Additionally, the battery powder mixtures often vary in composition, including high surface area CB, polymeric binder, graphite, and a wide range of active materials [64]. Assuming such a powder bulk to behave as a continuum is the most critical assumption that literature from metallurgy has adopted to be able to calculate the mechanical processes taking place during compaction. The immediate consequence of this assumption not being valid, is, that the powder bed in the roll mill gap cannot be regarded as one volume element, but as a bed of millions of individual

particles [71, 82]. Although the main forces exerted by the calender can still be regarded macroscopically, the way they are transferred into the particle bed has to be regarded microscopically. Forces acting on the particles at the particle-to-roll surface interface are not simply transferred through the whole particle bed, as it would be for a continuum. With particles having an unknown shape and morphology, the transfer of forces from interface particles to bulk particles cannot be precisely predicted, since the direction of force transfer is unknown [82]. Thus, typically forces dissipate through the particle bed in all directions, causing higher stress buildup in the interface region compared to the bulk [79]. Whether the particle bed consists only of interface zones is dependent on particle size, gap width, and height of the particle bed [83].

2. Infinite roll mill rigidity

While no device can have infinite rigidity, for the application of roll mills in battery electrode production this assumption is fairly realistic. The constructors of roll mills aim to achieve high rigidity since the devices are designed for compaction processes. They typically have a high mass, exert high forces on the material, and withstand high material resistance forces. In battery electrode manufacturing the compaction of the powder feed is to be controlled to a necessary minimum to achieve sufficient mechanical stability of the electrode while not reducing porosity too much. Therefore, the resistance forces of the material that are transferred from powder bed to the rolls is significantly lower than the forces for which the roll mill was originally designed. As long as compaction of the battery powder is held to a minimum, and the roll mill is designed for compaction processes, this assumption is acceptable. Once a powder mixture undergoes increased compaction, by either process design or accidentally by wrong parameterization, this assumption does not hold (as can be observed by the widening of the gap width).

3. Temperature and friction coefficients are constant

This assumption has to be reviewed in every single case of process application individually. Process temperature in dry electrode manufacturing can vary from room temperature, to above the melting temperature of polymeric battery components (>150°C). Depending on the material characteristics in terms of heat conduction and transfer, as well as the residence time of the powder in the roll mill gap and the corresponding compaction, a constant temperature in the particle bed can be assumed. Especially if small roll mill gap widths are used and the powder material is preheated from its residence time in the feeding zone.

As friction coefficients decrease with increasing pressure until they reach an almost constant value [84, 85], the estimated pressure onto the powder bed is the deciding factor, whether constant friction coefficients can be assumed. Since prediction or calculation of the nip zone and the pressure distribution in the particle bed are difficult, and direct

measurement of friction conditions in the calender gap is difficult to conduct, this assumption needs further investigation. During strong compaction, where it is certain that the powder bed is under high pressure, the assumption seems applicable, but especially at minimal compaction, or in the shear zone, where particle shearing is promoted and almost no pressure acts on the powder, this assumption is heavily under question [72]. A precise understanding of pressure evolution in the transition zone between shear and nip zone is necessary to finally evaluate the validity of this assumption.

4. Mass forces and inertia are negligible

For particles at the roll surface interface and in close proximity to it, this assumption is acceptable. Friction forces and pressure in these regions are significantly higher than mass forces and inertia [79, 81]. Inertia might become more relevant for the process design at very high roll speeds if the refilling of the roll mill gap with the powder feed takes place by gravity only. If the material in the nip zone is carried out of the gap at a mass flow which is not achieved by gravitational feeding, other solutions for the feeding of the powder must be introduced to avoid gaps and holes in the resulting electrode.

5. Steady state over time and in z-direction

A steady state particulate flow over time is a critical assumption in general. While processes with particulate flows aim to achieve a steady state, due to the inhomogeneity of particle systems this is difficult to achieve. Stress build-up and release, particle breakage, and adhesion to the roll surface are only some of the possible local phenomena, that can take place to hinder the development of a steady state [86]. For well-understood and designed processes, a periodic semi-steady state can be typically achieved [81]. While the process is not entirely in a steady state, periodically the process is reset to a certain baseline, either automatically by beneficial material characteristics or by the introduction of a small maintenance process (e.g. the periodic cleaning of a sieve by pressurized air pulses or by the introduction of vibration). In dry electrode manufacturing much of the research has been done in a batch-wise process design, but attempts are made to transform the powder compaction into a steady-state process [19]. With further improvements, a steady state over time can possibly be achieved, but for now, the assumption has to be reviewed critically.

A steady state in z-direction, thus in the width of the electrode strip can typically be assumed, if the roll milling process includes a feed control so that powder enters the gap at a constant width. If the process is well parameterized for the used powder mixture, meaning only minimal compaction takes place (no widening of the gap) and effects like stress buildup and release take place only periodically, a constant electrode width can be achieved. While particles will be pushed to the sides of the electrode during compaction and some will fall uncontrollably out of the gap at those sides, the final width of the electrode strip remains constant or subject to the periodic nature of the mechanical processes, respectively.

6. *Planes in the powder feed perpendicular to the feed direction always remain parallel to each other.* $\frac{\partial u_y}{\partial x} = 0$*. (Minimum surface inclination, no shearing, no kinetic friction between roll surface and particle*

This assumption is strictly bound to the nip zone of the calender, where no relative movements of the particles are expected but full compaction. And even there, assuming no particle breakage or rearrangements is questionable [72]. In the case of electrode manufacturing with a roll mill, the process aims to decrease the compaction zone and maximize the shear zone, where relative particle movement is desired and shearing is promoted. Although this assumption can potentially be valid for the nip zone, due to the specific process design in dry electrode manufacturing and the increased focus on the shear zone, this assumption is not valid. Because of this, the calculation of particle shear, pressure distribution, and other processes during roll milling is hardly possible.

Now that the process of powder calendering is described macroscopically, the major forces are introduced and the assumptions and simplifications are reviewed, it becomes clear, that calculations done in previous works in the field of metallurgy, although they offer a basic understanding of the mechanical processes, cannot be simply transferred to electrode manufacturing in roll mills. Especially the minimization of the nip zone and the focus shifting to the shear zone differentiates the electrode manufacturing process from regular roll mill compaction. Additionally, the need to regard the powder bed as a sum of many individual particles introduces several material parameters to the process, that must be accounted for. Therefore, it is beneficial to review the process and material parameters for their influence on the newly presented application of roll milling. In the following, a detailed review of these parameters and their influence is given for the same process design as depicted in Fig. 7(a).

2.3.2 Influence of Process Parameters

Process parameters include all the parameters and quantities, that are adjustable by the equipment used in the process. Since a single two-roll mill is used in this work, only the calender parameters are of interest in this part. These include the mill rigidity, roll diameter, roll speeds u_1 and u_2, roll pressure, roll temperature, and initial gap width. All parameters are evaluated qualitatively. Furthermore, the influence of the roll speeds, pressure, temperature, and initial gap width have been analyzed quantitatively and are presented in the results and discussions of this work.

2.3.2.1 Mill Rigidity

The rigidity or more often stiffness of a physical body describes its resistance to deformation or displacement under an applied force [87]. The highest force during calendering is the compression of the rolls under their hydraulic pressure, and their counterpart, the resistance of the material against this compression [76]. These two forces are acting opposite to each other. Since compaction of the powder is kept modest in dry electrode manufacturing, the compression forces used in this work are low compared to typical calendering processes. The rigidity of the

used equipment is designed for higher compression forces, thus machine rigidity plays no significant role during this work, as long as compaction is limited. In case the resistance becomes higher than the compression forces, the powder is already strongly densified and the electrode thickness is increasing due to an opening of the calender gap width [72]. In these cases, the rigidity of the equipment becomes relevant and has to be accounted for. For roll mills with very high rigidity, an increase of the gap width during processing is typically no concern but particle breakage can occur. For roll mills with low rigidity, gap width opening becomes more prominent. In any case, due to the typically high but still finite rigidity of the mill rolls, changes in process pressure always result in small changes of the initial gap widths [88]. Therefore, a correction of initial gap width is necessary for every change in process pressure.

2.3.2.2 Roll Diameter

The roll diameter is a process parameter not easily changeable, due to the necessity of the installment of a new set of rolls. Additionally, the high mass of the rolls often defines the dimension of the calender in terms of size, but also motorization. Therefore, typically the roll diameter is a given parameter or has to be determined before roll mill construction. Thus, understanding the influence of the roll diameter is crucial for the correct design of the process. Fig. 8 illustrates the roll milling process for two different roll diameters with the same roll gap width.
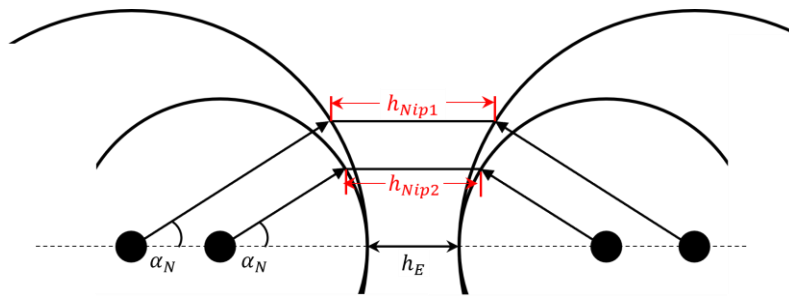
Fig. 8: Schematic representation of the rolling process with different roll diameters

For the same materials and equal circumferential speed of the rolls, the gripping angle α_N, which determines the beginning of the nip zone, is a constant value. Therefore, the volume element undergoing compaction becomes wider with increasing roll diameter as the width of the nip zone is increasing for higher roll diameters with $h_{Nip1} > h_{Nip2}$. Due to much higher material width at the beginning of the nip zone, the material has to undergo increased compaction, but has a longer compaction time due to the higher roll circumference. Since the final gap width h_E is not a constant value, but the compression force of the rolls, this results in a more even compaction process that can lead to an increased strip thickness due to the opening of the roll mill gap by the internal resistance of the material during strong compaction [72].

Since this process parameter could not be analyzed in this work due to the availability of only one set of rolls, it can only be assumed, that in the case of dry electrode manufacturing a low roll diameter is beneficial for the process. Here, a minimization of the nip zone is desired, and

high compaction rates of the powder could lead to increased shearing due to more rearrangements of the particles [89]. On the other hand, it could promote local phenomena such as stress buildup or particle breakage. An additional disadvantage of small roll diameters is the significantly reduced rigidity of the calender, that could lead to inhomogeneous strip thickness. Therefore, a high stiffness of the machine should be maintained even when using small rolls.

2.3.2.3 Roll Pressure

The hydraulic pressure on the bearing of the calender rolls is the roll pressure. It directly translates to the line load that the roll surface exerts on the material at the roll-to-particle bed interface. Depending on the material properties and the position in the gap zone, this pressure either dissipates rapidly in the shear zone or is transferred through the particle bed to establish a force chain network in the nip zone [71]. The resistance of the powder against compaction and deformation acts opposite to the roll pressure and is transferred from the material to the roll surface. This resistance of a powder against compaction increases very rapidly, once a critical compaction (tap density) is achieved [72], due to the necessity of elastic and plastic particle deformation for further compaction [71, 76]. Since only minimal compaction is desired, low roll pressures are beneficial for dry electrode manufacturing to allow the rearrangement of particles and reduce the stress build-up in the transition to the nip zone. On the other hand, with constant gripping angles, the powder resistance can become greater than the low roll pressure. This finally leads to the bearing of the roll to give in, opening the gap width of the roll mill and finally increasing the electrode strip thickness. For a given powder mixture, once its tap density is achieved, an increase in roll pressure does not lead to a reduction in electrode thickness. Additionally, a slight increase in electrode density by plastic deformation of individual particles can be caused [72]. Thus, roll pressure is preferentially limited, to still enable slight compaction of the powder to guarantee mechanical stability of the electrode but to reduce compaction and densification to a desired extent without drastic plastic deformation of the materials.

2.3.2.4 Initial Roll Gap Width

The roll gap width describes the distance between the closest interfaces of the two rolls. Before the calendering process begins, typically an initial roll gap width is set up after the rolls are turning and roll pressure is applied, and before material is fed through the gap. The initial gap width is relevant, when the internal resistance of the powder towards compaction in the nip zone remains smaller than the compaction forces of the rolls and their corresponding roll pressure. Only in this case, an opening of the gap is avoided, and the final electrode thickness is similar to the initial gap widths. If the internal resistance of the powder against compaction exceeds the roll pressure, the gap opens until it reaches a steady-state width in which powder compaction resistance and compaction forces are in equilibrium. In this case, the initial gap width only sets the starting width of the process and has no effect on the final electrode thickness.

If an initial gap width is applied, the resulting electrode thickness cannot be significantly lower than the installed initial gap width, since the rolls cannot compress further than this selected width. A low initial gap width causes the powder in the gap to be compressed until equilibrium

between material resistance and roll pressure is achieved. Here, the material experiences exactly the selected compaction forces, that are set by the roll pressure, but the electrode thickness cannot be controlled directly. A third possibility is the selection of an initial gap width, that is similar to the desired electrode thickness. With the control of the other process parameters, such as the roll speed settings, the compaction can be reduced to avoid strong gap opening and to achieve the desired electrode thickness while still applying the set roll pressure.

2.3.2.5 Roll Speeds

In typical calendering processes the rolls are turning in opposite direction at equal circumferential speed to achieve homogeneous compaction of the electrode. In case of dry electrode manufacturing, to minimize the nip zone, the rolls are turning at different speeds, depending on the used material feed [19]. Thus, a separation of the absolute speed of the rolls, and relative speed between the rolls has to be made. In this work, from this point onwards, the absolute speed u_1 describes the circumferential speed of the fast roll, and the relative speed between the slow and fast roll is expressed as the ratio of $\frac{u_2}{u_1}$ (in %).

Assuming gripping of the particles at the roll surface due to high friction forces, the roll speed is the determining factor of the material throughput, together with steady-state gap width and electrode density [72]. An increase in roll speed leads to a higher throughput, limited only by the refilling of the calender gap by the powder feed. Thus, roll speed can only be increased as long as the powder feed is able to provide the necessary mass flow. Speeds higher than that lead to insufficient material compaction, thus a lack of mechanical strength and inhomogeneous electrodes with holes. On the other hand, very low roll speeds are always possible but promote compaction instead of particulate shear. While local stress build-up and release can be minimized, particulate shear is limited. For very homogeneous powder samples, which can distribute stresses through the powder bulk well by having good flow and shear properties, low speeds are beneficial due to the reduction of local phenomena. For powders with bad shear properties such local phenomena can cause the deagglomeration and rearrangement of particles, improving processibility at the cost of potential particle breakage [72, 83].

By turning the rolls at unequal speeds, the herein-described calendering process significantly differs from its typical application and changes the mechanics of powder compaction. The particles at the roll surface interface are pulled into the gap at different speeds. By friction to the next particle in the powder bed, thus force transfer from layer to layer, a speed profile similar to laminar flow in liquids is introduced [71]. While no linear speed profile is achieved as with liquids, due to the particles being discrete elements with inhomogeneous surface morphology, the exact speed distribution across the width of the gap is not predictable [86]. Nevertheless, by introducing this speed profile to the particle bed, shearing of the particles is strongly promoted [19]. With increasing speed difference between fast roll and slow roll, thus higher speed difference between neighboring particles, the establishment of shear planes tangential to the roll surface is promoted. Powders with high friction coefficients, thus bad flow properties, resist this shearing by strong friction forces, whereas powders with good flow properties shear at even lower speed differences between the two rolls [79, 90]. With shearing promoted to an extent,

that shear planes can develop in the powder bed during calendering, the nip angle and compaction zone are decreased. The shear zone, where particle relative movements are possible, is maximized. Thus, the process shifts from a compaction process to a shear process [72]. With the promotion of particle shear, it is now possible to achieve low electrode thickness due to the particles being able to rearrange. Additionally, higher porosity can be achieved due to the minimization of the compaction zone. Introducing this roll speed difference is one of the key applications enabling the production of porous electrodes with a roll mill, as it has been also lined out by previous investigations done on the topic [19].

2.3.2.6 Roll Temperature

The dry manufacturing of electrodes by direct powder compaction is a dominantly mechanical process, thus mechanical properties and parameters influence the process. The temperature has an influence insofar as some of the mechanical properties of the utilized materials are temperature-dependent. If this is the case, temperature can be a powerful parameter to significantly influence the whole compaction process. For example, the use of polymer electrolytes with a low melting temperature (as low as 60°C) [91] for the production of SSB electrodes introduces a material, that can undergo a phase transition and significantly change its mechanical properties.

In the case of typical LIB formulations, polyvinylidene fluoride (PVDF) is used as the polymeric binder, which is thus the most sensitive material towards temperature changes in such compositions with a melting temperature between 145 and 170 °C. The viscoelastic properties of the molten binder are taken advantage of in the dry manufacturing process, by using roll temperatures close to or above the PVDF melting temperature. By melting or at least softening the PVDF, the viscosity of the binder is reduced and is more easily distributed through the electrode bulk during calendering. This improves the distribution homogeneity of the binder and leads to increased mechanical strength of the resulting electrode layer.

Furthermore, the PVDF is processed in a liquid state, thus the electrode powder blend is not entirely solid and dry. The viscoelastic polymer has a lubricating effect during the shear deformation in the calender, which helps to promote shear and to increase the processibility of the electrode blend. In electrode manufacturing, this effect is unique to dry manufacturing but is significant for the successful realization of the direct powder compaction method. Therefore, temperature control coupled with the choice and utilization of the polymeric binder plays a key role in process design and will be investigated during this work.

2.3.3 Granular Friction and Shear

The evaluation of the influence of the process parameters makes clear, that in direct powder compaction shearing of the powder bulk is essential to obtain thin and porous electrodes. By the analysis of the process parameters the evolution of shear and nip zones in the calender gap can be better understood, but the microscopic mechanisms taking place in the powder during

the transit through the shear zone are not yet discussed. In this chapter, these mechanical processes during powder shearing are further discussed with respect to the material properties, that have a significant influence on the mechanical behavior of the particles.

It has to be noted, that the herein-discussed dependencies between material properties and granular shear are typically the subject in the fields of tribology, civil engineering, or soil mechanics. Many works have been conducted to investigate material friction, solid lubrication, and landslides, often with the help of complex simulations to derive methods for the calculation and prediction of shear behavior in granular materials. Although many advances have been achieved in recent years, helped by increasing computational power, a full understanding of granular shear could not be achieved due to the multitude of parameters and often microscopic mechanical processes. Thus, this work discusses general trends and only well-investigated dependencies between material properties and granular friction and shear flow. In a later stage, when discussing the results of this work, the used materials and their influence on their shear properties are evaluated concerning the here-described material properties.

For readers heavily interested in powder rheology, granular friction, or tribology, the presented literature gives a good basis for further literature search. Since this work is mainly aimed at battery researchers and manufacturers, a detailed analysis of these very mechanical topics cannot be given here [79, 81-83, 86, 90].

2.3.3.1 Shear Flow

Shear flow in a particulate system exists, when relative displacement between neighboring particles in a particle bed takes place, while these particles have at least one point of contact. Through this contact, the friction between the particles defines the shear force under a given normal load [92]. The simplest scenario of a particulate shear flow is the equivalent to liquid laminar Couette flow as shown in Fig. 9. A powder bed is filled between two plates, one of which is sliding at a constant speed U. A normal load F_N is applied onto the moving plate and the shear force F_S necessary to move the plate along the particle bed surface is recorded. A speed profile $\frac{\partial U}{\partial y}$ across the height of the powder bed can be observed. Due to the inhomogeneity of the particulate system, this gradient is not linear, in fact, a precise calculation of the gradient is hardly possible. Therefore, an undefined number of shear planes are established, at which the relative movements between particle layers take place [82].
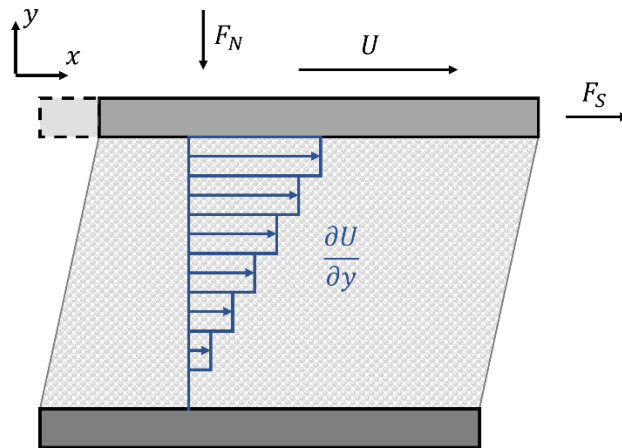
Fig. 9: Schematic representation of granular shear between two plates, similar to Couette flow

At this point, a differentiation between two cases has to be made. First, low friction at the boundary between the powder bed and the upper plate due to a very smooth plate surface and low material friction coefficient, or second, high friction at the boundary due to the high surface roughness of the upper plate. In the first case, the sum of the friction between particles at the boundary and the upper plate is lower than the friction between particle layers. This results in the sliding of the upper plate along the particle bed surface at the boundary, also called stick-slip [93]. The force transfer from plate to powder bulk by friction is not enough to introduce a speed profile into the particle bulk. No shear flow in the particle bed can be observed. With respect to the electrode calendering process, this case is detrimental for particle shearing, and thus is to be avoided in dry electrode manufacturing with a roll mill [94].

The second case is the relevant one and shall be discussed in more detail. Here, the friction between particles and the upper plate is higher than the friction between the particles at the roll interface and the next particle layer (speaking of particle layers is only vaguely correct since no perfect layer exists in the particle bulk). This causes the particles at the roll interface to move parallel to the direction of the upper plate, shearing along the next particle layer. Since these particle layers are not homogeneous, continuous discs, but are composed of many individual particles, a fraction of the particles in the second layer start to move in the direction of the first layer due to friction. This force transfer through the particle bulk leads to the development of a shear and speed profile through the height of the particle bulk similar to a liquid laminar flow profile [94].

The main acting forces are the applied normal load F_N onto the top plate and the shear force F_S needed to move the upper plate. The ratio between shear force and normal force is the friction coefficient μ_s or μ_k for the static or kinetic friction, respectively. For a sliding plate, the ratio of these measured quantities yields the friction coefficient between the plate and powder bulk. For a non-sliding plate, the internal friction of the powder is measured this way. Exemplary results of such a shear displacement measurement are shown in Fig. 10, where a powder bulk undergoes strain deformation at a constant strain rate and applied normal load [95].

$$\frac{F_S}{F_N} = \mu_s \text{ or } \mu_k$$
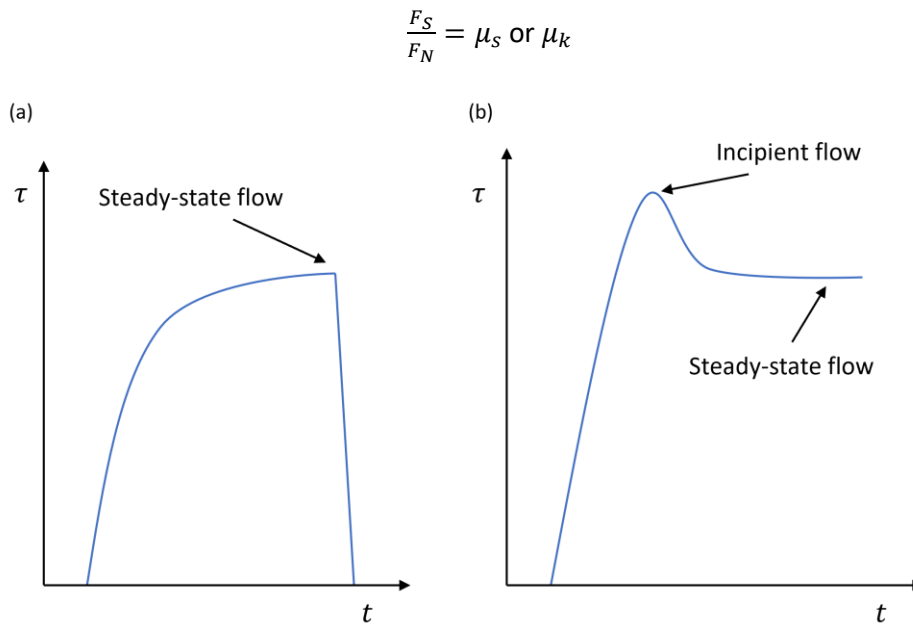
Fig. 10: Typical data obtained by shear flow measurements for unconsolidated powder samples (a) and pre-consolidated samples (b) [95].

With increasing time, the shear deformation is increasing linearly due to the constant strain rate. The shear stress τ is increasing first linearly with the strain deformation, then slows down until it reaches a constant value for unconsolidated samples. At this point, steady-state flow is achieved, which means that at least one shear plane has been developed somewhere in the powder bulk. The ratio between the applied normal force and the measured shear force and the applied normal force $\frac{F_S}{F_N}$ at this point is equal to the dynamic internal friction coefficient (DIFC) μ_k of the powder. When a preconsolidated powder is measured in the same way, the shear force increases linearly until it reaches a maximum. This point marks the incipient flow, at which plastic deformation of the powder bulk begins due to particle shear. The ratio between shear and normal force at this point equals the static internal friction coefficient (SIFC) μ_s of the powder. The shear force then decreases to a constant value, which again marks the steady-state flow, which is equal to the shear force measured for an unconsolidated sample of the same powder [95].

A preconsolidated powder has a higher density, and thus exerts higher resistance towards deformation due to stronger mechanical interlocking and higher cohesion forces. Therefore, the shear force needed to initiate plastic deformation of the powder bulk is higher than the measured shear force at steady-state flow, at which a shear plane has been developed inside the sample bulk. Also, this shear plane is the reason for both samples having the same shear force at steady-state flow. This value is characteristic for the internal friction of the powder and its specific shear plane.

The force distribution, that is developed during granular shear, is strongly dependent on the material properties of the sample. Several attempts to calculate and simulate these so-called

force chains have been made in literature [86, 90, 96-98]. Each of these attempts underlie a few assumptions, which reduce the complexity of the particulate system to allow the calculation of the force distribution. Therefore, calculated results only exist for systems with limited complexity, often single-component particle beds with specific particle shapes and friction coefficients. Nevertheless, they are helpful to understand how forces are distributed in the particle bed and the analysis of certain particle properties can be done with such simulations. Since they are often the basis for the analysis of some material properties, that are evaluated in the following chapters, a representative force chain distribution is presented in Fig. 11.
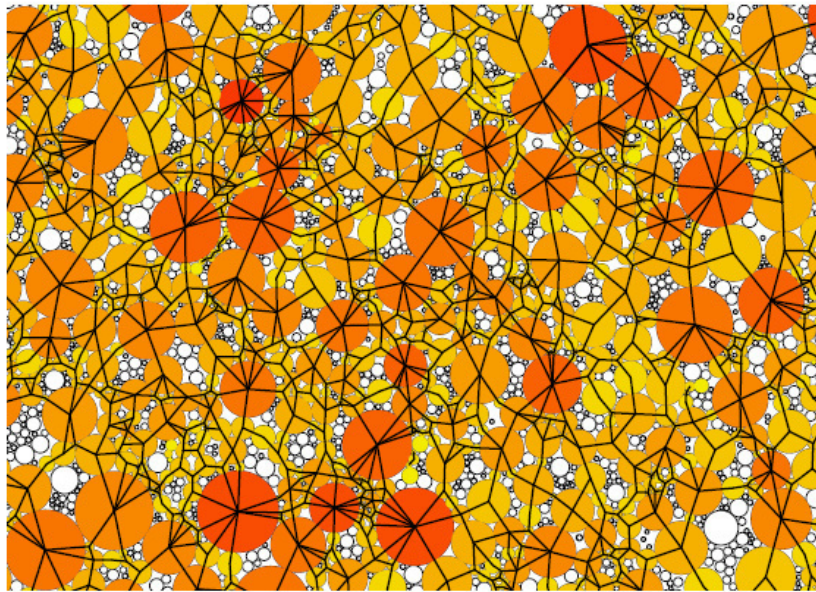
Fig. 11: Force chain distribution in a single component particulate bed of circular-shaped particles under an applied normal force [98].

The lines represent the direction of existing stresses inside the particles and the color of the particles represents their absolute value. White-colored particles experience no stress, instead, they lie loosely in the simulated particle bed. Large particles experience strong stresses more often than smaller particles, although exceptions exist. The inhomogeneous nature of the force chain distribution and pressure dissipation in a particle system leads to local phenomena such as stress build-up and release and plastic deformation of particles. These force dissipation through the particle bulk is the main difference between liquids and particulate systems that significantly increase their complexity [86, 90, 98].

As can be seen already in this example, many particle properties influence the evolution of such force chains and the frictional behavior during granular shear. Therefore, the most relevant particle properties are reviewed in the following concerning their influence on friction and finally their role in dry powder roll milling.

2.3.4 Material Properties

2.3.4.1 Particle Size and Distribution

The particle size of a particulate system is the first property one typically thinks of when characterizing a powder, thus is also the most investigated property in most powder applications. Nevertheless, the analysis of the frictional behavior of particulate systems with different particle sizes is challenging, since a change in particle size often induces a change in the particle size distribution or morphology of the particle shape. A simple downsizing of a certain powder not only leads to a smaller particle size but can change the shape of the particles as well as the shape of its size distribution. These properties have to be controlled, a powder has to be found that has the same material composition, size distribution, and particle shape so that only the absolute particle size is different. For such a powder system, the investigation of the direct shear in a shear cell is shown in Fig. 12.
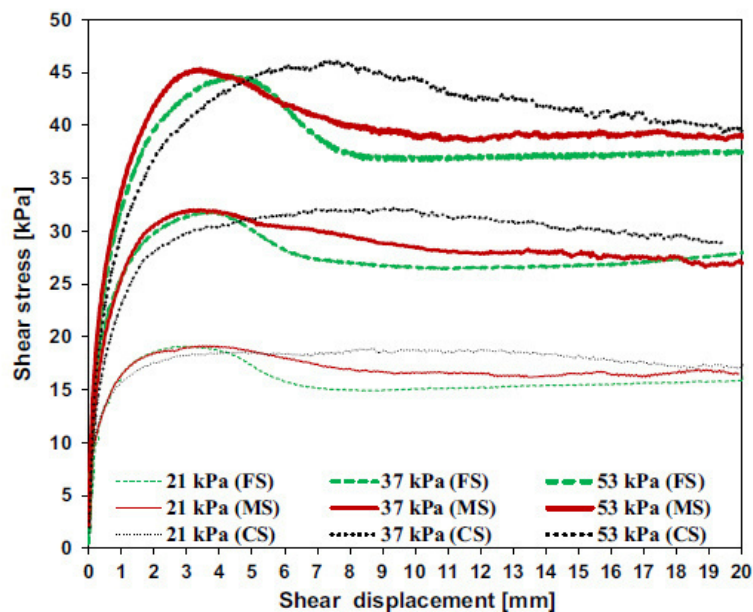
Fig. 12. Shear stress measurement of three different powders with different absolute particle sizes but similar size distribution at three different normal loads. (Fine sand, medium sand, coarse sand) [99]

For a specific normal force, no significant influence of the particle size can be observed on the absolute value of the shear stress at the yield point as well as the steady-state shearing. Differences can be observed only in the shear displacement or time needed to reach the yield point or the steady state shearing, respectively. With increasing particle size, both points need higher shear displacement to be reached, indicating a more homogeneous force chain development for small particle sizes [99].

2.3.4.2 Particle Size Distribution

For the investigation of the influence of particle size distribution on friction, simulations have been already extensively done for particle systems where the size distribution width as well as its shape were varied. A very good example is the work of Azema et al. [98]. Their generated particle size distributions and the corresponding particle-scale view under compression are shown in Fig. 13. The parameters b and s are design parameters for the construction of the size distributions. The simulative results for the friction coefficient of these size distributions are shown in Fig. 14 [98].
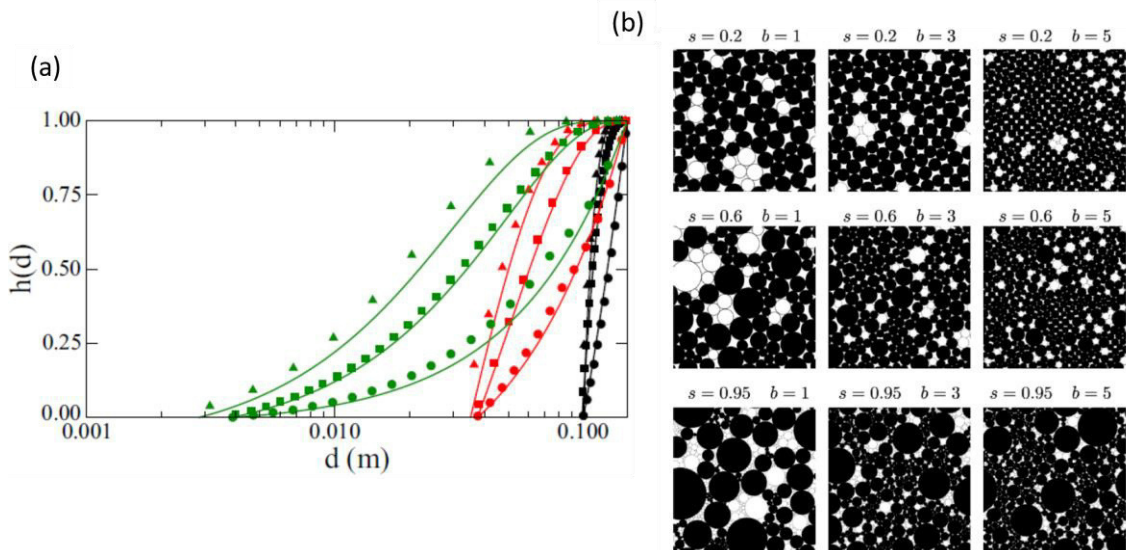
Fig. 13: Different particle size distribution for spherical particles used for the simulation of the friction coefficient, s = 0.2 (black), 0.6 (red), and 0.95 (green); and b = 1 (circles), 3 (squares), and 5 (triangles) [98].
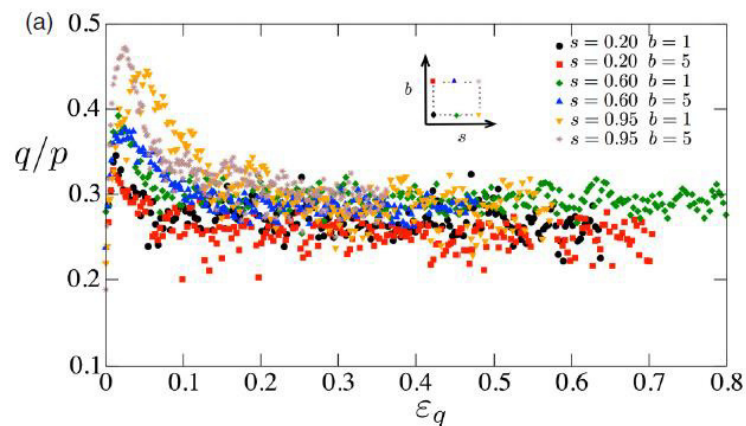
Fig. 14: Friction coefficients of the simulated particle size distributions [98].

The internal static friction coefficient $\frac{q}{p}$ (μ_s) , thus the shear force at incipient flow $(\varepsilon_q < 1)$, is high for powder beds with very wide particle size distribution, $s = 0{,}95$). The friction coefficient decreases for particle size distributions, that are narrower, as can be seen for the samples with

$s < 0.95$. The kinetic friction coefficient μ_k at steady state flow ($\varepsilon_q > 0.3$) is the same for all calculated samples. Therefore, the particle size distribution does not influence the macroscopic friction properties of a powder sample if it is in steady state. On the other hand, the particle size distribution does influence the force chain distribution. A more homogeneous or S-shaped size distribution has a more evenly distributed force chain network, with fewer particles experiencing extreme stresses as well as fewer particles floating without contact than other size distributions. A good visual comparison is represented by the simulation of the force chain networks of an S-shaped and a power-law-shaped particle size distribution in Fig. 15.
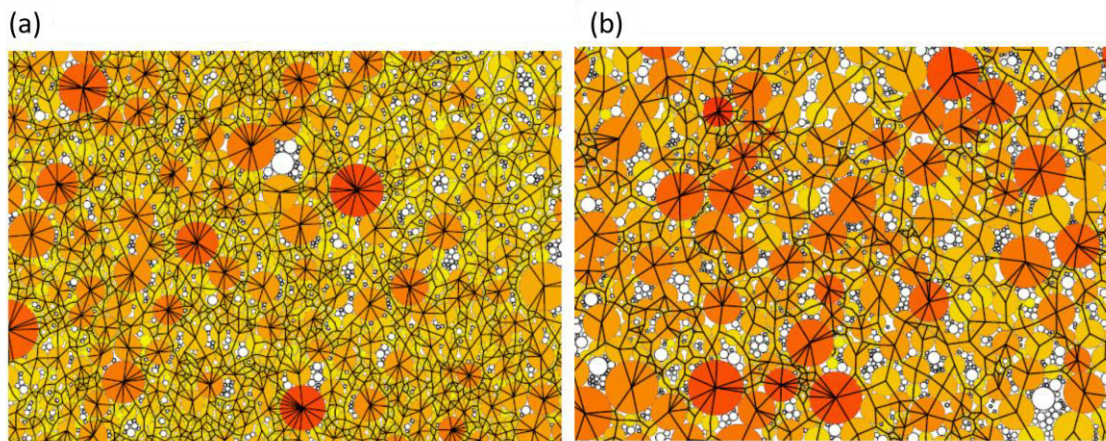
Fig. 15: Force chain networks for an S-shaped (a) and power-law-shaped (b) particle size distribution. [(s,b) = (0.9,1) (a) and (s,b) = (0.9,5) (b), respectively.] [98].

Therefore, in dry electrode manufacturing, the design of the particle size distribution can be a powerful tool to reduce local stress phenomena and prevent AM particle breakage. Additionally, by involving more particles in the force chain network, more binder-to-AM contacts can be potentially established, resulting in a higher mechanical strength of the electrodes. With this knowledge, synthesis or post-synthesis processes of the AM can potentially be adjusted to deliver beneficial materials for the dry manufacturing of electrodes.

2.3.4.3 Material Hardness

Material hardness describes the resistance of a material to localized deformation. Hardness is dependent on several material properties, such as ductility, elasticity, plasticity, etc, that are mainly influenced by the microstructure of the material [100]. In this work, a detailed analysis and explanation of hardness is not possible, although it is important for the roll milling process, as it influences the shear behavior of the granular flow especially at increased normal forces or very localized stress build-up. While it is likely irrelevant in the shear zone of the calender, where low stresses are applied to the particles, in the nip zone, where the normal force on the material increases rapidly, a high material hardness prevents plastic deformation of the particles. This is beneficial to retain the original shape of the AM particles. On the other hand, plastic deformation of the particle surface is a way of the particle bed to counteract local stress build-up, that impedes shear flow and can lead to particle breakage. A verdict on the influence of material

hardness in dry electrode manufacturing cannot be made at this point. To better understand the role of particle hardness, a detailed analysis of stress evolution and granular shear in the transition between shear and nip zone would be necessary. Nevertheless, the rough understanding of hardness is also relevant for material properties discussed in the next sections.

2.3.4.4 Particle Surface Roughness

Surface roughness is a parameter that describes statistical deviations of the surface height from a plane. For round-shaped particles, the plane would be the deconvoluted surface area of the sphere. In this case, the surface roughness describes the height differences that can be identified for this plane. As surface roughness indices are statistical, there is a variety of parameters, that describe the surface roughness. While they always describe height differences from the standard plane, they can have different weighting factors. The most common indices are the average roughness, the root-mean-square roughness, or the skewness [101].

Surface roughness has a major influence on solid shear mechanics, where high surface roughness leads to significant increases in friction coefficients [102]. Unfortunately, the analysis of surface roughness of a particle system is very challenging, due to the heterogeneity of the system [103] which is even increased by the complexity of material composition in the case of electrode manufacturing. Therefore, a quantitative determination of surface roughness and analysis of its influence on dry electrode manufacturing is not expedient or even possible. Nevertheless, a qualitative understanding of surface roughness can be beneficial for the selection of AM particle shape, if it is possible.

While the initial material friction at very low normal loads is subject to the chemical composition and crystal structure of the material, the bulk friction coefficient of the material can significantly differ depending on the roughness of the material surface [90]. The bulk friction coefficient of materials increases with increasing roughness due to the mechanical interlocking of surfaces, thus it influences force transfer during particle-to-particle shear [82]. The increase of bulk friction coefficient by high surface roughness is especially dominant for shear at low normal loads. With increasing normal load, and depending on material hardness, surface roughness becomes less dominant due to smoothening of the surface by plastic deformation [81].

Regarding the calendering process described in this work, a rough particle surface can impede granular shear in the shear zone, where very small normal forces are exerted on the material. In the transition to the nip zone, where the stresses start to increase rapidly, material roughness can potentially play a smaller role, given the material has a low hardness. Since the shear zone is aimed to be maximized in the calendering process, a high surface roughness is generally better avoided, but if strong compaction is desired, thus increasing the nip zone, high surface roughness can prove beneficial. In combination with low hardness, very high densification for solid-state batteries can be achieved [17].

For practical applications it is important to note, that surface area analysis is often taken into account for the evaluation of surface roughness due to the simplicity and availability of the measurement method. In fact, this correlation is a misconception and should not be applied for

the determination of surface roughness. The existence of pores, holes, and crevices in the particle structure can lead to significant increases in surface area, while statistically, the surface roughness is almost unaffected. Also, with different indices describing surface roughness, certain surface structures can result in high roughness indices, while a mechanical interlocking of surfaces is not promoted, thus the influence on the friction coefficient remains small or negligible. Thus, surface roughness remains a challenging parameter in the evaluation of its influence on dry powder processing.

2.3.4.5 Angularity

Like the surface roughness, the angularity of granular particles is a measure for the surface morphology of the particles. It is typically a measure for the number of corners of edges on the particle surface but can be also defined as a coordination number, indicating the number of contacts a single particle has with other particles [104]. It does not only directly influence the macroscopic friction coefficient during granular shear, but also influences whether particles purely shear or additionally rotate. These dependencies are shown in Fig. 16.
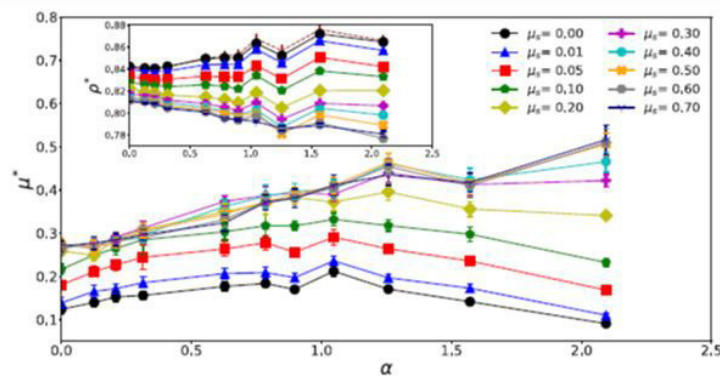
Fig. 16: Simulated evolution of the macroscopic friction coefficient with increasing angularity for materials with different local friction coefficients [90].

An increase in the macroscopic friction coefficient for increasing angularity can be observed, when the local friction coefficient of the material is at least higher than 0.20, which is typically the case for most solid materials, especially metallic materials [105]. The fact, that simulative works predict a decrease of macroscopic friction coefficient with increasing angularity for samples with low local friction coefficients is very interesting and needs further analysis, but is not important for the herein discussed application, since such low local friction coefficients are not realistic for the herein used materials. For local friction coefficients higher than 0.3 the increase of macroscopic friction coefficient with angularity is almost independent of the local friction coefficient [90].
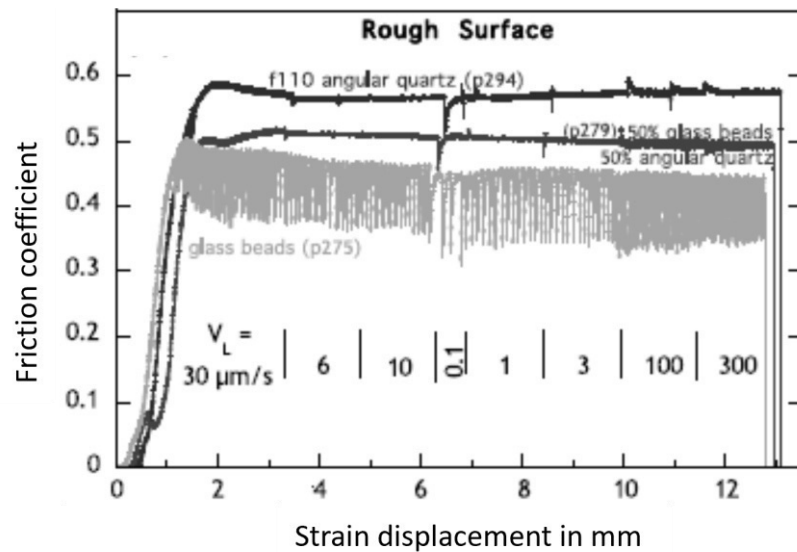
Fig. 17: Powder shear measurement of circular, angular, and mixed quartz particles [94].

A study by Anthony et al. [94] investigated the influence of particle angularity on particles with rough surfaces. The results of shear displacement experiments are in Fig. 17. The macroscopic friction coefficient for angular particles is significantly higher than for round particles. On the other hand, shearing of the round particles results in very strong stick-slip behavior caused by localized stress build-up and release. By mixing angular and round particles, local stress build-up is avoided while the macroscopic friction is slightly increased. It was concluded, that instead of pure shearing, thus strong local volume expansion during particle rearrangement, rotation of the particles is possible. This reduces local stress build-up and stabilizes steady-state shearing [79, 94]. Therefore, particle angularity can be a useful tool to stabilize granular shear for active materials with rough surfaces or high friction coefficients. If an angular material is introduced to the particle system, that has a lower friction coefficient than the used active material, the disadvantage of further increasing the friction by introducing angular particles can potentially be minimized (as is the case for the lubricating graphite).

2.3.4.6 Water Content and Humidity

The dry electrode manufacturing process does not include the use of liquids but does not necessarily exclude the relative humidity of the process atmosphere, as well as the initial water content of the materials used, which can significantly vary according to the hygroscopicity of the used materials. When water-sensitive active materials are used in the process, water content and humidity are often precisely controlled to avoid material deterioration. But in the case of a simple process setup where such protective measures do not have to be applied, humidity can still influence the process by affecting the intraparticle forces during granular shear. This influence was intensely investigated in the past due to its importance to geomechanical processes, but final results are often contradictory. The better-understood mechanisms are shortly discussed in this work but are not applied in the evaluation of the generated data, since high processing temperatures allow the assumption, that humidity can be neglected.

The existence of water at particle-contact joints can induce hydrolytic weakening of the material. This is a water-assisted plastic deformation that can enhance defect and dislocation migration in the material crystal structure, finally leading to plastic deformation and increased contact areas [106, 107]. This reduces particle roughness at contact junctions, potentially leading to a reduction of friction coefficient, thus reducing shear strength [106]. Effects such as pressure dissolution can take place, where surface layers dissolve under increased pressures, changing the friction coefficient of particle contact junctions [107]. This can be relevant for active materials, that have been exposed to humidity during their lifetime and could develop surface layers by reacting with humidity in the air. Whether pressure dissolution increases or decreases shear strength depends on the resulting contact chemistry and area, therefore, it is nearly impossible to predict. Finally, by liquid bridging, humidity can significantly increase the cohesion of a material. This plays a role, especially at normal forces close to zero, where cohesion is the dominating force rather than friction. High cohesion can impede the development of granular shear in the calender shear zone, where almost no pressure of the rolls is transferred to the material.

A final verdict on whether humidity has a beneficial effect on the process in terms of reducing material shear strength is impossible to give in general. Judging from the experience of this work, a fast investigation of the influence of humidity on each material system is the most efficient solution, if the influence of humidity cannot be neglected due to the applied process design.

2.3.4.7 Deagglomeration and Delamination

Deagglomeration and delamination are essentially similar to particle breakage. But while active material particle breakage is to be avoided, materials can be introduced to the powder mixture, that can easily deagglomerate or delaminate during granular shear. By this, stress buildup in the force chain network can be reduced by the material rearrangement after particle breakage. The introduction of such materials in the form of conductive additives can be electrochemically beneficial or even necessary to improve electrode quality and performance [108]. The conductive CB additive initially comes in the form of agglomerates, that first have to be deagglomerated to enhance its conductive property, thus this deagglomeration can be made use of during granular shear [108]. Similarly, graphite is often used as a conductive additive, that improves long-range conductivity through the electrode layer. Graphite with laminar structure is well known to be a solid lubricant and is often used in additive manufacturing or mechanical processing to reduce friction and wear on solid surfaces [109]. Since these are standard materials in electrode manufacturing, good use can be made of their lubricating properties and beneficial effects on granular shear.

2.3.5 Polymer Viscoelastic Shear

The polymeric binder additive used in the electrode composition differs from the other solid materials in terms of mechanical properties. Although the polymer has a similar, round particle shape and size compared to the other materials, the difference lies in the intraparticle structure of the polymer. The polymer particles consist of many entangled molecules that can form random amorphous arrangements up to very crystalline structures. Polymer properties such as chemical composition, branching, and molecular weight strongly influence the intraparticle structure of the molecules, resulting in very different mechanical properties when these particles are under stress or shear deformation [110]. A deformation of polymer particles leads to the rearrangement of the individual polymer chains on a scale from moieties up to chain segments or even the whole polymer chain. Thus, polymers respond to deformation by very fast and small processes, that can store and release stresses, as well as slow rearrangement of longer polymer chain segments, that are irreversibly deformed. The combination of these different responses towards deformation makes polymers behave similarly elastic to solid crystalline materials and viscous like liquid materials. This behavior is called viscoelasticity and is an important property of polymers [111]. It is necessary to understand, how process and material parameters influence the viscoelastic properties of the polymers and in turn, how this influences the mechanical processing of the polymers. Especially in the dry electrode roll milling, the polymer takes on an additional role to its typically adhesive properties, by acting as a process lubricant during shearing of the granular electrode materials. Why this is the case, and how process and material parameters influence this lubricating effect will therefore be discussed in this chapter.

2.3.5.1 Mechanics of Viscoelasticity

First, a more detailed understanding of polymer shear mechanics and its measurement is helpful in understanding the role of the binder. The measurement of viscoelasticity is typically done by oscillatory dynamic mechanical analysis in a shear rheometer [111]. This is very similar to the previous method of solid and powder shear analysis. A solid polymeric sample is fixed between two plates without the possibility of stick-slip behavior at the interface. Then, a sinusoidal strain with an angular frequency is applied to the polymer. Since polymer materials exhibit elastic and viscous behavior, the measured stress is a combination of both responses, a purely elastic part according to Hooke's law, which is completely in phase with the deformation:

$$\sigma(t) = G\gamma_0 \sin(\omega t) \tag{6}$$

And a viscous part according to Newton's law, which is out of phase with the deformation by $\frac{\pi}{2}$:

$$\sigma(t) = \eta\gamma_0\omega\sin\left(\omega t + \frac{\pi}{2}\right) \tag{7}$$

Here, G is the shear modulus of the solid material, γ_0 is the applied strain amplitude and η is the dynamic shear viscosity of the liquid sample.

The mechanical response of a viscoelastic material will be somewhere between that of an elastic body according to Hooke's law and that of a viscous liquid according to Newton's law. It exhibits a phase shift δ of $0 \leq \delta \leq \frac{\pi}{2}$:

$$\sigma(t) = \sigma_0 sin(\omega t + \delta) \tag{8}$$

This mechanical response can be decomposed into two orthogonal components, one in phase $\delta = 0$ and one out of phase, $\delta = \frac{\pi}{2}$:

$$\sigma(t) = \gamma_0[G'(\omega)sin(\omega t) + G''(\omega)cos(\omega t)] \tag{9}$$

Here, G' is the storage modulus, which defines how much energy the material can store upon deformation. It is a measure of the elastic behavior of the material since the stored energy can be released. G'' is the loss modulus, which defines the energy dissipation in the material, and thus is representative of the viscous behavior of the material [111].

2.3.5.2 Influence of Temperature

The mechanical response of polymers is strongly dependent on the temperature and the deformation rate, that the polymer undergoes [112]. Since most polymers are amorphous or semi-crystalline, the molecular chains can freely move and rearrange. With increasing temperature, the movement and rearrangement of the molecules increases due to their higher energy. Therefore, with changing temperatures, the polymer undergoes different states, which are represented in Fig. 18 together with the complex modulus [112].
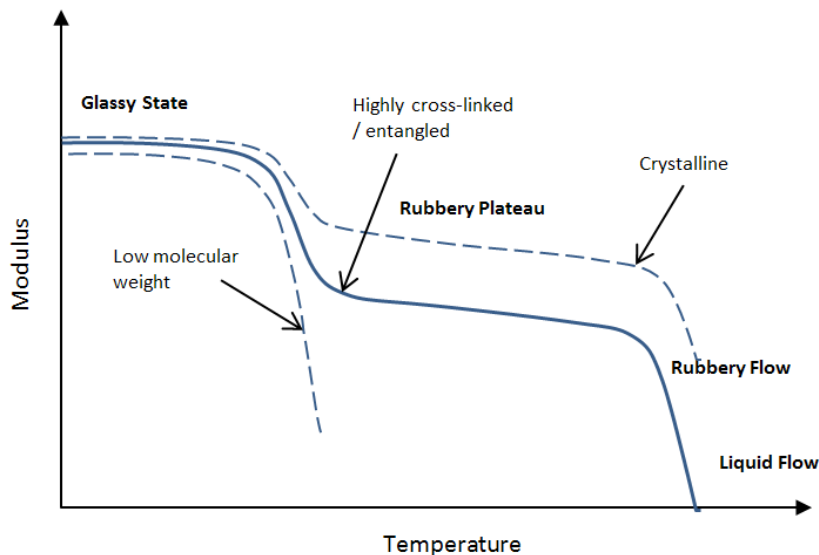
Fig. 18: Qualitative representation of the viscoelastic modulus of a polymer in dependence of the temperature [113].

Here, a polymeric sample undergoes different stages with increasing temperature. The mechanical response of the sample upon shear deformation is different according to the state of the sample. At low temperatures, polymers are in the glassy state. They have a high storage modulus

and behave more like a solid sample, where stresses are stored and released, or brittle fracture is possible at exceedingly high stresses. With temperature increasing above the glass transition temperature, polymers are in the rubbery plateau. The complex modulus is significantly lower than in the glassy state. This is due to the increased mobility of the molecule chains at higher temperatures. Upon fast deformation, the polymer shows elastic deformation and can store stresses, due to the short-range rearrangement of atoms or moieties. Upon deformation over a long duration, the sample loses stresses due to the slow rearrangement of whole molecule chains, thus showing viscous behavior. Whether elastic or viscous behavior dominates in this region is dependent on the specific polymer material properties. With further increasing temperatures, the polymer is behaving more and more viscous while the complex viscosity is decreasing. Upon exceeding the melting temperature, the polymer undergoes the phase transition and is dominantly viscous [114].

The mechanical response of polymers during the transition of the different states is very much dependent on the properties of the polymer [110, 114]. As Fig. 18 shows, polymers with a very low molecular weight do not show a very prominent rubbery region. Due to their typically short-chain molecules, they can move more freely and undergo plastic deformation under stress. Thus, they behave strongly viscous and a smooth transition from glassy state to liquid flow in its melt phase can be observed. They are considered to behave as dilute solutions [115]. High molecular weight polymers and polymers, that are highly entangled or cross-linked typically have a high complex modulus in the rubbery region. Due to strong cross-linking and intermolecular forces, the polymer is able to store stresses and only slowly release them due to the sluggish rearrangement of the long chains. This can be also the case for partly crystalline polymers. Crystalline regions have strong intermolecular forces and inhibit the rearrangement of the molecule chains over time [114]. This leads to a very distinguishable rubbery plateau with a typically high complex modulus. Also, a clear transition into the melt phase can be observed, which leads to a significant decrease in the complex viscosity of the polymer [111].

2.3.5.3 Influence of Strain Rate

In addition to the temperature dependence, the mechanical response of a polymer system is a function of the applied frequency of the deformation, thus the strain rate. For a constant temperature but varying frequency, the resulting mechanical response can be categorized again into different regions, that are very similar to the different states of the temperature dependency. They are shown in Fig. 19.
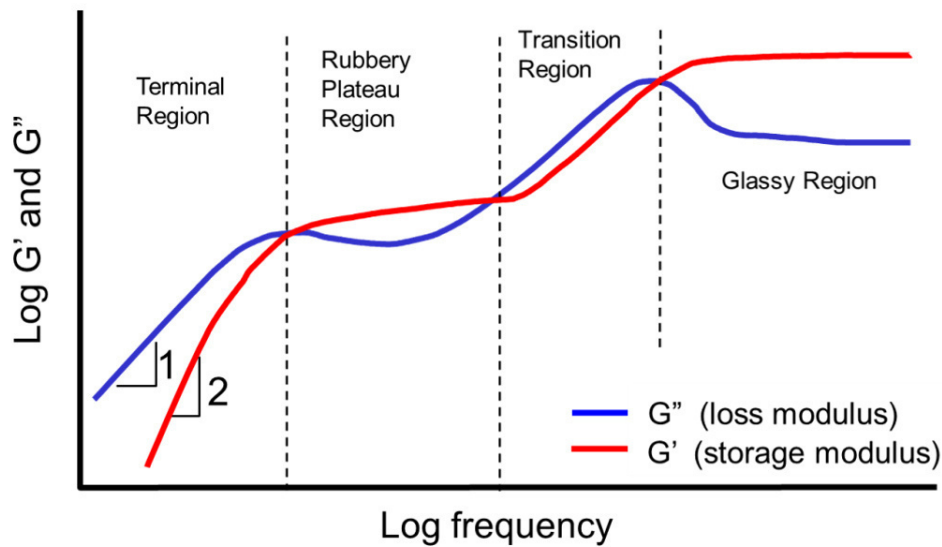
Fig. 19: Qualitative display of storage and loss moduli for a polymeric sample at constant temperature but varying frequency deformation [116].

Here, the storage and loss modulus are shown separately for an entangled polymer system at constant temperature and varying frequency of the strain deformation. For varying frequencies, the sample undergoes several transitions between regions, that are called like the states of the material when the temperature is changed. The regions observed in a frequency sweep measurement do not change the state of the sample, but the mechanical response of the sample can be considered the same as for a sample in the eponymous state. At a temperature above the glass transition temperature, a sample that is measured at very high frequencies, tends to behave like a glassy sample, for high frequencies the storage modulus is dominant over the loss modulus. If the same sample under the same temperature is measured at low frequencies, although the sample is in a rubbery state, the mechanical response is more viscous due to the high loss modulus [111, 116].

The strain rate of the polymer in the case of the dry electrode manufacturing process is dependent on the particle system, process speed, and roll gap width. The exact strain rate of each individual polymer particle is impossible to calculate or predict. But if the breakage of solid particles is avoided and dense packing during shear deformation is assumed, the strain rate of polymer deformation can be very high with increasing roll speed differences and decreasing gap widths. Thus, the strain rate dependence of the used polymers can play a significant role in material selection and process design.

The interplay of temperature and frequency dependence, as well as material properties such as chemical composition, molecular weight, entanglement, and many others, make the analysis of the viscoelastic behavior of polymers a complex challenge. Many works investigating these properties have been conducted, and rheological responses for complex systems are well docu-

mented, but since their complexity is enough to cover several books, a more detailed investigation is not possible during this work. For further documentation, fundamental and specific literature is given in the appendix for the interested reader.

3 Experimental

This section summarizes the used materials, experimental methods, and all necessary parameters for the reproduction of the experiments and measurements. Due to the evolution of the methods during the course of this work, some methods were subjected to minor changes for the production of the results. Due to the categorization of the results in three distinctive chapters, the methods are represented in detail with respect to the specific chapter in which they have been used.

3.1 Materials

The materials used in this work are summarized in Tab. 1, more specific details of the used PVDF binders are given in Tab.2.

Tab. 1: Materials with their names used in this work and their type and function.

Name	Material type	Product specifications
Active material		
NMC111	$LiNi_{0.33}Mn_{0.33}Co_{0.33}O_2$	NM-3100, BASF Toda, Japan
NMC622	$LiNi_{0.6}Mn_{0.2}Co_{0.2}O_2$	HED NMC622, BASF, Germany
Mechano-CAP 1P1	Anode graphite	HC Carbon, Germany
Additives		
Carbon black (CB)	Conductive carbon black	Super C65, Imerys, France
KS6L	Conductive lubricating graphite	KS6L, Imerys, France
CMC	Carboxymethyl cellulose	CRT 2000 PA07, Dupont, USA
SBR	Styrene-butadiene rubber binder	JSR TRD2001, JSR Micro, Japan
Kynar A	PVDF Binder	Arkema, France
Kynar B	PVDF Binder	Arkema, France
Kynar C	PVDF Binder	Arkema, France
Kynar D	PVDF Binder	Arkema, France
Others		
Primer foil	Primed aluminum (carbon)	En'Safe, Armor, France
Aluminum foil	Aluminum	Batte-Foil-0004W, Pi-Kem, UK

Tab. 2: Specifications for the Kynar Binders A to D

Binder	Type	Melt Temperature in °C	Molecular weight (qualitative)	Melt viscosity in Pa*s (at 230 °C, 100 s^{-1})
Kynar A	Homopolymer	165	Very high	5000
Kynar B	Homopolymer	168	High	3500
Kynar C	Copolymer VF2-HFP	150	High	3500

Kynar D	Copolymer VF2-HFP	165	Medium	2200

3.2 Electrode Composition

For the production of the electrode powder mixtures, a combination of AM, CB, graphite and PVDF binder has been used. The exact material composition for the powder mixtures has been slightly varied through the course of this work due to steady improvements generated by the development of the process. Therefore, Tab. 3 lists the used compositions separately according to their related chapters as they have been used in the investigations and presented in the results and discussions.

Tab. 3: List of the material compositions used in their respective chapter. *The PVDF type has been varied in this chapter.

Chapter of use	AM in %w	CB in %w	Graphite in %w	Binder in %w
4.1: Process parameters	NMC111 91	C65 2	KS6L 2	Kynar A 5
4.2: Mixing homogeneity	NMC622 93.5	C65 2.5	KS6L 1	Kynar A 3
4.3: Binder influence	NMC622 93.5	C65 2.5	KS6L 1	Kynar A-D* 3

3.3 Powder Mixture Preparation

Electrode mixtures have been prepared using a lab-size planetary batch mixer (Thinky ARV-310, Thinky U.S.A Inc., USA). Similar to the composition, the mixing procedure differs between the investigations done for the separate chapters.

For the analysis of the process parameters in the first results of chapter **4.1**, a single-step mixing process has been used. Due to no changes in material composition during the experiments in this chapter, a high reproducibility for the preparation of the powder mixture was ensured. 50 g of AM and the additives according to the composition have been mixed for one minute at a rotational speed of 2000 rpm.

For the second chapter **4.2**, which investigates the additive distribution homogeneity in the mixture, a multi-step mixing procedure has been used. Here, first, the AM and the PVDF were mixed. Then, CB has been admixed. Finally, the KS6L has been added to the blend and mixed. To achieve different states of additive deagglomeration and distribution homogeneity, three mixtures have been prepared with the same composition under different mixing procedures, where the intensity of the separate mixing steps has been varied. These mixtures are the low intensity mixture (LIM), the medium intensity mixture (MIM), and the high intensity mixture (HIM). Each mixing

step has a duration of one minute. A summary of the intensity in terms of rotational speed for all three powder blends is given in Tab. 4.

Tab. 4: Mixing intensities in rotations per minute used for the production of mixtures with different degrees of additive deagglomeration and distribution in chapter 4.2. Mixing time of one minute for each step.

	NMC622 + Kynar A in rpm	+ C65 in rpm	+ KS6L in rpm
LIM	500	500	500
MIM	700	1000	500
HIM	1500	2000	1500

The mixing procedure used for the electrode blends in chapter **4.3** is according to the mixing procedure used for the HIM in the previous chapter. Here, the beneficial properties of the homogeneous mixture have been used to perform the investigations on the influence of the different binders.

3.4 Electrode Manufacturing

3.4.1 Dry Process

For the dry manufacturing of electrodes, a two-roll calender with a roll diameter of 200 mm was used in this work (GK-300L, Saueressig, Germany). A 10 g batch of powder was manually added to the roll gap on a width of 8 mm and compacted between the calender rolls, which turned in opposite directions, as demonstrated in Fig. 7(a).

The process parameters used in chapter **4.1**, where the influence of each adjustable process parameter was analyzed, are listed in Tab. 5.

Tab. 5: Calendering parameters used in chapter 4.1 for the consecutive investigation of each process parameter. Highlighted parameters have been varied and investigated.

Investigated parameter ↓	Temperature in °C	Initial gap width in µm	Roll pressure in bar (N/mm)	Relative roll speed in %	Absolute roll speed in m/min
Temperature	20 - 180	150	150 (1125)	100	0.5
Initial gap width	150	80; 150; 250	150 (1125)	100	0.5
Roll pressure	150	150	20 − 220 (150 − 1650)	100	0.5
Rel. roll speed	150	100	50 (375)	100 - 30	0.5
Abs. roll speed	150	100	50 (375)	30	0.5 - 4

In the second chapter **4.2** the initial gap width, roll pressure, and temperature have been kept constant. Due to the differences in mechanical properties of the used material mixtures in this section, the shear influencing process parameters have been varied. The relative roll speed has been varied between 30 % to 10 % and the absolute speed has been varied between 0.1 m/min and 5 m/min. The parameters are summarized in Tab. 6.

Tab. 6: Calendering parameters used in chapter 4.2 for the investigation of additive deagglomeration and mixing homogeneity.

Temperature in °C	Initial gap width in µm	Roll pressure in bar (N/mm)	Relative roll speed in %	Absolute roll speed in m/min
180	80	30 (225)	30 - 10	0.1 - 5

Self-supported electrode sheets with a width of approx. 100 mm and lengths between 100 mm and 500 mm have been formed. Discs with a diameter of 14 mm were punched from the electrodes and laminated in a second calendering step to the pre-coated aluminum foil. The pressure and temperature remained unchanged but equal roll speeds of 0.1 m/min have been used to laminate under compaction conditions. The roll mill gap width has been set to be 3 µm lower than the aluminum and the initial electrode discs thickness combined. These process parameters were used for all the lamination steps in this work, and thus are the standard lamination parameters given in Tab. 7. Afterwards, discs of 12 mm diameter were punched for coin cells.

Tab. 7: Standard calendering parameters used for the lamination of self-supported electrodes to the pre-coated aluminum current collector.

Temperature in °C	Initial gap width in µm	Roll pressure in bar (N/mm)	Relative roll speed in %	Absolute roll speed in m/min
180	Electrode thickness + aluminum foil thickness – 3 µm	30 (225)	100	0.1

In chapter **4.3,** the use of the different binders impacts the shear properties of the resulting powder mixtures. Thus, the speed parameters were varied to accommodate the differences in the material properties. In contrast to the previous chapter, the exact investigation of the processibility was not the main focus but the production of electrodes with similar morphologies. Therefore, the speed parameters have been varied in smaller increments. A summary of the used parameters is given in Tab. 8.

Tab. 8: Calendering parameters used in chapter 4.3 for the production of electrodes with the use of different binders.

Temperature in °C	Initial gap width in µm	Roll pressure in bar (N/mm)	Relative roll speed in %	Absolute roll speed in m/min
180	80	30 (225)	30 - 10	0.1 - 2

The electrode with the Kynar B binder forms a self-supported electrode, similar to the electrodes prepared in the previous chapter when using the Kynar A binder. Discs of 14 mm diameter were punched and laminated to the pre-coated aluminum foil by a second calendering step. Additionally, the self-supported electrodes made with the Kynar B binder had sufficient mechanical strength, size and homogeneity to be laminated as a whole sheet to the precoated aluminum foil in a second calendering step. Both lamination steps have been done at the standard lamination parameters given in Tab. 7. Finally, discs of 12 mm diameter were punched for coin cells or 50 x 50 mm squares were punched for pouch cells.

The electrodes formed with the Kynar C and Kynar D binders did not form self supported electrodes, thus a different lamination process was used. Here, the powder mixture was fully processed through the calender gap, forming an electrode of approx. 500 mm length, that remains sticking to the roll with the faster circumferential speed. The rotation of the rolls is then stopped, the precoated aluminum is fed through the empty calender gap and tension is applied by the foil winders. Then, the rotation of the rolls has been continued at the standard lamination process parameters as given in Tab. 7. By softly compacting the electrode and the foil, the electrode is transferred to the precoated aluminum foil. Finally, discs of 12 mm diameter were punched for coin cells or 50 x 50 mm squares were punched for pouch cells.

3.4.2 Slurry-based Electrodes

A slurry-based reference electrode has been prepared for the comparison with the dry produced electrodes in chapter **4.2** of the results. With the same material composition, the additive distribution and electrochemical performance between the electrodes have been compared specifically. The cathode slurry for the reference electrode was mixed in three steps using a planetary mixer (Thinky ARV-310, Thinky U.S.A Inc., USA). A PVDF stock solution using Kynar A in NMP has been prepared first, and the CB was admixed. Second, AM and graphite were added and homogenized. Finally, NMP was gradually added until a solid content of 70 w% was achieved, while the mixture was further homogenized.

The electrode has been produced by a roll-to-roll coater (KTF-S, Matthis, Switzerland) with a plain aluminum foil at 0.2 m/min with two drying steps of 80 °C and 120 °C, respectively. The electrode has been calendered to approx. 30 % porosity (GKL400, Saueressig, Germany).

The graphite anode has been produced by an aqueous process route. SMG-A graphite was used as the active material and C65 as additional conductive additive. The slurry was prepared by dispersing and mixing the SMG-A and C65 in a stock solution of carboxymethyl cellulose (CMC) in deionized water by a dissolver mixer (Dispermat, VMA Getzmann GmbH, Germany) at 2000 rpm for one hour (after 5 min degassing under vacuum). Additional styrene-butadiene rubber (SBR) latex binder was added after slurry homogenization was completed, thus coagulation of the SBR particles under high shear could be avoided. The composition of the anode is summarized in Tab. 9.

Tab. 9: Graphite anode composition

AM in w%	CB in w%	CMC in w%	SBR in w%	Solid content in in w%
96	1.5	1.25	1.25	56

The slurry was coated on copper foil by a roll-to-roll coater (KTF-S, Matthis, Switzerland) and dried in two steps at 30 °C and 50 °C, respectively. Subsequently, the anodes were slightly calendered to a porosity of approx. 40 %. Such anodes have been prepared with a mass loading of 9.5 and 14.5 mg/cm^2 to be used for thin or thick cathodes, enabling the balancing at a ratio as close as possible to 1.1 of anode capacity versus cathode capacity.

3.5 Cell Assembly

CR2032 stainless steel coin cell parts (Hohsen, Japan) were cleaned in an ultrasonic bath with isopropanol and dried in a vacuum oven at 120 °C for 24 hours. The punched electrodes with 12 mm diameter were dried for 24 hours in a vacuum oven at 80 °C (VDL23, Binder GmbH, Germany). Assembly has been conducted in a glove box under argon atmosphere (MB 200B, MBraun, Germany). Punched discs of glass fiber filters (GF/C, Whatman, USA) with a diameter of 16.5 mm were used as separator and 200 µl LP30 was added as electrolyte (Merck, Germany). For the assembly of half cells, lithium discs (MTI Corp., Canada) with a diameter of 16 mm and thickness of 1.5 mm were used, while for full cells punched graphite anodes with a diameter of 14 mm were used. The cells were crimped with a pressure of 5.17 MPa with a hydraulic press (MSK-110, MTI Corp., Canada), cleaned with isopropanol, and rested for 24 hours before testing.

Pouch cells were assembled using the punched 50 x 50 mm^2 cathodes and 54 x 54 mm^2 graphite anodes. The electrodes and the 58 x 58 mm^2 ceramic coated separator foil (Separion, Litarion GmbH, Germany) were dried overnight in a vacuum oven at 130 °C and assembled in a dry room with a dew point of below -50 °C. 450 µl of LP30 electrolyte (Merck, Germany) was used for each pouch cell.

3.6 Electrochemical Characterization

For the electrochemical characterization of the produced electrodes galvanostatic rate capability tests, long-life cycling, and potentiostatic cyclic voltammetry has been used. Since all electrodes are composed of NMC622 as AM, each cell, both, half and full cell, was measured in the voltage range between 3.0 and 4.2 V at a constant temperature of 25 °C. A theoretical capacity of 175 mAh/g was used for the calculation of the C-rate currents.

Rate capability tests were started with either one or two formation cycles at C/20 followed by three cycles at C/10. Then, 10 cycles were performed at C/2, 1C, 2C, 3C and again C/2. Charging and discharging were conducted symmetrically until 1C, above which charging was conducted

always at 1C and discharging at the respective C-rate. With C-rates of C/2 and above, a constant voltage step (CV) was implemented. In the rate capability tests done for electrodes in chapter **4.2** of the results, the cut-off current for the CV step was 50 % of the corresponding C-rate. In the rate capability tests done for the electrodes in chapter **4.3** of the results, the cut-off current for the CV step was always C/20.

Long-life cycling tests were started with one formation cycle at C/20 followed by three cycles at C/10. Then, 1000 cycles at symmetric 1C were conducted. The long-life cycling tests in chapter **4.2** of the results include a relaxation cycle every 50th cycle, with a symmetric C-rate of C/20. All cycles have a constant voltage step with a cut-off current of C/20. The long-life cycling tests in chapter **4.3** of the results were performed identically except for the relaxation cycle every 50th cycle, which was not included here, due to the relaxation cycles being implemented only at a later stage of this work.

Small changes, such as the implementation of the relaxation cycle and the change in cut-off current from 50 % to a constant C/20, were introduced during the course of this work, since these methods were adapted over time and standardized in the research group, to offer consistent and comparable results for future investigations and research. This has to be noted before the comparison of the differently presented results.

Cyclic voltammetry was performed with two formation cycles at voltage steps of 0.017 mV/s, followed by three cycles at 0.034 mV/s. Then, 10 cycles were performed at voltage steps of 0.17, 0.68, and 3.4 mV/s, each. The last 50 % of each step response was used for the calculation of the corresponding current.

3.7 SEM and EDS Analysis

SEM micrographs have been recorded using a field-emission scanning electron microscope (Supra 55, Zeiss, Germany). EDS analysis has been conducted using a silicon drift detector (Ultim Extreme, Oxford Instruments, United Kingdom) at an acceleration voltage of 4 kV.

Electrode cross-sections for the analysis with SEM and EDS were prepared using an ion beam mill (EM TIC3X, Leica Microsystems, Germany), accelerating argon ions at a voltage of 6.5 kV and 3 mA gun current.

3.8 3D Surface Analysis

The 3D topographies and the surface height profiles have been investigated using a chromatic white light interferometer (MicroProf, Fries Research & Technology, Germany). The analysis size was set to 3 x 3 mm with a resolution of 1000 x 1000 points analyzed.

3.9 Powder Resistivity

A 2 g sample of powder was homogeneously filled in an insulating polymer cylinder and contacted between two copper pistons. A normal load of 80 N was applied via the copper pistons, using a static material testing machine (ZwickiLine, ZwickRoell, Germany). The height of the powder under consolidation was recorded and the resistance between the two copper pistons was measured using a multimeter (Fluke8842A, Fluke, USA). Five samples of each powder were measured, and the mean resistivity was calculated. To ensure, that resistance measurement with a multimeter delivers precise results, the powders have been tested to behave purely ohmic. For this purpose, a DC polarization method was used, applying step potentials between the pistons and measuring the current evolution. The results, shown in the appendix in Fig. A. 1, show no polarization and clear ohmic behavior of the powders. Therefore, multimeter measurements are sufficient to analyze the powder resistivity.

3.10 Shear Cell Measurements

The shear behavior of the powders and their internal friction coefficient were measured with an automated ring shear cell (RST-01, Dietmar-Schulze Schüttgutmesstechnik, Germany). The method according to Schulze was used [95](p 84-88), which is essentially a variation of the typical Jenike shear cell measurement [117]. A schematic representation of the method is given in Fig. 20.
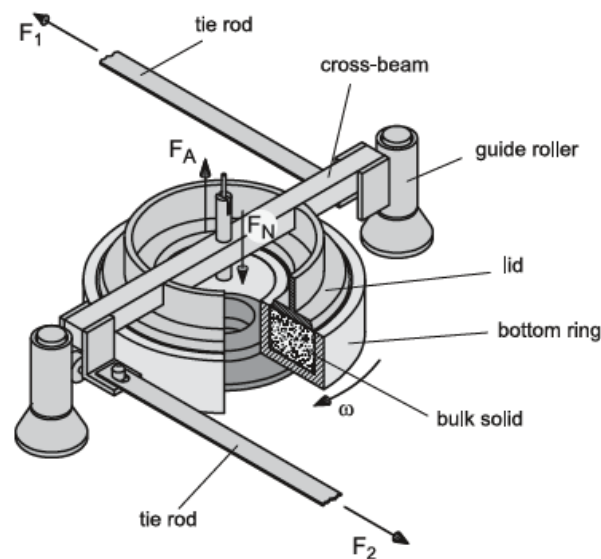
Fig. 20: Schematic representation of a shear cell used in the RST-01 by Dietmar Schulze. The bottom ring with the powder bulk is rotated, while a normal load is applied to the top ring, and the torque is measured by the tie rods [95].

The measurement procedure includes a preshear step at a high normal load. The sample is consolidated and sheared until steady-state flow is attained, after which the rotation of the ring is reversed until the shear stress is reduced to zero and the system is relaxed. A normal load below that of the preshear is applied, the sample is sheared, and the maximum shear stress is measured, which represents the incipient flow and is one point of the yield locus. This procedure is repeated, beginning with the application of the preshear normal load and shearing until steady-state flow, followed by the measurement of the next yield point. The linearization of the yield points results in the yield locus, which allows the construction of the mohrs circles and the determination of the angle of internal friction at steady-state flow.

The samples in chapter **4.2** have been measured at three different normal loads, 5, 50, and 150 kPa. These normal loads represent the normal load used for the preshear point. The determination of the yield points was done at 0.2, 0.4, 0.6, and 0.8 of the used preshear normal load.

In chapter **4.3**, the measurements of the sample at room temperature have been done at normal loads of 5, 15, 30, 50 80, 120, and 150 kPa for the preshear point. The determination of the yield points was done at 0.2, 0.4, 0.6, and 0.8 of the used preshear normal load. For the measurement at high temperatures, the ring was filled with the powder sample and heated in an oven at 200 °C for one hour. The ring with the sample has been installed and measured without delay after extraction from the oven. Normal loads of 5, 50, and 150 kPa were applied during preshear. Due to significant cooling of the sample during the measurement procedure, only the first pair of normal load and shear stress have been used for the determination of the preshear point, thus the angle of internal friction at steady-state flow. Also, no yield locus could be determined due to the time sensibility of this measurement at elevated temperatures.

4 Results and Discussion

The results can be summarized in three separate chapters. In the first chapter **4.1,** the process parameters are investigated. Their influence on the roll milling process has been evaluated by the analysis of the resulting electrode morphology, namely the electrode porosity and thickness. After the analysis of the process parameters, the second chapter **4.2** focuses on the powder homogeneity after mixing as a preparative step prior to roll milling and has been published as a separate publication [118]. This step has been found to be crucial for direct powder rolling since the correct distribution of the different materials is not only essential for good electrochemical performance of the electrode but significantly influences the manufacturing process, its reproducibility, and electrode characteristics. Electrochemical analysis of the resulting electrodes concludes this chapter and brings the results in relation to slurry-based electrode performance. With a well-investigated process setup and mixture preparation, the third chapter **4.3** focuses on the influence of the material properties of the binder on the calendering process. Especially the effect of different binder viscosity on the electrode morphology is further analyzed, showing significant differences in electrode characteristics depending on binder properties. Then again, electrochemical analysis of the resulting electrodes has been performed.

4.1 Process Parameters

4.1.1 Results

This chapter investigates the influence of the process parameters, which can be adjusted by the roll mill, on the resulting electrode morphology. The material used for these investigations is a standard mixture according to method 3.3, which has shown good processibility over a wide range of experiments. It was used for all experiments in this chapter. The SEM micrographs of the resulting mixtures are shown in Fig. 21.
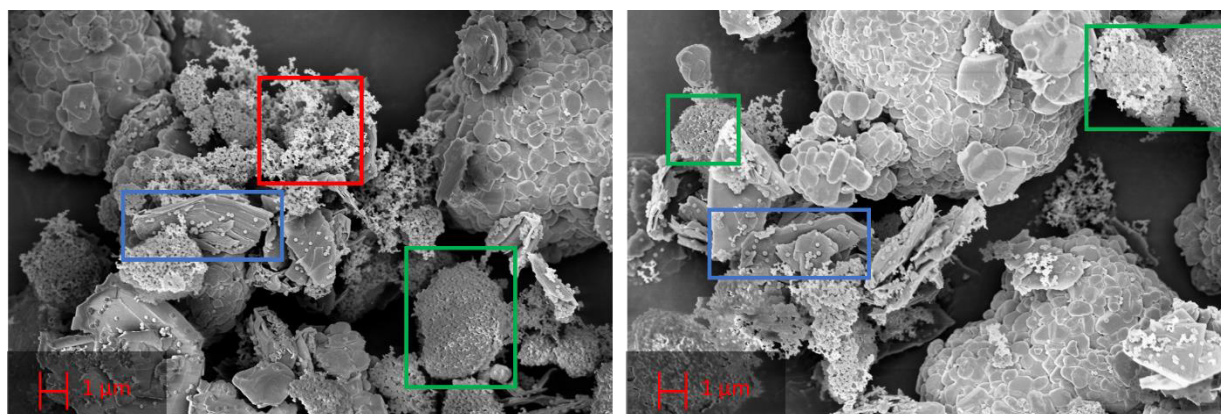
Fig. 21: SEM micrographs of the produced powder mixture. CB agglomerate particles highlighted in red, graphite particles highlighted in blue, and PVDF agglomerate particles highlighted in green.

The large and roughly round particles, that are made of small primary particles, are the NMC111 AM. The red frame highlights the conductive CB agglomerate particles. CB typically exists as an agglomerate, consisting of smaller aggregates of very fine carbon structures, that give this material its high surface area. The blue highlights show the plate-like graphite additive that serves as an additional long-range conductive additive and as a solid lubricant at the same time. The green frames show the PVDF agglomerate particles. These particles consist of many round primary particles with a diameter of approx. 200 nm, that form agglomerates during their production process. Fig. A. 2-5 in the appendix displays SEM micrographs of the pristine materials to show their initial morphology and give a reference. These representative SEM micrographs in Fig. 21 show a quite homogeneous distribution of the various material species particles. However the agglomerate particles have not been broken into aggregates or primary particles, thus highly localized species concentration are found on a small-scale view. On a large-scale view, the homogeneous distribution of the agglomerate particles leads to no concentration gradients of individual species in the mixture.

4.1.1.1 Roll Temperature

The necessary mechanical strength to obtain electrode sheets is achieved by the use of the binder, that builds the network, which incorporates the active material and conductive additives. Since in dry electrode manufacturing the binder is not dissolved, it has to be distributed in the mixture first by dry mixing and has then to be brought into close contact with the other solid materials. This is achieved by softening or melting the binder during its transit through the roll mill gap. Therefore, at constant initial gap width, roll pressure, and roll speeds according to method 3.4.1, the roll temperature has been varied to investigate its influence on the mechanical properties of the resulting electrodes. This investigation only brought qualitative results, since at low temperatures, no electrode was formed at all. With increasing temperature, first electrode flakes started to form, but they were very inhomogeneous and of low quality, with holes and rifts. Only for high temperatures near the melting point of the binder, which is 165°C, homogeneous electrodes could be obtained. The qualitative results are summarized in Tab. 10.

Tab. 10: Qualitative results for the variation of process temperature.

Temperature in °C	20-90	110	130	150	180
Electrode quality	No electrode formed, and powder exits the roll mill gap	First flakes are generated, with no cohesion between separate flakes	Cohesive sheet is formed, inhomogeneous, with holes and rifts	Homogeneous electrode formed, even thickness (except at the edges)	Homogeneous electrode, high mechanical stability, smooth surface finish

Since electrodes could only be formed for temperatures close to the melting point of the binder, all other measurements in this chapter have been conducted at a temperature of 150 °C, which was the maximum roll temperature at this stage of the work. Process temperatures of 180 °C were only possible at a later stage of this work.

4.1.1.2 Initial Gap Width and Roll Pressure

The standard cathode mixture was calendered at different initial gap widths but constant roll pressure and temperature, as well as absolute and relative speed according to methods 3.4.1. The results are given in Fig. 22.
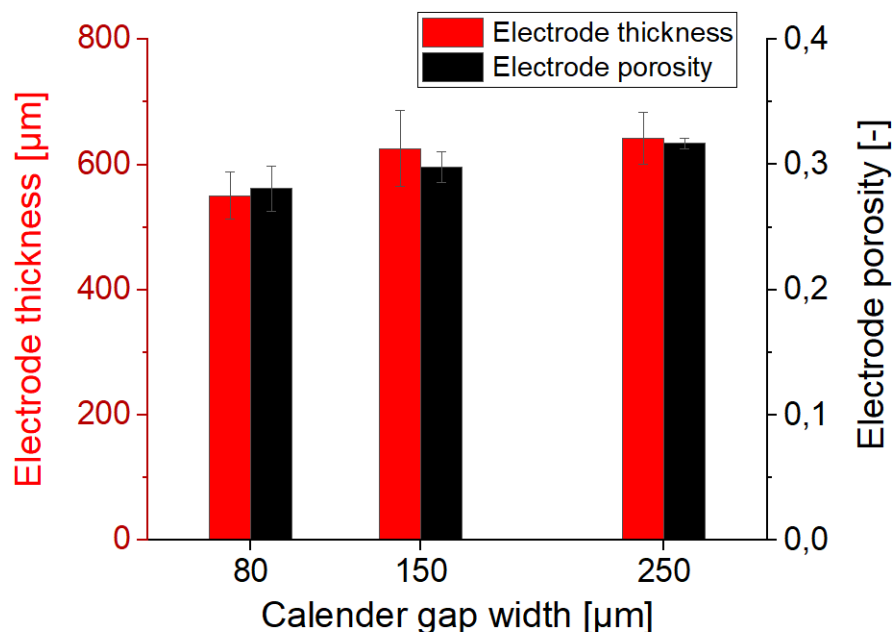
Fig. 22: Electrode thickness and porosity for electrodes produced at different initial gap widths of the rolls. At 150 °C, 150 bar (1125 N/mm), 100 %, and 0.5 m/min roll speed.

The resulting electrode thickness ranges from 550 µm for an initial gap width of 80 µm to 641 µm for an initial gap width of 250 µm. The electrode thickness is significantly higher than the set initial gap width. A slight tendency of higher electrode thicknesses with increasing initial gap width can be observed. This tendency is relatively small compared to the absolute value of the

final electrode thickness. The resulting porosities range from 0,28 to 0,32 for increasing initial gap widths, respectively. Here as well, a slight increase of porosity can be observed for higher initial gap widths.

Under the same conditions, the influence of the roll pressure on the electrode properties has been investigated. Here, the initial gap width was set to 150 μm while the other parameters remained unchanged. The results are given in Fig. 23.
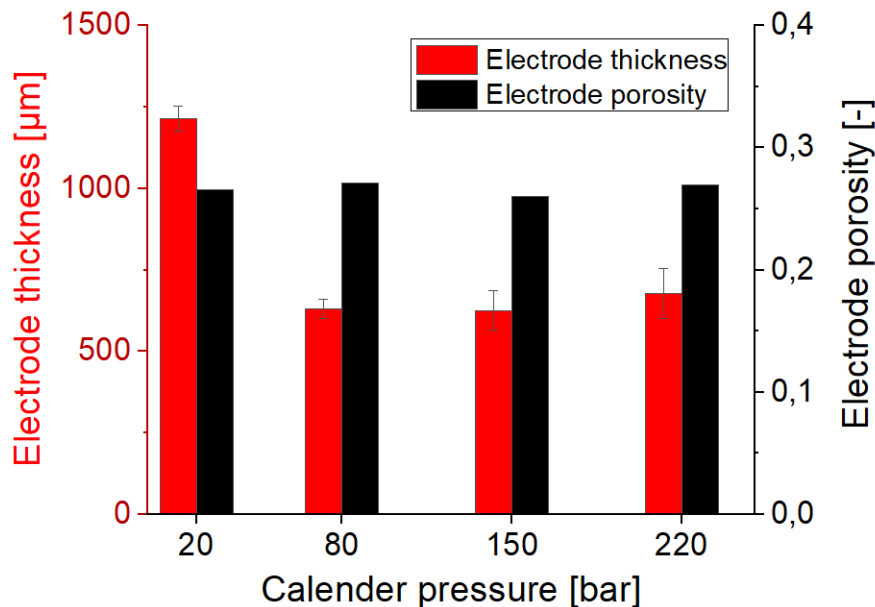
Fig. 23: Electrode thickness and porosity for electrodes produced at different calender roll pressures. At 150 °C, 150 μm initial gap width, 100 %, and 0.5 m/min roll speed.

At a roll pressure of 20 bar (150 N/mm), the resulting electrode has a thickness of approx. 1215 μm. For roll pressures above 80 bar (600 N/mm), the electrode thickness lies in the range between 626 and 678 μm and shows a slight increase for higher roll pressures. Thus, between 20 and 80 bar a drastic change in electrode thickness is observed. The electrode porosity lies around 0.27 for all measured pressures. No clear tendency has been found for increasing pressure.

4.1.1.3 Roll Speed

The investigation of the influence of the roll speed has been done in two parts. First, the relative roll speed has been investigated. This means, that one roll turns with a constant circumferential speed, while the speed of the second roll varies. This difference is expressed in percent, with the slow roll having only a percentage of the speed of the fast roll. For the investigation of the relative speed, an absolute speed of 0.5 m/min for the fast roll has been used. Other process parameters such as roll temperature, initial gap width, and roll pressure remain constant according to methods 3.4.1. The results of the investigation of relative roll speed are given in Fig. 24.
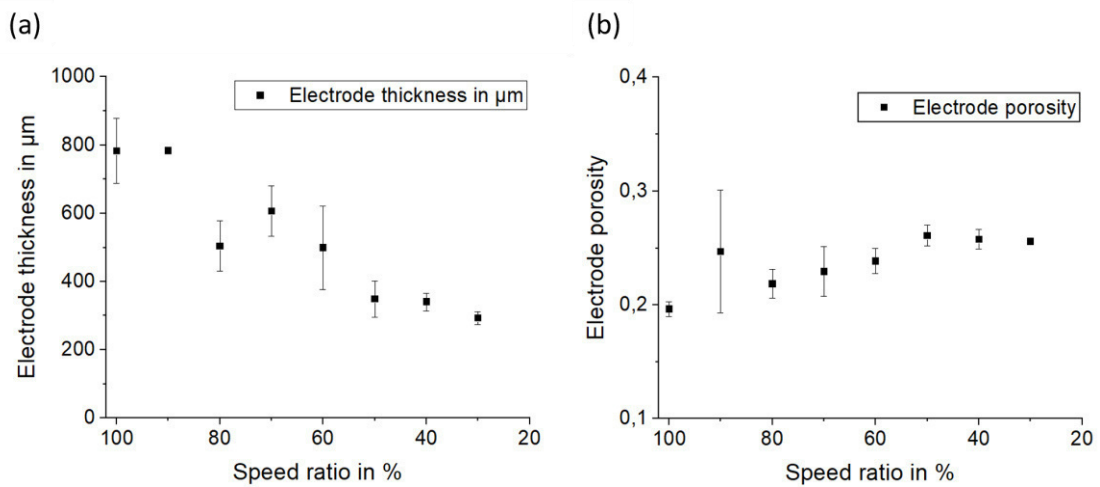
Fig. 24: Resulting electrode thickness (a) and electrode porosity (b) for varying relative roll speed. Constant temperature, roll pressure initial gap width, and fast roll absolute speed.

For equal roll speeds at 100 %, the resulting electrodes have a thickness of 782 μm. With decreasing speed ratio, so with decreasing slow roll speed, the electrode thickness decreases to 293 μm for a speed ratio of 30 %. The porosity of the electrodes produced at equal roll speeds is approx. 0.20 and increases to 0.26 with decreasing speed ratio. Some of the data points have high error bars, indicating low reproducibility of the process and/or inhomogeneous electrode properties. The measured data at 90 % relative speed shows this very clearly. Here, no fluctuation in electrode thickness has been observed for the produced electrodes, but strong fluctuations in electrode porosity. Thus, the material underwent different degrees of densification.

Under the same process conditions and using the same powder mixture, the relative roll speed was fixed at 30 % and the absolute roll speed was increased. This means, the speed of the fast roll has been varied and the slow roll has been changed to maintain a relative speed ratio of 30 % compared to the fast roll. The exact process conditions can be found in methods 3.4.1. The results are given in Fig. 25.

(a)

(b)
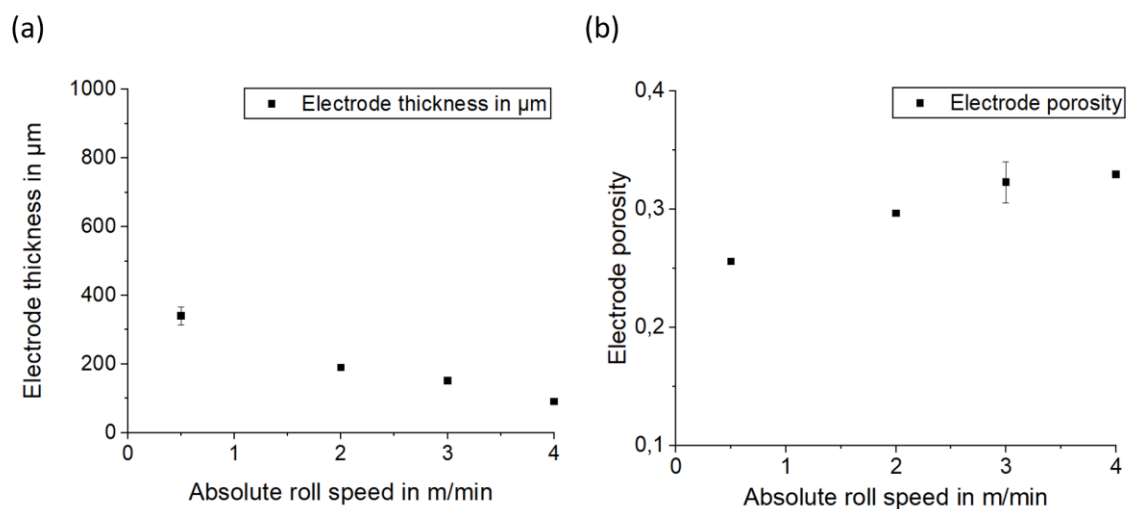
Fig. 25: Resulting electrode thickness (a) and electrode porosity (b) for varying absolute roll speed.

The resulting electrode thickness decreases significantly from 340 µm to 91 µm with increasing absolute roll speed, starting from 0.5 m/min to 4 m/min, respectively. For the same change in absolute roll speed, the porosity increases from 0.26 to 0.33. A steady decline of the electrode thickness and increase in electrode porosity can be observed for both, decreasing relative speed, and increasing absolute speed of the rolls.

In Fig. 26 the SEM micrographs of the resulting electrode surfaces are shown for a densely compacted electrode at a 100 % speed ratio and a less compacted electrode at a 50 % speed ratio under otherwise identical process conditions.
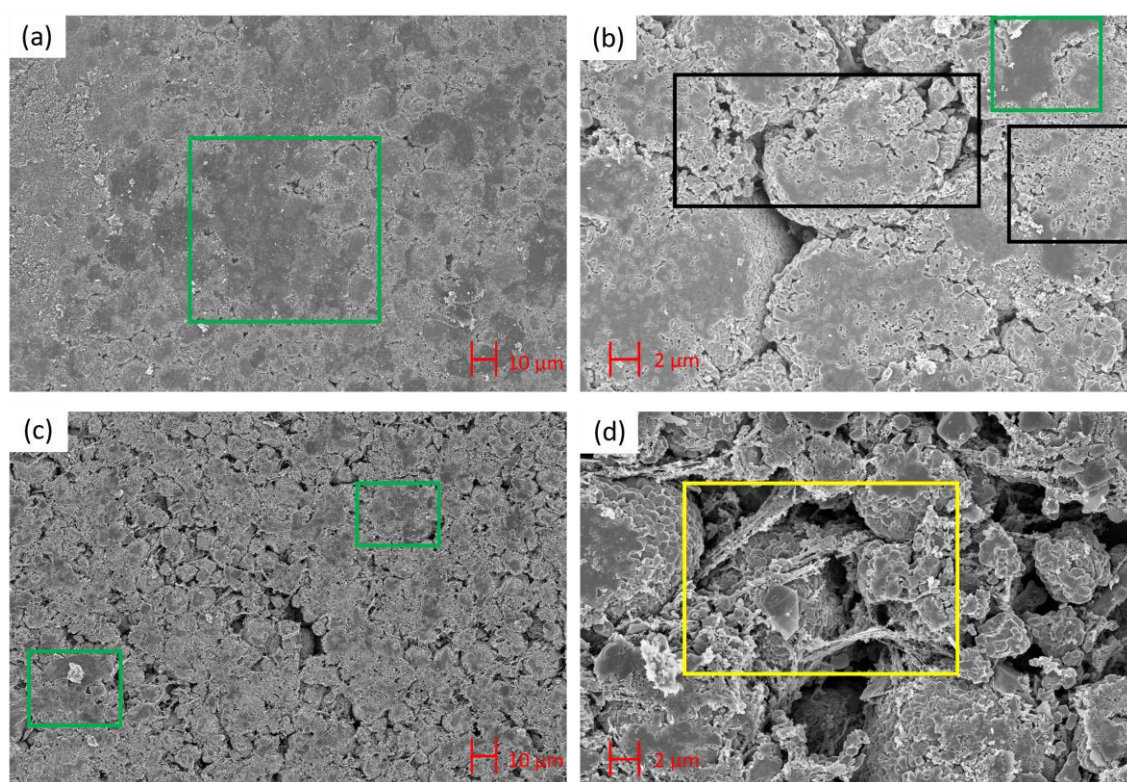
Fig. 26: SEM micrographs of an electrode produced at 100 % relative roll speed (a) and (b), and an electrode produced at 50 % relative roll speed (c) and (d). Green highlights indicate agglomerated areas of binder, black highlights show fractured AM particles and yellow highlights show binder filaments.

The SEM micrographs of the electrode produced at 100 % relative roll speed show a very densely compacted electrode surface. Large surface covering agglomerations of melted binder are clogging the surface (green highlights) and lead to a low porosity. Fractured AM particles are found across the whole surface area (black highlights). The SEM micrographs of the electrode produced at 50 % relative roll speed show a significantly less compacted surface structure. Only a few and small agglomerates of the binder are found on the surface and visible open pores are spread across the surface. At higher magnifications the existence of binder filaments can be seen (yellow highlights), which are mingled with CB aggregates. These fibrils are found spanning across the pores between AM particles, bridging them. Also, only occasionally fractured AM particles can be found.

To further investigate the morphology of the electrodes and the additive distribution in the bulk, cross sections have been prepared according to method 3.7 and SEM and EDS analysis have been conducted. Fig. 27 shows the results for the electrode produced at 50 % relative roll speed.
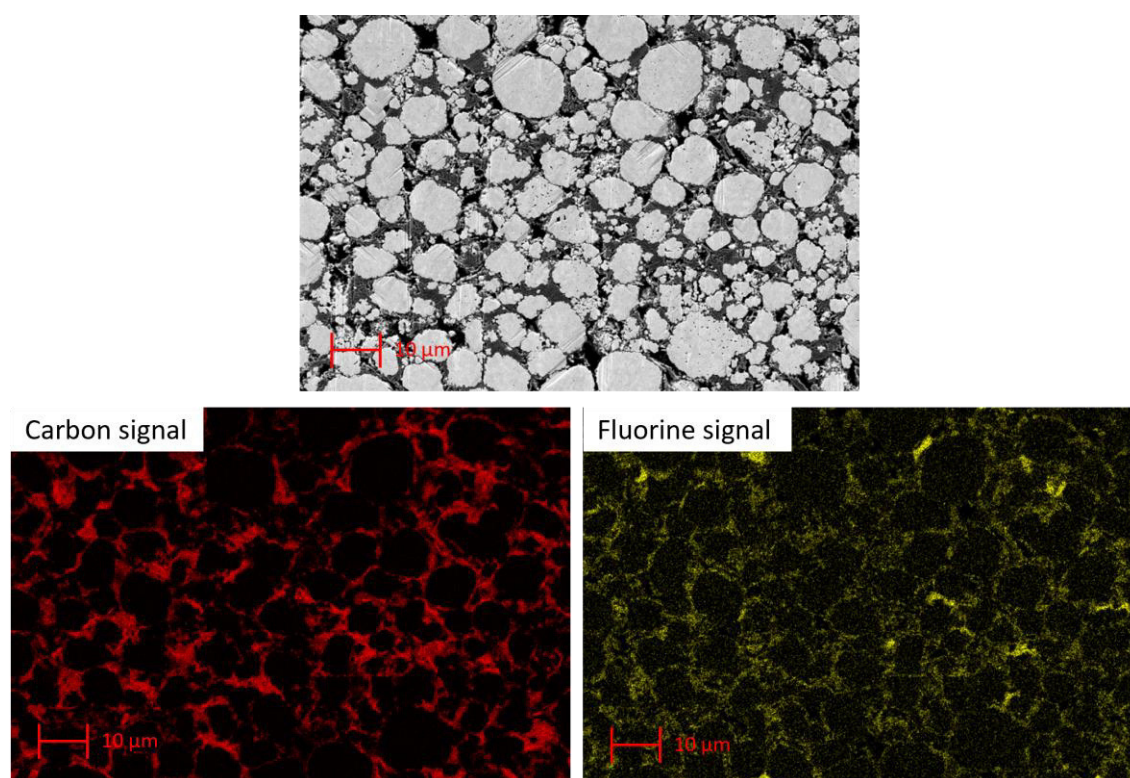
Fig. 27: SEM micrograph of a cross-section of an electrode produced at 50 % relative roll speed. EDS analysis of the same cross-section with the carbon and fluorine signals.

The SEM micrograph of the cross-section shows almost no fractured AM particles in the bulk of the electrode. Additive and pore distribution seems to be homogeneous through the electrode bulk. The EDS analysis of both, carbon and fluorine signals, shows, that additive distribution is almost homogeneous through the electrode bulk. Only a few areas with no carbon signals can be found, indicating the lack of CB and binder in those areas. Also, the fluorine analysis shows the existence of a few binder agglomerates, indicated by strong fluorine signals (yellow). In these areas, the binder concentration is locally very high. Although a few inhomogeneities concerning the CB and binder distribution can be found, no general concentration gradient is observed.

The surface structure, as well as the electrode morphology in the cross-section, seem to be quite homogeneous on a microscopic scale, but macroscopically, the surface of the electrodes is uneven, when electrodes were processed at different relative roll speeds. Fig. 28 shows SEM micrographs at low magnification of an electrode produced at 50 % relative roll speed.
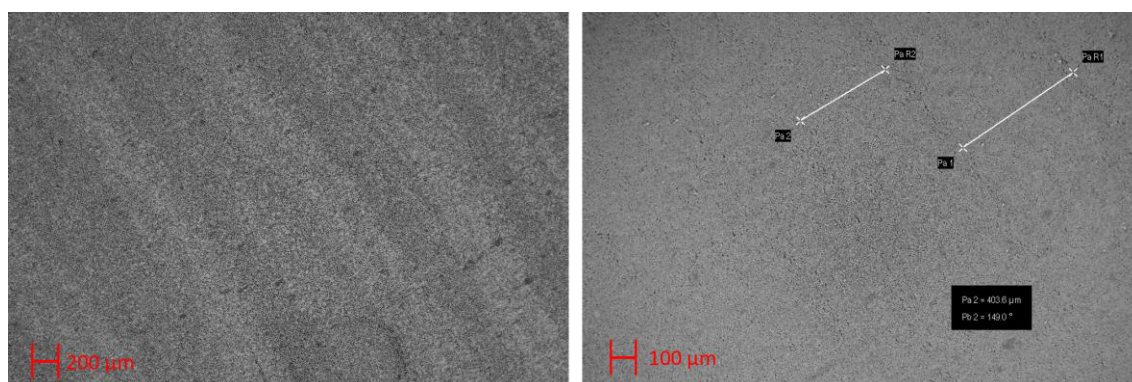
Fig. 28: SEM micrographs of the electrode surface of an electrode produced at 50 % relative roll speed. An almost periodic wave-like pattern is visible on the surface.

A repeating pattern on the electrode surface can be observed for electrodes, that were produced with the use of different relative roll speeds. This pattern is visible with the eye, as well as SEM at low magnifications. Due to the top-down view, white light interferometry has been conducted to better investigate the surface structure of the electrodes. Fig. 29 presents the results of this analysis for electrodes produced at different relative roll speeds showing a 3D image of the surface structure together with a profile of the surface height parallel to the flow direction of the material during processing.
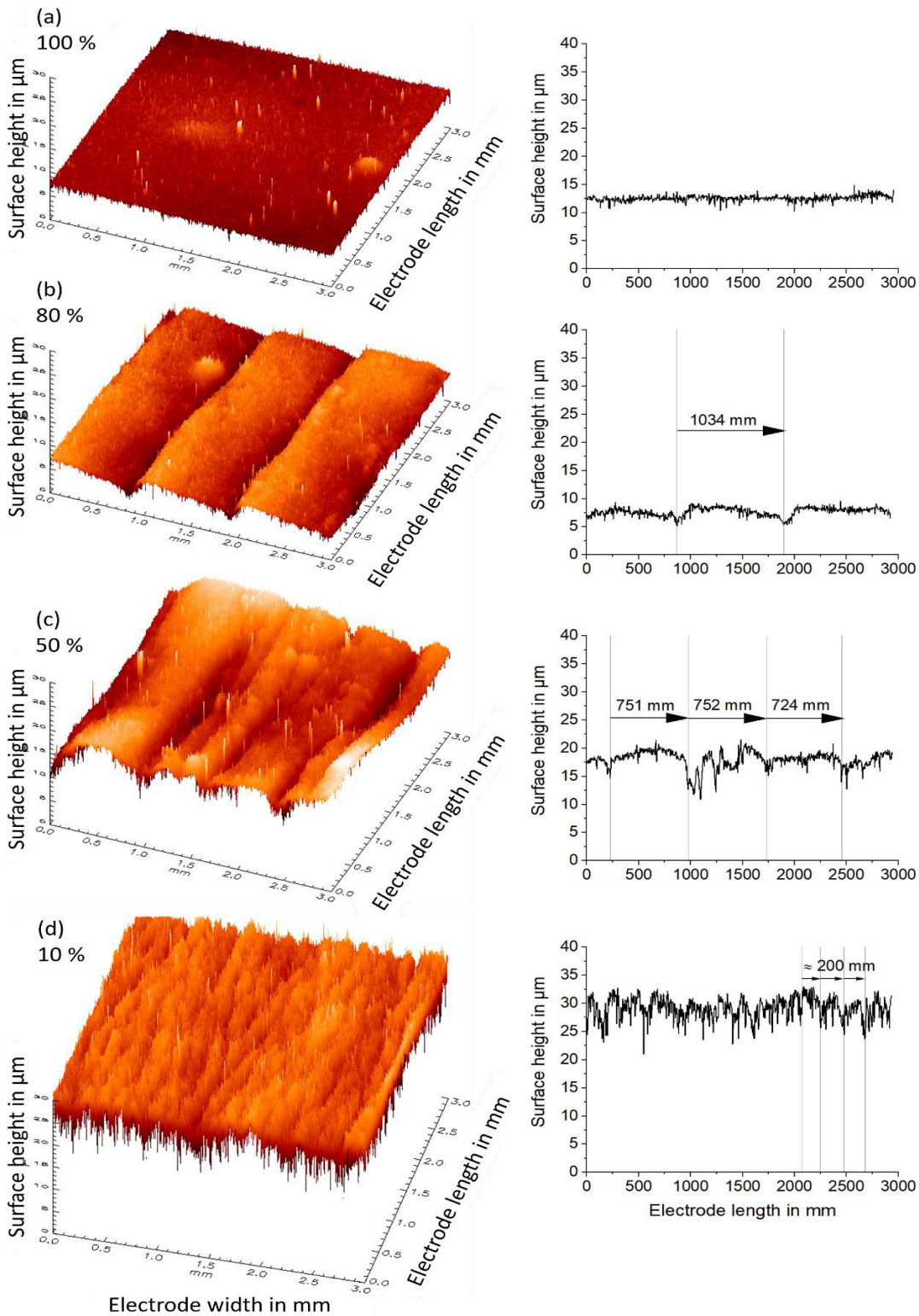
Fig. 29: Surface analysis by white light interferometry with a 3D image (left) and profile of the surface height (right) of electrodes produced at different relative roll speeds of 100 % (a), 80 % (b), 50 % (c) and 10 % (d).

At 100 % relative roll speed, thus at equal roll speed and pure compaction, the electrode surface is very smooth. With the introduction of unequal roll speeds, the resulting electrodes clearly show an uneven surface topography in the form of waves. These are of quite precise periodic nature at low relative speed ratios such as 80 %, each wave having a distance of approx. 1 cm between their reoccurrences. Each wave leads to an increase in electrode thickness, followed by a rapid decrease in thickness, as can be well seen in the surface height profile. With decreasing relative roll speed, such as 50 %, the wave formation has a more irregular nature and a lower distance between their reoccurrence, with approx. 750 µm. The waves are not entirely parallel to each other, and some can be subdivided into smaller waves. At very low relative speed ratios, such as 10 %, thus very shear-promoting process parameters, frequent wave formation can be observed. The distance between neighboring waves is approx. 200 µm and different waves often collide at small angles, producing an almost parallel pattern on the electrode surface. Height differences between the minimum and maximum values of neighboring waves are approx. 5 µm and with that slightly lower than at 50 % relative speed ratio with differences of roughly 8 µm, respectively. With a macroscopic view, the electrodes produced at low relative speed ratios, thus high shear promoting process parameters, have a more even electrode thickness than electrodes produced at intermediate relative toll speeds. They also have a higher surface area, due to the higher number of occurring waves.
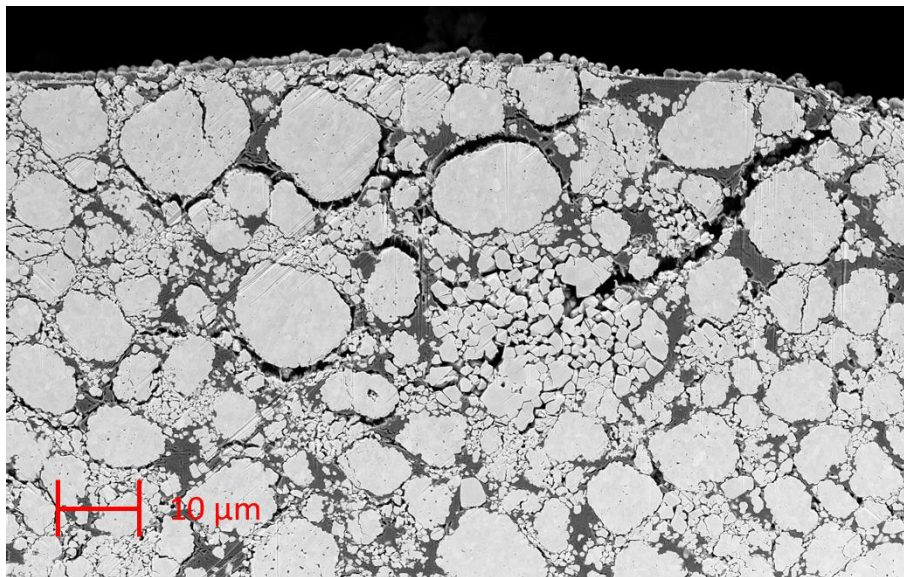
Fig. 30: SEM micrograph of the cross-section of an electrode produced at 50 % relative speed with an explicit focus on the wave-like structure on the surface.

An SEM micrograph of the electrode cross-section perpendicular to the material flow direction with a focus on such a wave-like structure is shown in Fig. 30 for an electrode produced at 50 % relative roll speed. A rise and fall in surface height can be seen accompanied by a crack, that forms at the end of the structure. Also, broken AM particles can be found along the crack through the bulk of the electrode, indicating strong stress build-up and release.

Detailed electrochemical analysis of the resulting electrodes was not possible at this stage of the work. There was yet no solution to properly laminate the electrodes to a current collector and alternative methods (hot press lamination or surface sputtering with gold) either altered the electrode significantly or delivered results, that were not comparable to properly laminated.

4.1.2 Discussion

It has been found that high temperatures are beneficial for the direct powder calendering of electrodes. First, it enhances the mechanical strength of the resulting electrode strip, especially with temperatures close to and above the melting temperature of the binder. Second, the processibility of the powder blend is improving, enabling the production of thinner and more homogeneous electrodes. The increase in mechanical strength comes from the activation of the binder's adhesive properties at high temperatures. It is necessary for the binder to glue the other solid materials together to provide the mechanical strength, that is needed to obtain an electrode. Since the binder is not dissolved in direct powder roll milling, the binder has to be softened or melted, so that the contact area between binder and other solid material can be increased during compaction. With a high contact interface between the binder and the AM and CB additive, the binder establishes strong mechanical forces between the particles due to its strong surface adhesion and mechanical interlocking. The surface adhesion is caused by strong dispersive forces due to the long molecular chains of the polymer and the herein resulting strong van-der-Waals forces [114]. The mechanical interlocking is a result of the softening or melting of the binder accompanied by the compaction of the powder. The solid materials are pushed into soft PVDF or the PVDF is melted on the surface of the solid particles. This allows the PVDF to fill in holes and crevasses in the surface of the solid active materials, not only increasing the contact interface area but also interlocking mechanically, once the PVDF is cooled down and solidified.

With temperatures increasing above the melting temperature of the PVDF, the processibility of the powder blend steadily improves. This is attributed to the more viscous behavior of the PVDF in its melt phase and the reduced complex viscosity at higher temperatures [110]. This makes the PVDF more prone to plastic deformation during compaction of the powder bed. Thus, it counteracts the build-up of strong force chains and finally reduces the potential of AM particle breakage and crack formation in the electrode. Due to this property of the binder, it can be understood as a lubricating agent in addition to its properties as a binder and adhesive. With even higher temperatures, the viscosity of the binder further decreases, promoting its plastic deformation, thus increasing the contact area to the solid material, resulting in higher mechanical strength of the electrode. Therefore, process temperatures above the melting temperature of the binder are beneficial, if high mechanical strength of the electrode, or a reduction of stress build-up during processing is necessary. It has to be noted, that changes to the binder upon melting and solidifying, such as reduced crystallinity or material expansion and shrinkage, have to be accounted for. Potentially, these processes can play a role in electrode manufacturing, but

since no such influences could be observed during this work, these effects have not been further investigated.

The analysis of the initial gap with and roll pressure in Fig. 22 and Fig. 23 show, that they have barely any influence on the resulting electrode properties. Only for very low roll pressures, such as 20 bar (150 N/mm), a high increase in electrode thickness could be observed. At such low pressures, the local stresses on the particles in the force chain network are also low and insufficient to deagglomerate the additive particles, especially the CB and graphite. With no deagglomeration, the powder is not able to accommodate the local stress build-up by plastic deformation of the agglomerates. This finally leads to the resistance of the powder bulk, which is the sum of all local stresses, to easily become higher than the initially low roll pressure, leading to profound gap opening during processing and high electrode thickness. Above a certain critical pressure, where the additives are deagglomerated under the local stresses, the electrode thickness decreases to an almost constant value. Only small changes in electrode thickness and porosity can be observed for pressures above this critical roll pressure. Thus, high roll pressures show no use for the control of electrode thickness and porosity. On the contrary, it leads to increased plastic deformation of the AM, as can be seen in the SEM micrographs of the electrodes produced in Fig. 26. This is detrimental in most cases of electrode production since AM particle breakage is one of the main degradation mechanisms in an electrode, often leading to high losses in electrode capacity [69].

The initial gap width of the rolls does not influence the electrode properties much. This is due to the roll mill gap being more dependent on the shear properties of the material and roll surface during steady-state processing [72]. The initial gap width just defines the minimum gap width of the rolls during processing and at which the process begins. The mechanical and shear properties of the powder finally define the process and the resulting electrode properties.

In contrast to the initial gap width and roll pressure, the speed parameters of the calender rolls have a very strong influence on the electrode properties. By using different speeds for the two rolls, a speed profile is introduced to the powder bulk in the calander gap. While the material properties define their shear behavior, the introduction of a speed profile onto the material does promote shearing by increasing the speed differences between neighboring particles. Higher speed differences between the rolls, thus lower relative speeds as defined in this work, lead to promoted shearing in the calender gap and a reduction of the compaction zone. As demonstrated in Fig. 24 and Fig. 25 this leads to a decrease in electrode thickness, due to the reduction of the gripping angle, and to increased porosities, due to a smaller compaction zone. The same effects are observed for an increase in absolute roll speed if a relative speed is already applied. The absolute difference between the roll speeds is increasing, even further promoting the granular shear during processing.

The more profound shearing of the powder bulk and the reduction of the compaction zone is also evident in the SEM micrographs of the electrode surface and cross-section in Fig. 26 and Fig. 27. High porosity and no AM particle breakage is found for the electrodes produced at different roll speed, indicating low compaction, and reduced local stress build-up in the force chain

network. Additionally, surface analysis shows, that fine filaments connect different AM particles, which are the product of binder filamentation induced by shear deformation. Since the filaments span across several AM particles in one major spatial direction, it can be safely assumed, that profound shearing was necessary to establish the distance between the AM particles, that were once in contact during processing.

The introduction of granular shear can be seen in the macroscopic properties of the electrodes, as well. The surface structure of the electrodes produced at different roll speeds shows the existence of wave-like structures, that are accompanied by an increase of the electrode thickness, as shown in the SEM micrographs at low magnification in Fig. 28 or the surface analysis by white light interferometry in Fig. 29 . A close look at one of these structures in the SEM micrograph of the electrode cross sections show, that these structures are the results of local stress build-up and release. This can be assumed by the profound AM particle breakage indicating high stresses, followed by the crack formation, indicating stress release. Such a periodic behavior is often observed in granular shear, since the shearing at a shear plane is accompanied by small volume expansions, especially for particles with low aspect ratio. The interfaces of a shear plane during granular shear are made of many individual particles. If the particles are not plate-like or do not have flat surfaces, like the round AM particles in this work, the shear interfaces are never microscopically flat. By the relative movement of the interfaces during shear, a volume expansion is necessary to overcome the surface roughness of the interface [94]. This volume expansion leads to the increase in electrode thickness and the profound stress build-up, followed by stress release and crack formation. For speed parameters, that only slightly promote granular shear, thus high relative speeds such as 50 %, this stress build-up and release is very significant, as shown in Fig. 29. The crack formation is very periodic over a long electrode length, leading to strong differences in electrode thickness. With more shear-promoting process parameters, such as 10 % relative speed, the length and duration of the stress build-up are reduced. This leads to smaller differences in electrode thickness and to smaller or even no crack formation at all. Due to the frequent reoccurrence of the stress build-up and low differences in electrode thickness, pseudo pseudo-stationary process is established at high shear-promoting process parameters. The macroscopic thickness of the electrode is homogeneous along the electrode length, strong crack formation is avoided, and a high porosity and electrode surface is created, which can be beneficial for the electrochemical performance of the electrode.

Overall, the analysis of the process parameters has shown, that the electrode properties thickness and porosity are heavily influenced by the shearing and compaction of the powder during calendering. The mechanics defining the granular shear are mainly influenced by the material properties, but also the process parameters, that promote shearing. Thus, initial gap width and roll pressure only have a minor influence on the resulting electrode properties. On the other hand, the control of the roll speed offers the possibility, to heavily influence granular shear by introducing a speed profile to the powder bulk by differences between the speed of the two rolls. With this, a strong influence can be taken on the electrode thickness and porosity and makes the control of the roll speeds the most important process property for the adjustment of electrode properties.

Along with the possibility of influencing the electrode properties with the roll speed parameters, increased shearing of the powder bulk leads to a reduction of local stress build-up, avoiding inhomogeneous compaction and disadvantageous plastic deformation of AM in the form of particle breakage. Additionally, electrode thickness becomes more homogeneous on the larger length scale of the electrode, and potentially beneficial morphologies are created in form of higher electrode surface area.

4.2 Mixture Homogeneity

The analysis of the process parameters has not only shown their influence on the process, but was a good foundation for the observation of additional dependencies, that were relevant to the development of the process. One of these observations was the influence of additive agglomerates and their distribution in the powder mixture. As described in the previous section, the agglomerates play a role in the mechanics of shear flow and compaction but also affect the electrochemical performance of the final electrode. So far, a very reproducible mixture was used, where the different material species particles were simply homogenized, but additives were not deagglomerated. This mixture resulted in electrodes with disadvantageous electrochemical properties so that even basic electrochemical characterization was difficult to perform. Additionally, during the preparation of a high number of mixture batches for the different experiments, it was found, that small changes in either mixing conditions or material composition or mass led to significant changes in the shear behavior of the resulting mixture. Such changes in the mixture quality translated to big differences in powder processibility and electrode morphologies under otherwise constant process parameters. Therefore, this section investigates the influence taken by the dry powder mixing conditions on the resulting distribution of materials in the powder bulk, their processibility and the resulting electrode morphology and electrochemical performance [118].

For this, three powder mixtures with the same composition using different mixing intensities have been prepared with the goal to achieve a different state of additive deagglomeration and distribution in the powder bulk. A low-intensity mixture (LIM) was prepared, where particles were homogenized but not deagglomerated. A medium-intensity mixture (MIM) was prepared, where conductive CB and PVDF binder particles were mostly deagglomerated but not entirely homogeneously redistributed in the mixture. Finally, a high-intensity mixture (HIM) was prepared, where CB and PVDF particles were completely deagglomerated and then homogeneously redistributed on the active material surface. These powder blends have then been manufactured to electrodes, and the influence of the mixing intensity is investigated by the resulting electrode morphologies and electrochemical performance.

4.2.1 Results

4.2.1.1 Mixture Homogeneity Analysis

The characterization of the mixture homogeneity and the deagglomeration of the additives has been done by extensive SEM imaging and qualitative analysis of the micrographs. Statistical image analysis has been attempted, but due to the uneven sample surface and very similar signal emission of the materials the obtained results were found to be imprecise. A sufficient solution could not be found during this work. Although a more quantitative analysis of mixing homogeneity and additive deagglomeration and redistribution would be desirable, qualitative analysis with a very large sample size of SEM micrographs was performed. Supporting that, the electric

resistivity of the resulting powder mixtures was analyzed under an applied normal load to investigate the deagglomeration and distribution of the conductive CB in the powder bulk. Representative SEM micrographs and the measured electric resistivities for the three dry mixtures are given in Fig. 31. A large sample size of representative SEM micrographs is given in the appendix in Fig. A. 6-8. Additionally, the powders have been analyzed by the DC polarization method to ensure purely ohmic behavior of the samples. The results are given in the appendix in Fig. A. 1.
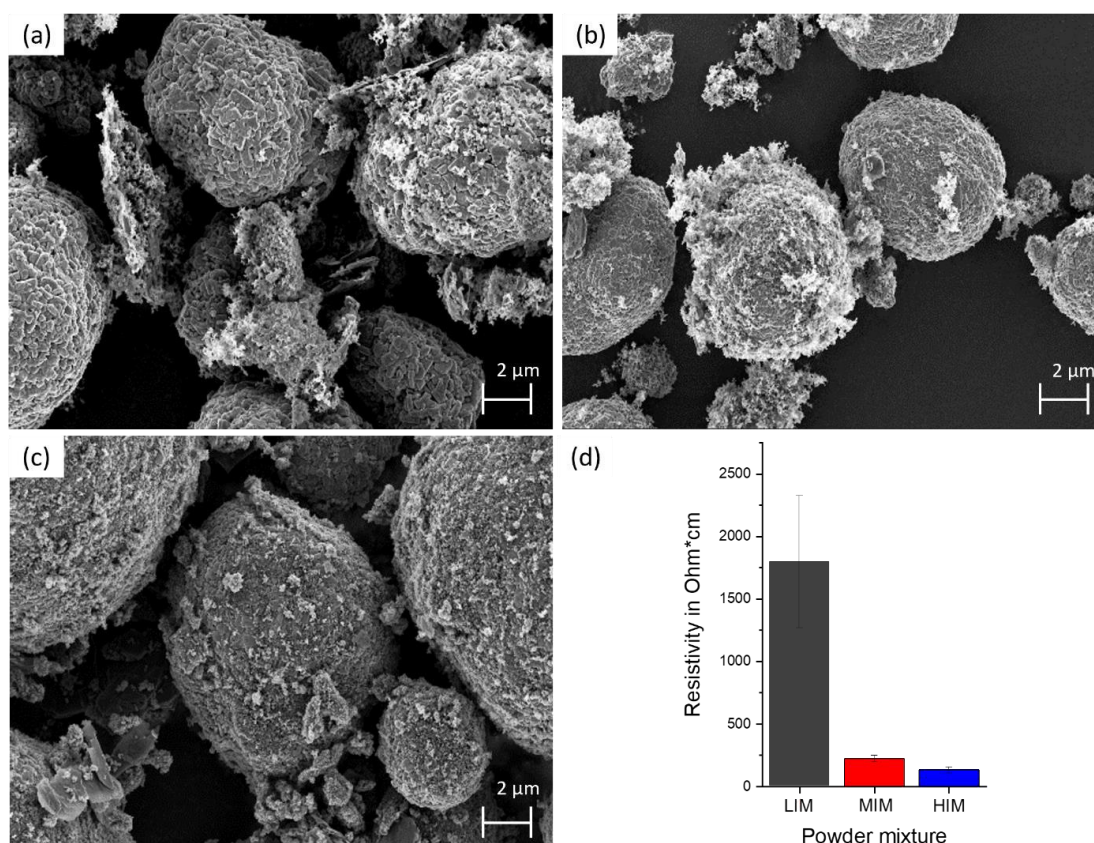
Fig. 31: Representative SEM micrographs of the dry powder mixtures: LIM (a), MIM (b), HIM (c), and the measured powder resistivities (d) [118].

The SEM micrographs of the LIM show a particle blend, that is very similar to the mixture used in the previous section for the investigation of the process parameters. AM, CB, and PVDF particles are intact and can be clearly separated from each other. Almost no additive deagglomeration can be observed in the LIM. The AM surface is mainly free from any additives. The SEM micrographs of the MIM show a particle blend, where intact CB and PVDF agglomerate particles can be rarely found. The additives are found in smaller aggregate sizes, sometimes attached to the AM surface. Many AM material particles are still uncovered by the additives. In SEM micrographs of the HIM, no CB or PVDF agglomerate particles can be identified, thus the additives have been deagglomerated. Also, the surface of each AM particle is homogeneously covered by the deagglomerated PVDF and CB. A few small aggregates consisting of PVDF and CB can be found in between the covered AM particles due to slightly excessive use of the additives (beneficial for electrochemical performance). The measured electric resistivities of the three powder

mixtures under an applied normal load in Fig. 31(d) help to differentiate the rate of CB deag-glomeration. The LIM has a significantly higher resistivity compared to the other two mixtures with 1793 Ohm*cm. The resistivity of the MIM and HIM differ slightly with 226 Ohm*cm and 135 Ohm*cm, respectively.

4.2.1.2 Shear Behavior and Processibility

The frictional properties of the produced mixtures were analyzed using a ring shear cell and compared to a sample of pure NMC622. Additionally, the static friction coefficients of the pure CB and KS6L graphite have been measured and also compared to pure NMC622 to show the influence of each specific component on the frictional properties of the powder. The measurement of the dynamic internal friction coefficient (DIFC) has been done at different normal loads since the frictional behavior of powders is significantly influenced by the applied pressure [95]. The results are shown in Fig. 32, the measuring procedure is given in methods 3.10.
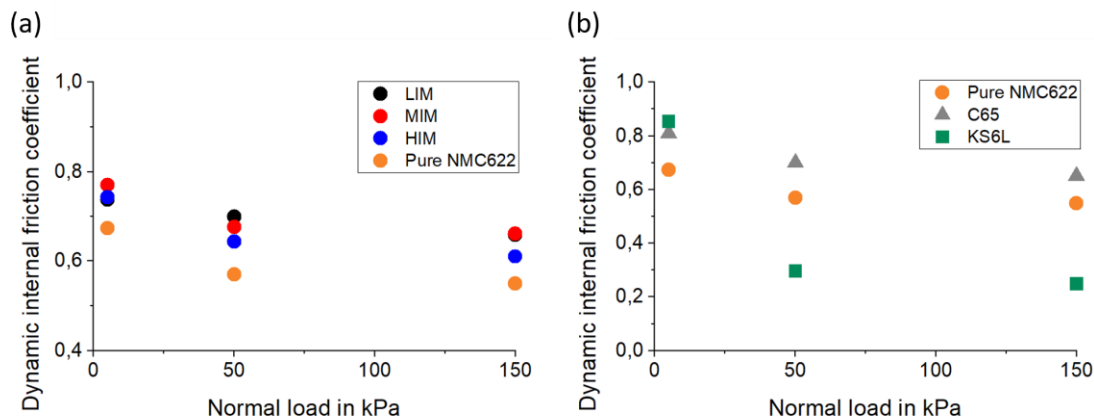
Fig. 32: Dynamic internal friction coefficients of the investigated mixtures (a) and pure additives (b) compared to pure NMC622 [118].

The DIFC of all three mixtures lie significantly above that of the pure NMC622 with approx. 0.75 compared to 0.67, respectively. With increasing normal load, all of the DIFC decrease in value as is typical for solid materials. The pure NMC622 remains at DIFC lower than the mixtures. Comparing only the mixtures, the MIM has the highest DIFC at low normal loads, with 0.77 compared to 0.73 of both, the LIM and HIM. With increasing normal loads, the DIFC of the HIM decreases stronger than that of the other mixtures. At a normal load of 150 kPa, it results at 0.61 compared to 0.66 for both, LIM and MIM. Therefore, it indicates better shear behavior, since finally, lower shear forces are needed to induce shearing when a normal load is applied to the material. A look at the influence of the additives on the shear behavior in Fig. 32(b) shows, that at low normal loads, the DIFC of the additives is higher than that of the pure NMC622, with values of 0.81 for the CB and 0.85 for the KS6L compared to the 0.67 of the NMC622. With increasing normal load, the DIFC of the C65 is decreasing, but remains significantly higher than the DIFC of the NMC622 with 0.65 compared to 0.55, respectively. The DIFC of the KS6L on the other hand is rapidly decreasing to very low values of 0.29 or 0.25 for normal loads of 50 or 150 kPa. Thus, the KS6L has by far the lowest measured dynamic friction coefficients at high normal loads.

The analysis of the processibility of the powders has been conducted directly in the roll mill by calendering a defined amount of powder under different process parameters. The analysis is qualitative by the fact that an electrode was formed at all, as well as quantitative by the analysis of the resulting electrode thickness and porosity. The process parameters at which the electrodes have been investigated range from very shear-promoting parameters with high relative and absolute roll speeds to less shear-promoting parameters. The otherwise high temperature and low roll pressure were kept constant according to methods 3.4.1. The results are shown in Fig. 33 and Fig. 34.
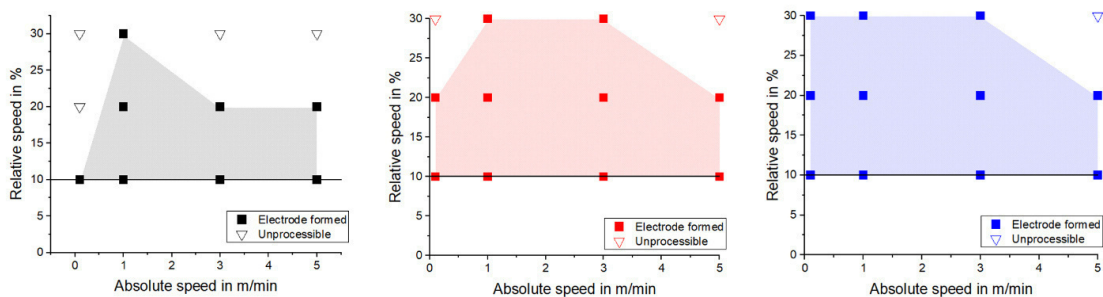
Fig. 33: Qualitative analysis of the processibility of the powder mixtures: LIM (a), MIM (b), and HIM (c). Filled points indicate electrode formation [118].

The LIM showed limited processibility at low absolute speeds or at high speed ratios so that only a few parameter settings resulted in intact electrodes. Thus, the LIM is difficult to process to an electrode for less shear-promoting process parameters, where the speed difference between the rolls is small. The MIM was unable to form an electrode only at 30 % speed ratio and 0.1 and 5 m/min absolute speed, thus showing improved processibility when compared to the LIM. The HIM was unable to form an electrode only at the setting with 30 % speed ratio and 5 m/min absolute speed. The HIM requires less shear-promoting process parameters to be processed to self-supported electrodes. The fact that no mixture formed an electrode at 30 % and 5 m/min is due to limitations in the feeding of the powder. The mass flow of the feed by only gravitation was not sufficient to homogeneously fill the gap between the rolls at such high roll speeds, resulting in holes and cracks during electrode formation. The inability to form electrodes for this setting does not come from the differences in the shear behavior of the powder blends.
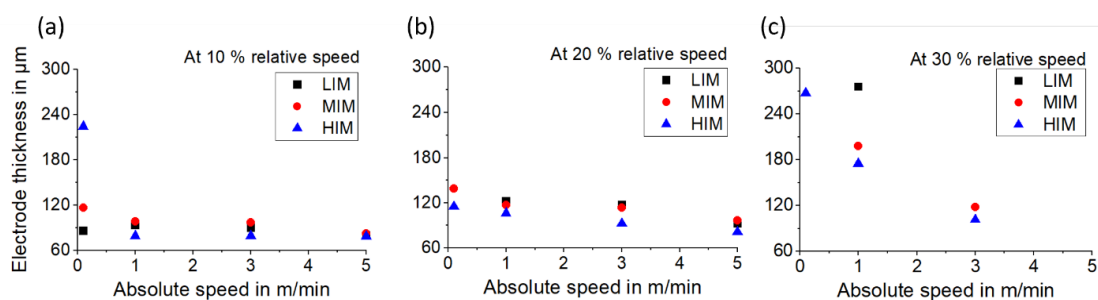
Fig. 34: Electrode thickness of all electrodes produced at different roll speed parameters at 10 % (a), 20 % (b), and 30 % (c) relative roll speed [118].

Fig. 34 shows the resulting electrode thicknesses for the produced electrodes, which have been shown in Fig. 33. At 10 % relative speed all of the electrodes produced at an absolute speed higher than 1 m/min have a low thickness between 80-100 µm. Only the LIM and MIM slightly increase from 80 to 100 µm for these process parameters. At very low absolute speeds the thickness of the MIM and especially of the HIM increase significantly. With an increasing speed ratio between the rolls, the electrode thickness is increasing. At 20 % relative speed a small but clear trend of increasing electrode thicknesses with decreasing absolute roll speed can be seen. Every mixture follows this trend, although the HIM electrode thickness is slightly lower than those of the LIM and MIM for all absolute roll speed settings at 20 % relative roll speed. The electrode thicknesses increase from 80 µm to approx. 140 µm with decreasing absolute speeds. At 30 % relative speed, thus less shear promoting roll speed conditions, not all parameters resulted in functioning electrodes, as also shown in Fig. 33. For the HIM, which did not form an electrode only for the 5 m/min absolute speed setting, the trend of increasing electrode thicknesses with decreasing absolute speeds is more prominent as at lower relative speeds. Here, the electrode thickness increases from 90 µm to approx. 270 µm. The few intact electrodes of the MIM indicate a similar trend while their electrode thickness lies above that of the HIM. The LIM was only able to form an electrode for one of the settings and the resulting electrode thickness is significantly higher than that of the MIM and HIM for the same settings.

4.2.1.3 Electrode Structure

The structure of the resulting electrodes has been investigated by SEM. Cross-sections of the electrodes produced at 10 % relative speed and 3 m/min absolute speed were prepared and analyzed. They were compared to the cross-section of the slurry-based reference electrode. Representative images are presented in Fig. 35.
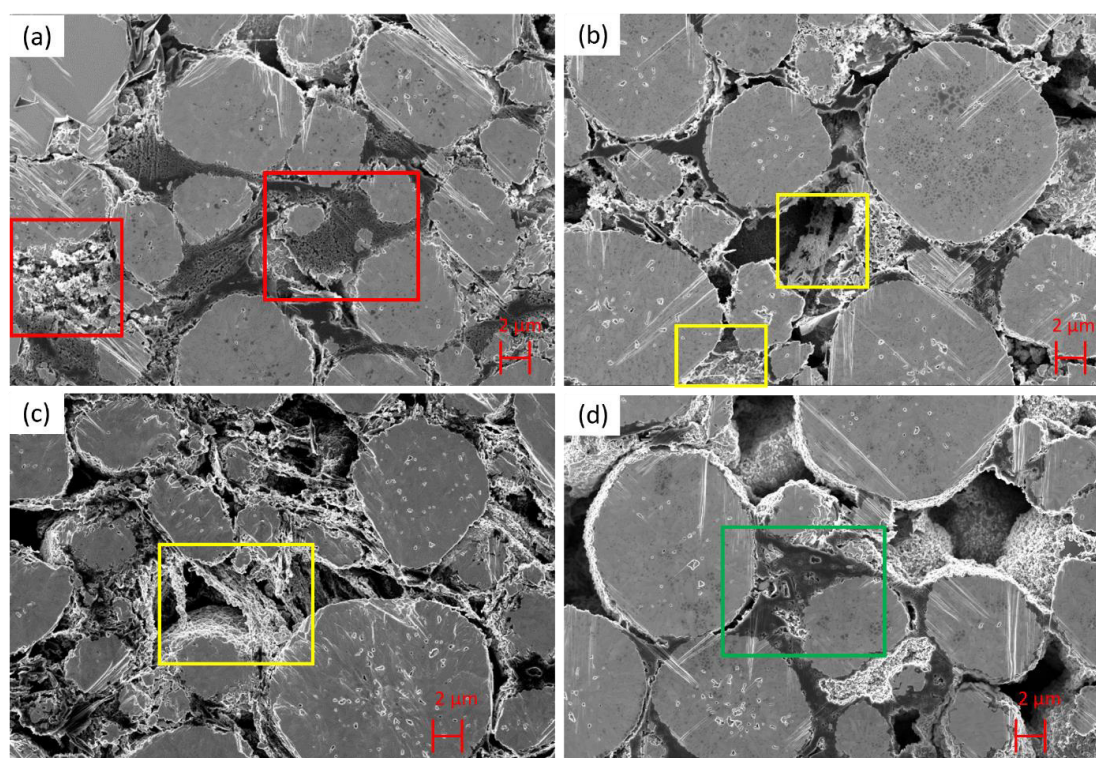
Fig. 35: SEM micrographs of the electrode cross-sections of the LIM (a), MIM (b), HMI (c), and slurry-based reference electrode (d). Red highlights show CB agglomerations, yellow highlights show PVDF filaments and green highlights show PVDF agglomerations [118].

No significant AM particle breakage can be observed for any of the electrodes. The LIM electrode has many inhomogeneities in the form of agglomerates or strongly densified areas. Mainly CB agglomerates are visible and highlighted with red. Also, many areas exist, that are completely devoid of any additives. The electrode made with the MIM does show only a few agglomerates and free AM surface area. PVDF filaments can occasionally be found and are highlighted in yellow. The HIM electrode has very profound PVDF filamentation and seems to have a higher porosity. The filaments bridge and connect the AM particles, while they also incorporate the CB aggregates. Areas with free AM surface are often in close proximity to the filaments. The overall additive distribution seems more homogeneous than in the LIM and MIM electrodes. The slurry-based electrode shows similar characteristics as the LIM electrode with agglomerations of a mixture of PVDF and CB highlighted in green, as well as areas devoid of additives. They indicate an inhomogeneous distribution of the additives. To have a better analysis of the homogeneity of the additive distribution, EDS analysis has been carried out for cross-sections of the same electrodes, the results are presented in Fig. 36.
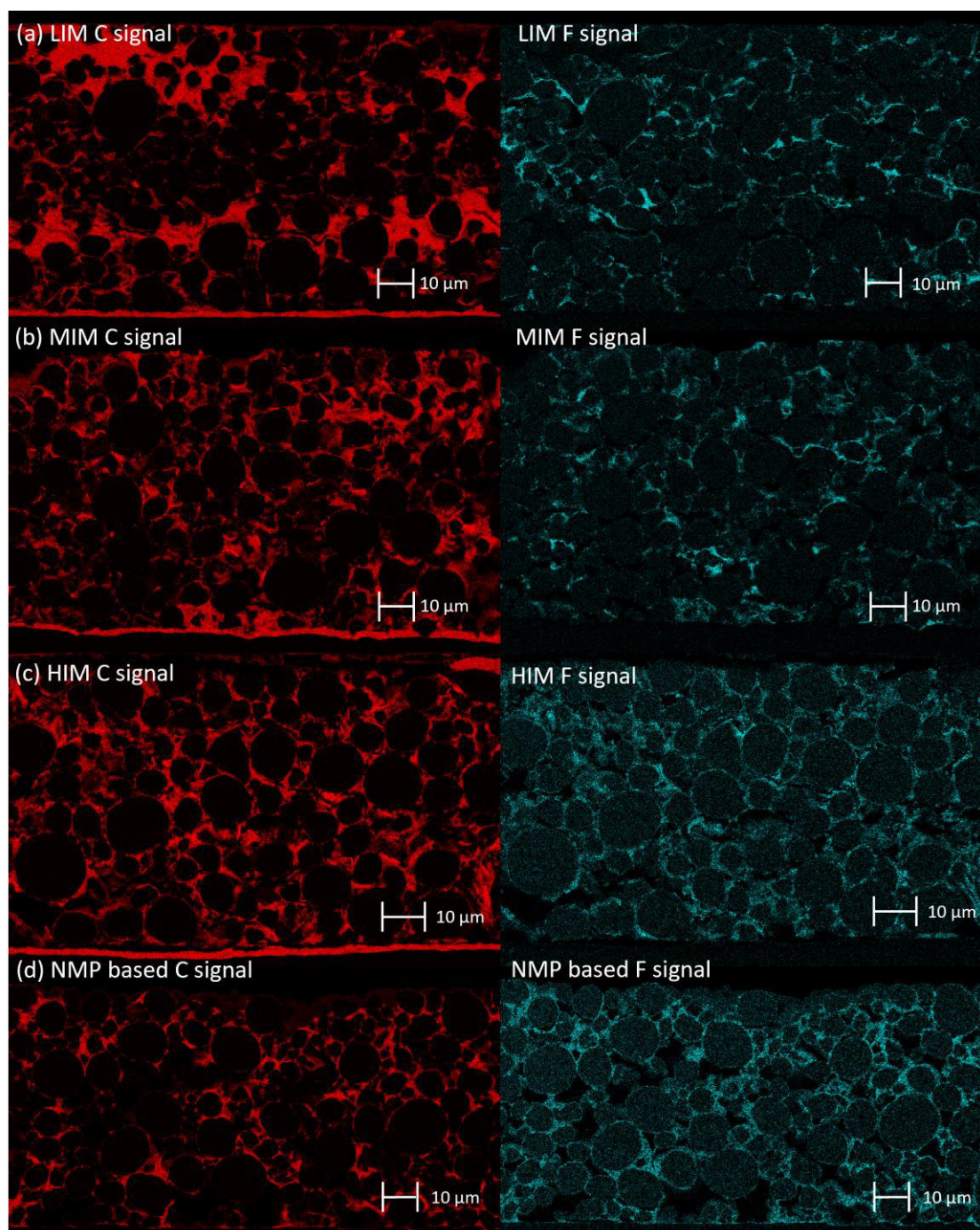
Fig. 36: EDS analysis of the cross sections of the LIM (a), MIM (b), HIM (c) and NMP-based (d) electrodes. The signals for carbon (left) and fluorine (right) are shown [118].

The red color represents the obtained carbon signal, and the blue color represents the fluorine signal. The analysis of the LIM shows big carbon agglomerates between the AM particles, where on the other hand no fluorine signal is detected. These areas represent pure CB agglomerations. On the other hand, in the central part, only low carbon signals are obtained, while fluorine is clearly present. Thus, PVDF is present in these areas without having much CB incorporated. Additionally, large areas devoid of both, CB and PVDF can be seen. These are clearly identified as

the areas, where the separation of single AM particles becomes difficult, due to no carbon and fluorine signals on the AM particle surface. Furthermore, the found agglomerations of CB and PVDF are not linked, meaning they are not found together in a carbon binder matrix, but rather separate from each other. The analysis of the MIM reveals inhomogeneities in form of CB agglomerations as well, but their size is significantly lower than for the LIM. Also, while areas devoid of additives can be found, they are less, as the individual AM particles can be separated more easily. The HIM has a very homogeneous distribution of both, the CB and PVDF. The additives surround most of the AM surface and no big agglomerations can be found. All individual AM particles can be easily separated, thus the AM surface is well covered by both additives. The analysis of the NMP-based electrode shows an inhomogeneous distribution of the carbon signal. Although no big agglomerations are found, some areas are devoid of CB, indicated by the difficult separation of individual AM particles. On the other hand, the fluorine signal is rather homogeneous. The AM particle surface is well covered by the PVDF. Some interparticular spaces are filled with binder, resulting in small agglomerations. Other interparticular spaces are empty of additives, resulting in open pores.

4.2.1.4 Electrochemical Performance Analysis

The electrochemical performance of the dry produced electrodes has been analyzed by C-rate capability tests, long-life cycling, and cyclic voltammetry and has been compared to the NMP-based electrode. Fig. 37 shows the specific discharge capacities of all electrodes with their standard deviations in a half-cell setup. The electrode properties are given in Tab. 11. The exact procedure is given in 3.6.

Tab. 11: Electrode characteristics of the cells measured in the C-rate capability test.

Electrode	Thickness in µm	Porosity	AM Mass loading in $\frac{mg}{cm^2}$
LIM	86.9 ± 6.7	0.35 ± 0.02	22.3 ± 1.3
MIM	81.7 ± 1.4	0.34 ± 0.01	21.4 ± 0.8
HIM	72.1 ± 4.4	0.30 ± 0.02	20.1 ± 1.2
NMP based	63.5 ± 0.1	0.30 ± 0.01	17.5 ± 0.1
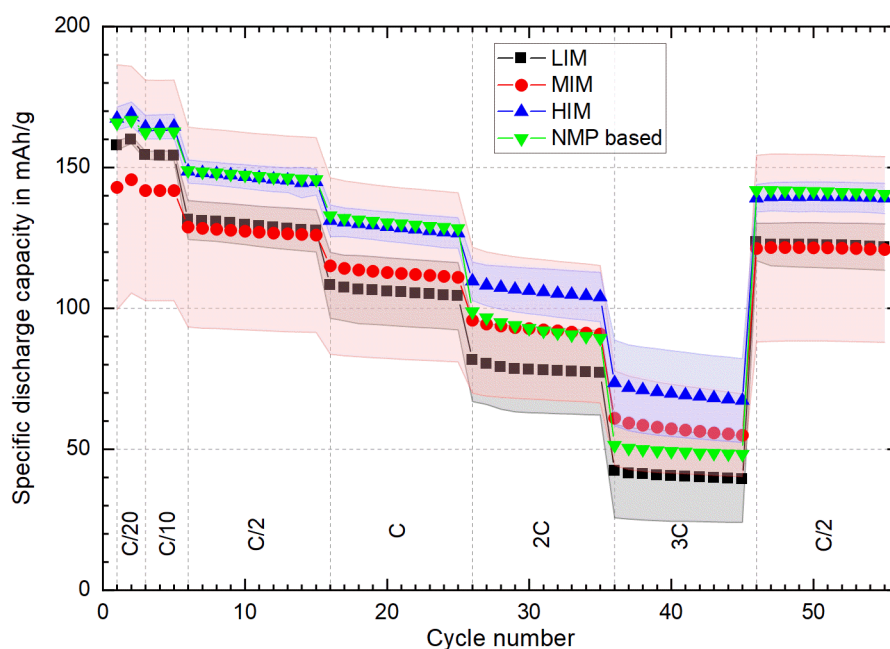
Fig. 37: C-rate capability test of the dry manufactured electrodes made with the LIM, MIM, and HIM mixtures compared to the NMP-based electrode. Charging rates are limited to a maximum of 1C to prevent lithium plating. Constant voltage step with a current cutoff according to 50 % of the respective charge C-rate. Average of five cells [118].

The initial specific discharge capacity (SDC) of the HIM and NMP-based electrodes are approx. 169 mAh/g, which is a good value for NMC622 with a theoretical capacity of 175 mAh/g. The LIM lies lower with approx. 160 mAh/g, indicating, that not all of the AM particles in the electrode participate in the charge transfer reaction. The initial SDC of the MIM lies significantly lower with approx. 145 mAh/g, but has a very high standard deviation, indicating strong differences in the analyzed cells. With increasing C-rate the SDC of all electrodes naturally decreases. At 1C the HIM and NMP-based electrodes perform very similarly, while the LIM decreases more rapidly than the MIM. At C-rates above 1C, the SDC of the NMP-based electrode decreases drastically and reaches at 3C a value almost as low as the LIM with 49 mAh/g compared to 40 mAh/g, respectively. The HIM retains the highest SDC at 3C with approx. 70 mAh/g followed by the MIM with 58 mAh/g. Although the MIM starts the measurement with a significantly lower initial SDC, the performance of the MIM remains parallel to the HIM with increasing C-rates. With respect to the absolute SDC values, this indicates a very similar rate capability of the electrodes. After returning to C/2 all electrodes regained their previously measured SDC of this C-rate. Thus, no degradation mechanisms of either AM or CB-binder matrix are expected after the induced strain at higher C-rates.

To further investigate the cycling performance especially at higher charging and discharging rates, cyclic voltammetry has been conducted with voltage steps, that roughly equal charging rates when converted to the respective C-rates. Thus, Fig. 38. Compares the current responses

during cyclic voltammetry of the same electrodes as in Fig. 37 at voltage steps of 0.017 mV/s and 0.17 mV/s, which correspond to a charging time equal to those of C/20 and C/2.

(a)   (b)
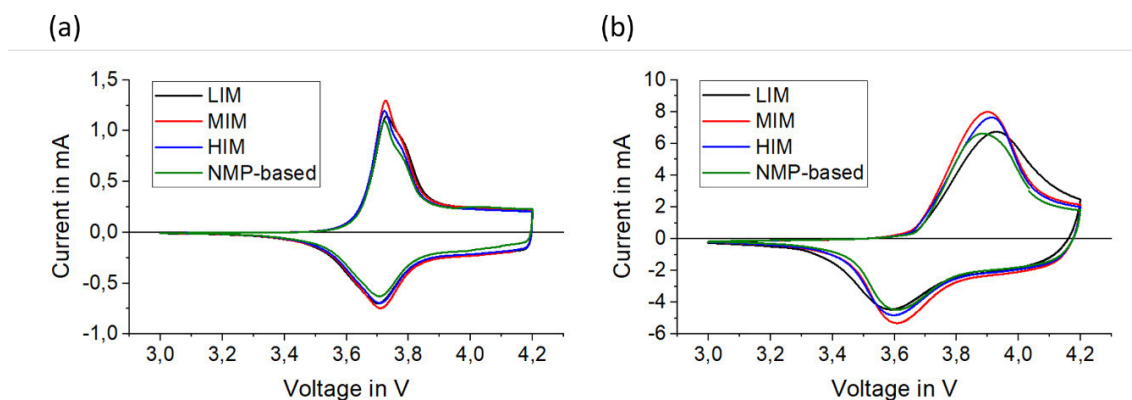
Fig. 38: Cyclic voltammetry of the dry manufactured electrode made with the LIM, MIM, and Him mixtures compared to the NMP-based electrode at voltage steps of 0.017 mV/s (a) and 0.17 mV/s (b) [118].

During charging at a low voltage step of 0.017 mV/s a major current peak at 3.73 V is observed, which has a small shoulder at approx. 3.8 V. During discharge, the main peak is measured at 3.71 V and no side peak can be identified. The potential difference between the redox reactions during charge and discharge is very small at this voltage step. Thus, at very low charging rates, the electrodes behave electrochemically identical. At a higher voltage step rate of 0.17 mV/s the current peak during charging shifts to a higher potential of approx. 3.9 V. Although the potential difference of the current peaks during charging is similar, the LIM can be identified to have a slightly higher potential and the NMP-based electrode has a slightly lower peak potential. The potential during discharge shifts to lower potentials of approx. 3.6 V. Here as well, the LIM shows a stronger shift, thus having a slightly lower current peak potential than the other electrodes. Therefore, the overall difference between charge and discharge peak potential is highest for the LIM, showing an increased overpotential.

Finally, the long-life cycle stability of the electrodes has been investigated. For this, the cells have been cycled for 1000 cycles with a symmetric C-rate of 1C. Every 50th cycle was conducted at C/20 to relax the cells and allow for a more precise investigation of the cells' potential evolution along the course of their cycle life. The results of their cycle life analysis are shown in Fig. 39.
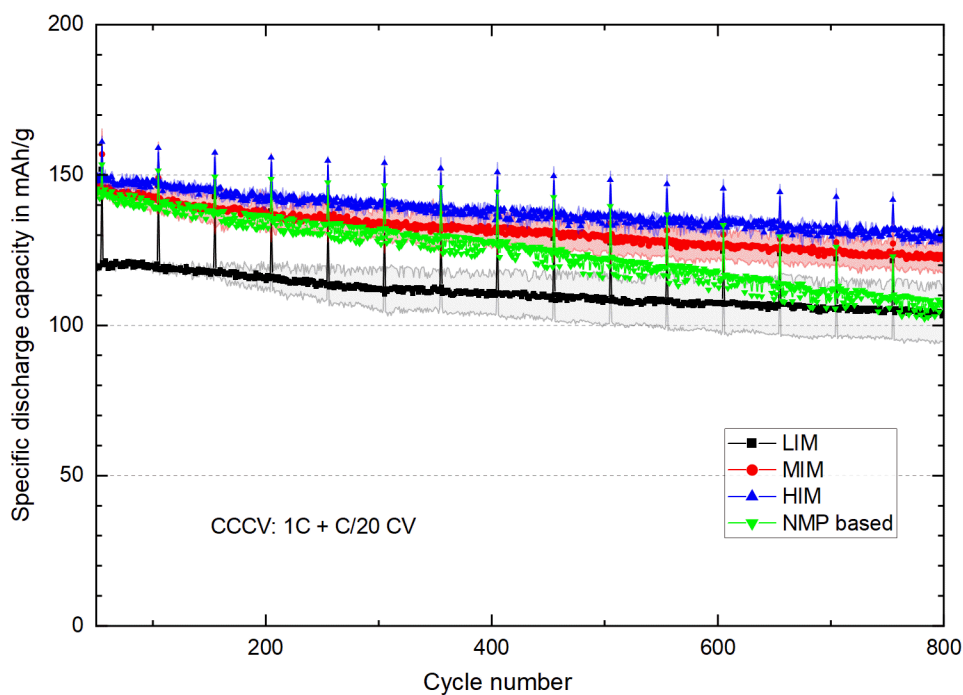
Fig. 39: Long-life cycling stability of the dry manufactured electrodes made with the LIM, MIM, and HIM mixtures compared to the NMP-based electrode. Symmetric cycling at 1C with a constant voltage step at a cutoff current equal to C/20 [118].

The discharge capacities of the MIM, HIM, and NMP-based electrodes at the start of the long-life cycling test are very similar, with 149 mAh/g, 145 mAh/g, and 143 mAh/g, respectively. The SDC of the LIM is significantly lower at 120 mAh/g. This behavior translates well from the C-rate capability tests, where the performance of the HIM, NMP-based and the MIM (after taking the low starting capacity into account) was similar at 1C, while the LIM already shows lower rate capability. The higher absolute values for the measured discharge capacities compared to the C-rate capability test come from the slightly different charging program, where in long life cycles the cutoff current of the CV charging step is at C/20 instead of C/2 for the C-rate capability test. The curves of the discharge capacity of the dry manufactured electrodes run almost parallel, showing a similar degree of capacity loss with approx. 18 mAh/g, 15 mAh/g, and 14 mAh/g for the HIM, MIM, and LIM, respectively. Due to the minor differences in capacity loss between the dry-manufactured electrodes, the same degradation mechanisms are expected. The NMP-based electrode, although starting at a similar SDC as the HIM and MIM, shows a higher capacity loss during long-life cycling of approx. 36 mAh/g after 800 cycles.

4.2.2 Discussion

The prepared mixtures show a different degree of additive deagglomeration and redistribution as can be seen in the SEM micrographs in Fig. 31. Also, the high resistivity of the LIM indicates, that CB deagglomeration did not take place during mixing. In its agglomerate state, the used amount of 2.5 w% CB in the investigated composition is not enough to establish good long-range conductivity through the measured powder bulk, since the CB is highly locally concentrated. SEM micrographs of the MIM indicate a good degree of additive deagglomeration due to the existence of only a few intact additive particles. Additionally, the MIM has a significantly lower powder resistivity compared to the LIM, thus the CB is able to provide good conductivity through the powder bulk. The more homogeneously distributed CB in the form of smaller aggregates can form a sufficient conductive network. With more intensive mixing parameters the agglomerates in the HIM are completely deagglomerated. Furthermore, by sequential mixing steps the resulting CB aggregates and the PVDF primary particles are homogeneously redistributed on the AM surface, first the PVDF, then the CB. A fine layer of additives is attached to the AM surface. While the pure PVDF would act as an insulator, the surface covering CB renders most of the surface area electrically conductive. This very homogeneous distribution of the additives results in the lowest measured powder resistivity of all three mixtures.

The additive distribution homogeneity also translates into the processability of the powder blends. Since the additives have different contributions to the overall shear behavior of the mixture, their degree of deagglomeration and distribution in the particle bulk affects the internal friction coefficient of the particulate system. The analysis of the DIFC in Fig. 32 shows, that CB has a detrimental effect on the shear behavior by increasing the friction coefficient. This can be attributed to the very rough structure of the CB particles and aggregates, causing strong mechanical interlocking, thus strongly resisting granular shear. On the other hand, a homogeneous distribution of all the additives leads to a reduction in the DIFC of the whole particle system. Graphite, being known as a solid lubricant, leads to a significant decrease in DIFC. Not only does the graphite have a low local friction coefficient due to the plate-like flat surfaces, but also has the potential to delaminate under increasing shear forces [119]. Thus, the graphite easily undergoes plastic deformation to accommodate local stress build-up. Additionally, as pointed out in the literature 2.3.4.5, the introduction of angular particles such as the graphite to a system of round particles improves the shear behavior of the system due to the ability of the angular graphite to rotate [94]. This reduces the volume expansion of the particulate system when shear planes undergo strain deformation. Finally, the homogeneous distribution of the binder primary particles on the AM surface does significantly increase the chance, that a thin layer of PVDF lies between the contact points of different AM particles during granular shear. Hence, the solid shear mechanics become influenced by the introduction of the soft viscoelastic material between the solid interfaces. During shear deformation of the powder bulk, rather than solid friction, the PVDF between the solid interfaces is sheared to fine filaments, as can be seen for the more homogeneous mixtures in Fig. 35. These filaments are the result of the shear deformation of the primary PVDF particles distributed on the AM surface. They connect several AM particles and are responsible for the mechanical stability of the electrode sheet once it exits the calender

gap. Additionally, by incorporating the deagglomerate CB, the filaments establish a good conductive network through the electrode.

The sheer fact that PVDF filaments are formed during calendering is proof of the PVDF taking a significant role in the shear mechanics of the powder bulk. As the roll speed parameters have been investigated for the different powder mixtures in Fig. 33 and Fig. 34, it was observed, that the improvement in DIFC of the more homogeneous mixtures directly translates to a wider processibility window. The ability of the HIM to form electrodes at even low shear promoting roll speed parameters and the lower electrode thickness when compared to the other mixtures shows, that the powder is more easily sheared in the calander gap. Essentially, the shear zone in the gap is larger for homogeneous mixtures. This is a direct consequence of the homogeneous distribution of the lubricating graphite and the fine distribution of the PVDF primary particles. Thus, not only is a homogeneous distribution beneficial for the mechanical strength of the electrode but also for the processibility during calendering. A wider window of process parameters is available and electrode thickness can be controlled on a wider scale with increasing homogeneity of the additive distribution.

Furthermore, the homogeneous distribution of the additives in the powder mixture does translate through the calendering process into the electrode bulk. As the analysis of the electrode cross sections in Fig. 36 shows, with increasing mixture homogeneity also the additive distribution in the electrode bulk is becoming more homogeneous. The calendering step does not significantly change the additive distribution nor leads to their reagglomeration, as it can sometimes be observed in liquid processing when binder migration during drying can occur [29]. With the minimization of agglomerations and areas devoid of additives, the connection of more AM particles to the conductive CB and binder network can be increased and the potential of crack formation due to lacking binder is reduced. Additionally, since the dry manufacturing in a calender does not alter the additive distribution homogeneity, the CB and binder remain linked in the electrode bulk. When compared to the NMP-based electrode in Fig. 36, a very similar PVDF distribution homogeneity has been achieved. Comparing the CB distribution, the NMP-based electrode shows a significantly less homogeneous distribution. The dissolution of the PVDF in slurry-based processes allows a very good distribution of the binder, but the CB can reagglomerate in the slurry and during drying, while in dry processing the CB and PVDF can already be linked together during mixing. By this, the mixing step offers a possible design tool to pre-adjust the CB and binder network and translate it into the electrode by dry manufacturing. This enables the specific design and investigation of CB and binder networks.

The electrochemical performance of the produced electrodes does follow the trend, that higher additive distribution homogeneity leads to better cell performance. The C-rate capability test in Fig. 37 shows that the HIM has the best rate performance at higher C-rates, followed by the MIM and LIM. Although the MIM has a lower initial specific discharge capacity than the HIM, its rate performance is parallel to the HIM. Thus, the difference in additive distribution homogeneity between these two mixtures does not seem to play a big role up to rates of 3C, if the slightly favorable electrode mass loading of the HIM from Tab. 11 is taken into account. The LIM on the

other hand, although having a high initial SDC, at rates of 1C or higher a significant capacity loss is caused by the inhomogeneous CB distribution and slightly increased mass loading. A similar decline in discharge capacity at higher rates for the NMP-based electrodes is caused by the inhomogeneous distribution of the CB, as well. Here, electrode thickness, porosity, and mass loading are the most beneficial of all compared electrodes, thus the additive distribution is assumed to cause the capacity loss. Additionally, since the CB and PVDF in the NMP-based electrode are not strictly linked, even well-connected AM particles by the PVDF might not be well connected to the conductive network due to a lack of CB in these areas. The composition used for the NMP-based electrode is the same as for the dry mixtures but is probably not well optimized for the slurry process. This makes the direct comparison of the NMP-based electrode with the dry produced electrodes difficult and potentially disadvantageous for the slurry-based method.

The cyclic voltammetry analysis in Fig. 38 shows the higher overpotential of the LIM at higher rates. This can be attributed to higher charge transfer resistances due to low CB deagglomeration and inhomogeneous distribution through the electrode bulk. The other electrodes have a quite similar overpotential up to the intermediate C-rates. This falls in line with the observations made in Fig. 37, where capacity retention of the HIM, MIM, and NMP-based electrode declined similarly up to rates of 1C. At even higher rates the cyclic voltammetry data did not deliver meaningful results due to a strong broadening and overlap of the measured current.

The long-life cycling test in Fig. 39 was conducted at a C-rate of 1C, thus the results fall in line with the capability test, that the HIM, MIM, and NMP-based electrodes start with a very similar initial SDC at the start of the measurement. The LIM has a significantly lower SDC due to rate limitations caused by the disadvantageous carbon binder distribution already at 1C. Nevertheless, during cycle life, the curves of the SDC of the LIM, MIM, and HIM remain parallel to each other, thus showing a similar degree of capacity fade, with absolute values of 14, 15, and 18 mAh/g after 1000 cycles, respectively. Therefore, a very similar degradation mechanism can be assumed for the dry-manufactured electrodes. Differences in their additive distribution do not seem to play a significant role in the electrode degradation mechanism, but only in the initial performance of the electrode, especially at higher C-rates. The NMP-based electrode on the other hand starts with a high SDC but shows a stronger capacity fade over its cycle life with 36 mAh/g lost after 1000 cycles. The exact degradation mechanism is yet unclear but has to be caused either by the additive distribution or the influence of the binder dissolution and resolidification. For the dry-manufactured electrodes, the additive distribution did not seem to significantly influence the electrode degradation specifically. Additionally, the additive distribution of the NMP-based electrodes seems quite comparable to the LIM in terms of CB distribution and shows a homogeneous PVDF distribution in the analysis of the cross sections in Fig. 35 and Fig. 36. Therefore, it is assumed, that dissolution and resolidification of the herein utilized binder does have a negative influence on the cycle stability of the electrodes. While during this work no clear answer could be found, it remains a focus for future work on this topic. Possible causes of such a strong degradation mechanism could be changes in the swelling behavior of the binder due to altered crystallinity and a more homogeneous layer of PVDF on the AM surface, blocking ion diffusion during the charge transfer.

Summarized for this chapter, the influence of additive distribution during the premixing of the powders on the processibility and electrochemical performance of the resulting electrodes has been investigated. The deagglomeration and distribution of the additives strongly influences the mechanical behavior of the powder blend during calendering, by influencing the dynamic internal friction coefficient of the powder bulk. A homogeneous additive distribution leads to lower internal friction coefficients due to the lubricating effect of the graphite and the binder, which is present at more particle-to-particle contacts to facilitate shearing. This leads to increased processibility windows during calendering. With increasing additive distribution homogeneity, a wider range of roll speed parameters can be used to produce electrodes. Additionally, due to the improved shear behaviors of homogeneous mixtures, the electrode thickness at otherwise identical process parameters is decreasing, due to a minimization of the compaction zone in the roll mill gap. Thus, a wider range of electrode properties can be produced, generally increasing the dry manufacturing versatility. Not only does the homogeneous distribution of the binder reduce the friction of the powder blend but leads to an increased amount of binder filamentation. These filaments increase the mechanical strength of the electrode and by incorporating the conductive CB, ensure high electric conductivity through the electrode bulk. The electrochemical performance of the resulting electrodes is not only influenced by the additive distribution homogeneity but also the electrode properties that are as well a function of the mixture homogeneity. Thus, a differentiation of the respective effects is difficult. Generally, the performance of electrodes with homogeneously distributed additives is improved due to a mixture of beneficial electrode properties such as reduced mass loading and higher porosity, and lower overpotentials due to a good conductive carbon binder network. The cycle stability of the electrodes does not seem to be influenced heavily by the additive distribution but rather the initial performance of the electrode at the respective C-rate does. But comparing the dry-manufactured electrodes to an NMP-based electrode with the same material composition, a clear difference in the degradation mechanism is expected, due to strong differences in capacity retention after long life cycling. The exact mechanism is yet to be clarified.

4.3 Influence of the Binder

The investigation of the influence of the process parameters and the mixing homogeneity has shown, that the additives significantly impact the shear properties of the whole blend. The friction properties of the CB and graphite itself, as well as their influence on the electrode blend, could be analyzed directly by shear deformation measurements. The influence of the binder, and its property as a lubricant, was only indirectly indicated by the previous investigations through the low friction coefficient of the homogeneous mixture and the strong presence of filament formation. This chapter focuses primarily on the binder and tries to analyze its lubricating property for the dry electrode manufacturing process. Furthermore, the influence of the binder shear strength on the dry powder roll milling process is investigated. The resulting electrode morphology is characterized in dependance on the used binder properties and their electrochemical performance is analyzed.

4.3.1 Results

4.3.1.1 Shear Behavior and Processibility

First, the lubricating character of the PVDF binder was investigated using powder shear measurements like it has been done for the CB and graphite additives in the previous section. Shear measurements of the binder at room temperature proved to be unrepresentative for its role during processing in the roll mill gap due to the binder not being in molten state, thus having significantly different properties than at high temperatures that are used during calendering. Therefore, the measurements with the ring shear cell have been conducted at elevated temperatures, by first preparing the shear cell and the powder sample, then heating the sample to 200 °C and immediately conducting the shear measurement. Although the measurement time has been reduced to a minimum and the sample holder is made of massive steel, thus having a high heat capacity, a constant temperature during the measurement could not be maintained. To counteract this problem, only the first measured point made with each measurement was used. The comparison of the static internal friction coefficient (SIFC) between the HIM at 200 °C and 20 °C (room temperature) is shown in Fig. 40.
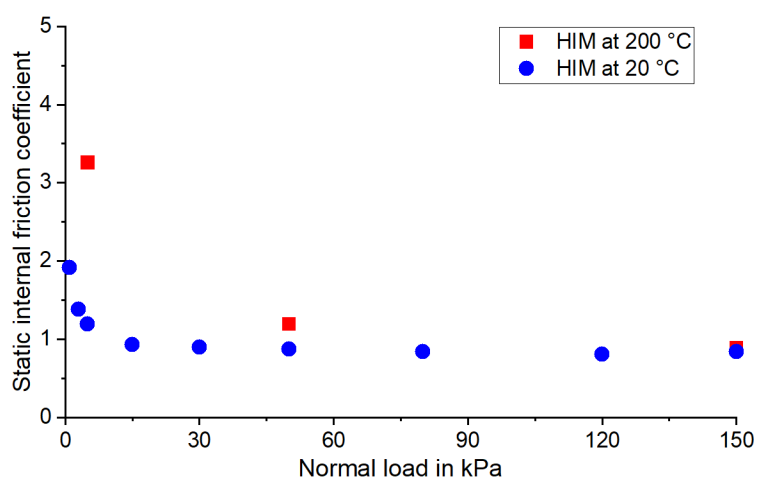
Fig. 40: Measurement of the static internal friction coefficient of the homogeneous electrode mixture at room temperature and 200 °C.

The SIFC at low normal loads is higher for both temperatures than at high normal loads due to the dominance of cohesive and adhesive forces over friction forces. In comparison, the HIM at 200 °C has a significantly higher SIFC at low normal loads than at 20 °C, with values of 3.3 compared to 1.4 at a normal load of 5 kPa, respectively. The SIFC is decreasing for both temperatures with increasing normal load. At 20 °C the SIFC almost reaches a constant value for high normal loads at approx. 1.08, while the SIFC measured at 200 °C still shows a small decline. At high normal loads of 150 kPa (which are still far below the normal loads during calendering), the SIFC of the HIM measured at 200 and 20 °C are almost identical. Since the measurement at 200 °C still shows a decline, it is expected that the SIFC is further decreasing for higher normal loads. Measurements at higher normal loads, that are more representative of the pressures during roll milling, are not possible due to equipment limitations.

The results of the previous sections showed, that upon shearing in the roll mill gap, the PVDF binder undergoes filamentation under the acting shear forces. Thus, the shear strength of the binder was compared to the shear strength of the solid materials. Such a comparison between the shear strength of a solid and a liquid material is unconventional but essentially represents the situation in the roll mill gap during processing. If the shear strength of a battery mixture without binder is higher than the shear strength of a battery mixture with a binder, then the binder acts as a lubricant in this special case. Since the direct measurement of the internal friction coefficient at such high normal loads and temperatures is impossible, the comparison of the shear strength of the single components can be done. Here, the shear strength of the solid mixture without binder can be extrapolated due to the friction coefficient being a constant value for sufficiently high normal loads. In the previous results in Fig. 32, a constant DIFC for normal loads of 150 kPa can be observed, thus extrapolation to high normal loads is possible. The binder on the other hand has a shear strength, that is almost independent of the normal load since the PVDF is in a molten state at a process temperature of 180 °C or 200 °C [120]. In the liquid state,

the shear strength of the binder is rather dependent on the shear rate. A calculation or prediction of the shear rate during processing is difficult to provide, due to the varying gap width and unknown shearing mechanism. Therefore, the shear strength of the binder over a wide range of shear rates is compared to the shear strength of the solid materials over the applied normal load. The shear strength of the solid material is extrapolated from the herein measured DIFC of 0.6 for the pure NMC622 and the shear strength of the binder is taken from dynamical mechanical analysis measurements provided by the binder producer. The results of the comparison are shown in Fig. 41.
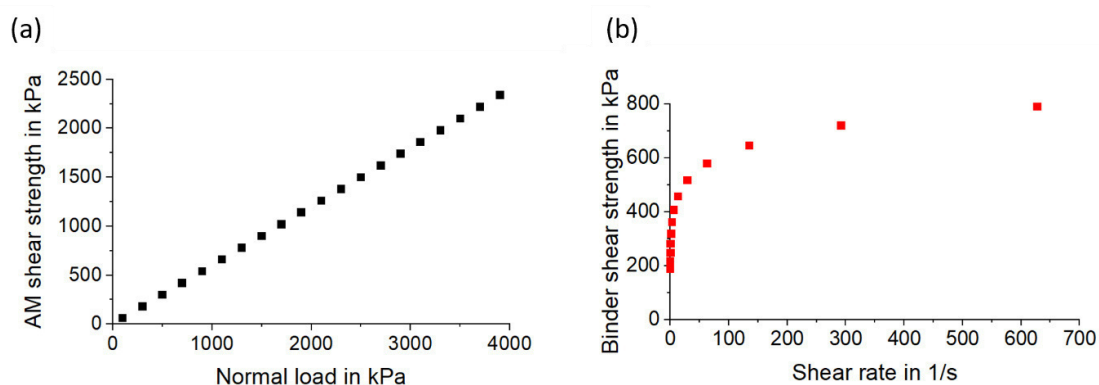
Fig. 41: Comparison of the shear strength of the pure NMC622 AM under increasing normal load (a) and of the Kynar A PVDF binder under increasing shear rate (b).

The shear strength of the pure AM is increasing linearly with the normal load, according to a constant DIFC for such high normal loads. At a normal load of 1300 kPa, the shear strength of the AM is at 840 kPa. The shear strength of the molten binder is almost independent of the normal load but is increasing significantly for high shear rates. For low shear rates, the increase in shear strength is drastic but the increase slows down for very high shear rates. While usually no maximum value is ever achieved, the shear strength can be well approximated for high shear rates at approx. 800 kPa. This shows, for the given assumptions of constant DIFC for the AM and load-independent shear strength for the binder, that the shear strength of the AM surpasses the shear strength of the binder at high normal loads. For the herein investigated material NMC622 and Kynar A, this normal load is reached at approx. 1300 kPa.

To now investigate the influence of the binder shear strength on the roll milling process, four different binders have been used to produce homogeneous battery mixtures according to method 3.3. The binders differ in molecular weight, molecular weight distribution, and copolymer content and distribution. Finally, due to these differences, the binders vary in shear strength, which is the main macroscopic property investigated in this work. A summary of the binder properties is given in Tab. 12.

Tab. 12: Summary of the qualitative binder properties

Binder	Type	Melt temperature in °C	Molecular weight qualitative
Kynar A	Homopolymer	165	Very high
Kynar B	Homopolymer	168	High
Kynar C	Copolymer VF2-HFP	150	High
Kynar D	Copolymer VF2-HFP	165	Medium

The shear strength of the binders has been provided by the producer in the form of their respective complex viscosity relative to the angular frequency of the shear measurement. They were conducted at slightly different temperatures, all above the melting temperature of the binders, the results are presented in Fig. 42.
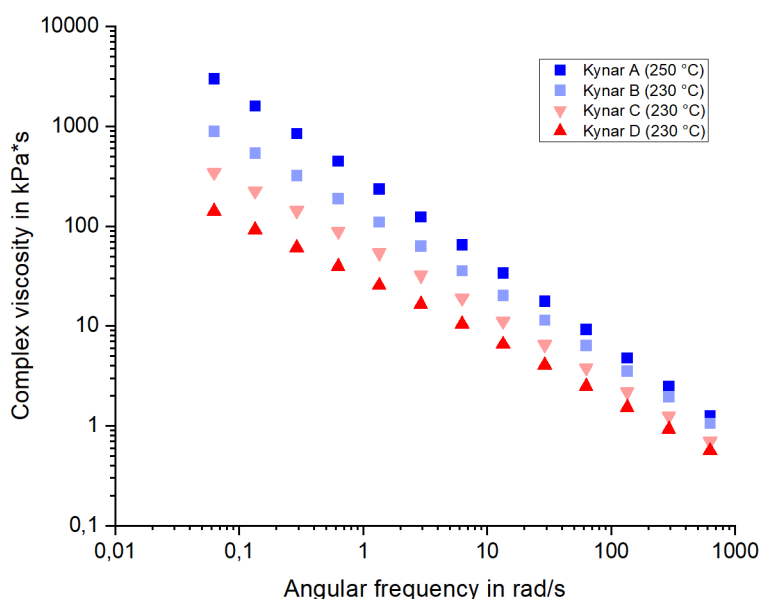
Fig. 42: Complex viscosity of the binders investigated in this chapter.

Kynar A has the highest complex viscosity, followed by Kynar B, Kynar C, and Kynar D with the lowest complex viscosity. All binders have been measured at 230 °C except the Kynar A, which has been measured at 250 °C. Since higher temperatures reduce the elastic behavior of polymers, it can be assumed, that the complex viscosity of the Kynar A at 230 °C would be even higher than at 250 °C, thus it would shift the complex viscosity to even higher values. All binders have relatively high complex viscosity due to their high molecular weight, which makes the measurement at temperatures just slightly above the melting temperature difficult. Although the process temperature in this work is typically at 180 °C, the relative differences in viscosity

between the various polymers remain similar, since they follow the same temperature dependence [121] Thus, in this work it is assumed, that at 180 °C the relation between the different binders is the same as for 230 °C, with the Kynar A having the highest shear strength and Kynar D the lowest, respectively.

During the processing of the battery mixtures with the different binders, the gap width has been recorded to investigate the processibility of the mixtures and to analyze the influence of the binders on the shear behavior of the blend. The results of the measured calender gap width are presented in Fig. 43.
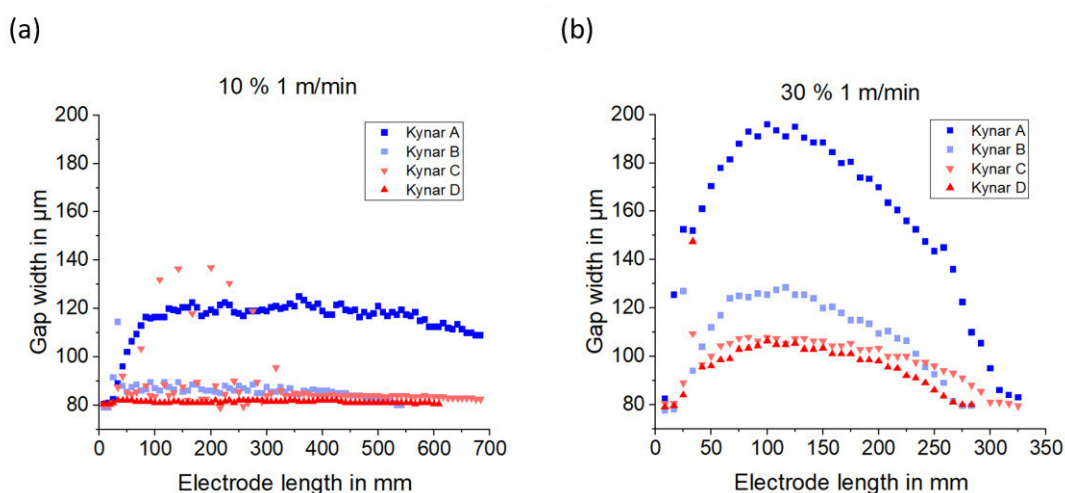
Fig. 43: Gap width analysis during processing of the mixtures with different binders. High shear roll speed parameters of 10 % relative and 1 m/min absolute speed (a) and medium shear roll speed parameters of 30 % relative and 1 m/min absolute speed (b).

At very shear-promoting parameters the mixtures containing Kynar B, Kynar C, and Kynar D can be processed to thin electrode sheets, that have the same or only slightly higher thickness than the initially set gap width of 80 μm. No roll mill gap opening was observed for these mixtures at 10 % relative and 1 m/min absolute speed. For the Kynar C, a few of the measured gap width points show strong deviation, which is assumed to come from irregularities on the roll mill surface during processing, such as material residue in the form of adhering agglomerates. A perfect cleaning of the roll between measurements is not possible, thus such deviations cannot be always avoided. The mixture containing Kynar A on the other hand did cause the roll mill gap to increase to approx. 120 μm until an almost steady state has been reached.

The gap widths during processing with the less shear promoting parameters of 30 % relative speed and 1 m/min absolute speed are shown in Fig. 43(b). Here, all battery mixtures caused an increase in the measured gap width due to the opening of the rolls. The Kynar A caused the strongest increase in gap width up to approx. 200 μm. The mixture containing the Kynar B is the blend to cause the second strongest increase in roll gap width, up to approx. 120 μm. The Kynar C and Kynar D mixtures both lead to a small increase of the gap width to approx. 100 μm.

4.3.1.2 Electrode Structure

The resulting electrodes were optically and mechanically very different. They have been analyzed by SEM to investigate their morphology. The results are shown in Fig. 44.
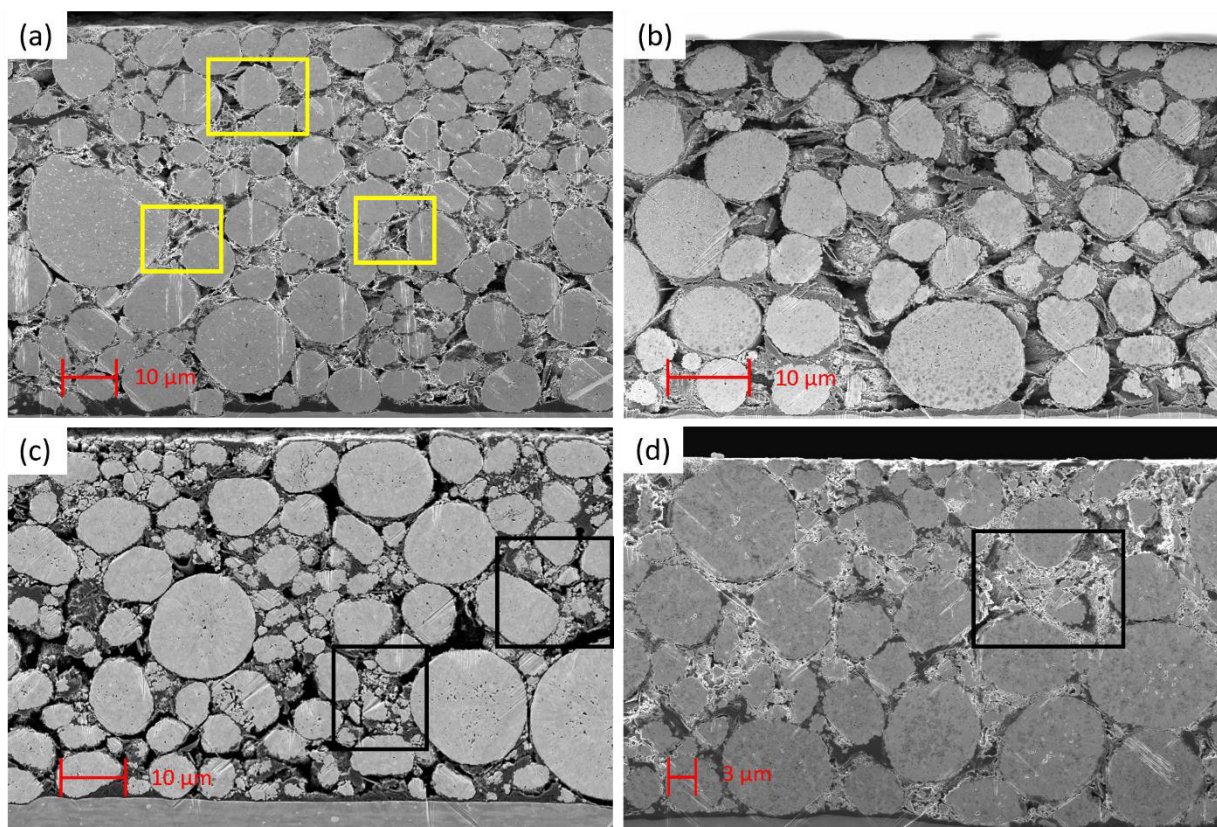
Fig. 44: SEM micrographs of the produced electrodes with different binders: Kynar A (a), Kynar B (b), Kynar C (c), and Kynar D (d). Kynar A filaments are highlighted yellow and AM particle breakage is highlighted black.

Kynar A and B electrodes do not show signs of fractured AM particles or strong agglomerates of either CB or binder. PVDF filamentation is highlighted in yellow for the Kynar A, while it is very dominant in the Kynar B electrode. Qualitatively, both electrodes possess sufficiently high porosity and a homogeneous distribution of the components. The Kynar C and D electrodes both show signs of fractured AM particles, highlighted in black. No binder filamentation can be detected for either of the two electrodes. The Kynar C electrode has an open pore structure, but the Kynar D electrode is almost completely dense. Only very few pores are detectable and spaces between AM particles are filled with carbon binder domains instead of open pores.

Additionally, the surface structure has been analyzed by white light interferometry. A comparison between the electrodes is shown in Fig. 45.
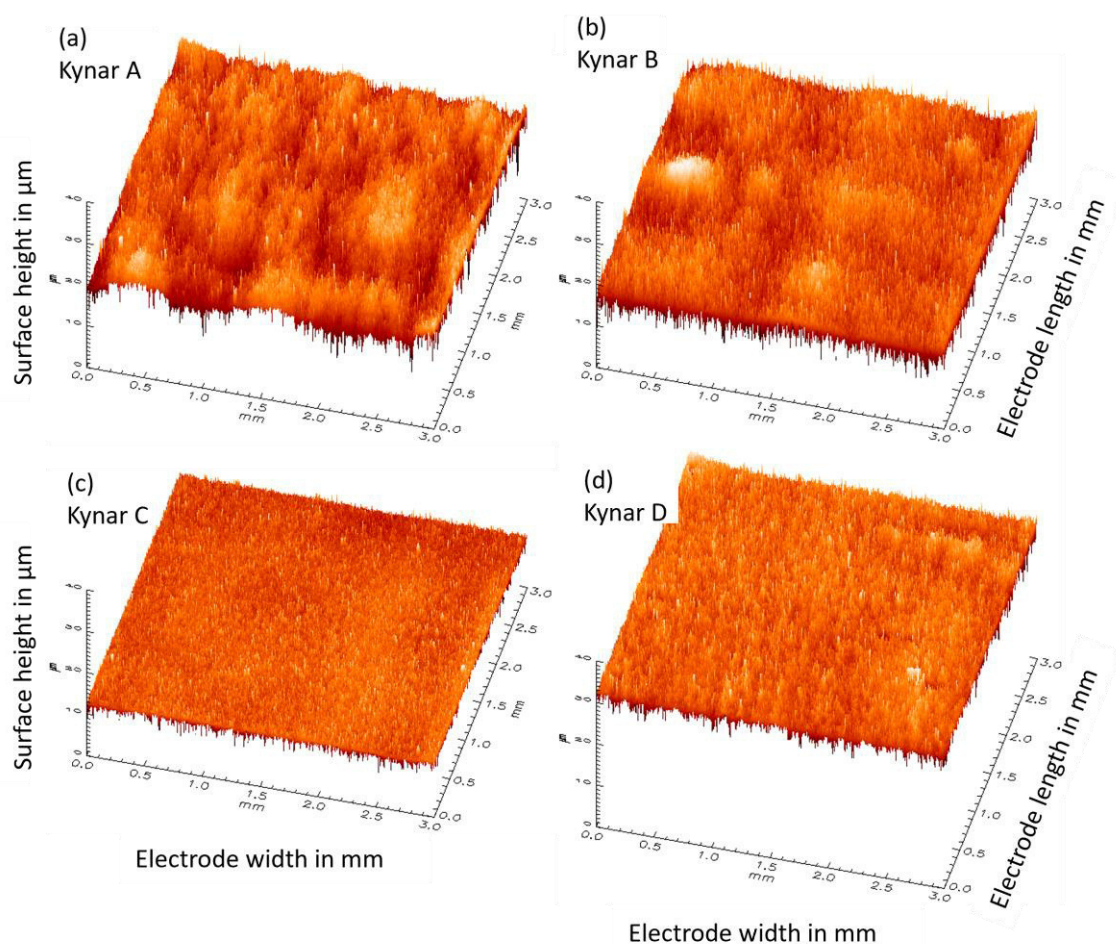
Fig. 45: 3D surface analysis of the electrodes produced with different binders: Kynar A (a), Kynar B (b), Kynar C (c) and Kynar D (d).

The surface of the Kynar A electrode shows the already investigated (Fig. 29) periodic wave-like structure, indicating stress build-up and release. The surface of the Kynar B electrode is smoother compared to that of the Kynar A electrode. Also, irregularities in surface height are significantly less and if a wave-like structure can be observed, peaks and burrows of the stress build-up and release are less regular and sharp. The surfaces of both, the Kynar C and D electrodes are significantly more flat compared to the Kynar A and B electrodes. The Kynar C electrode surface does have no irregularities in surface height. The Kynar D electrode surface has no periodic irregularities, but has many small local peaks compared to the Kynar C electrode. This indicates a microscopically higher surface roughness and area.

Finally, the electrochemical performance of the electrodes has been analyzed concerning their thickness and porosity. The results always have to be set into relation to the electrode porosity and thickness, since these properties significantly influence the cycling performance [67]. Additionally, due to the different binder properties, the morphology of the electrodes differs significantly even for the same process parameters. Fig. 46 summarizes the range of the porosity and thickness, that could be achieved with the investigated process parameters for each binder.
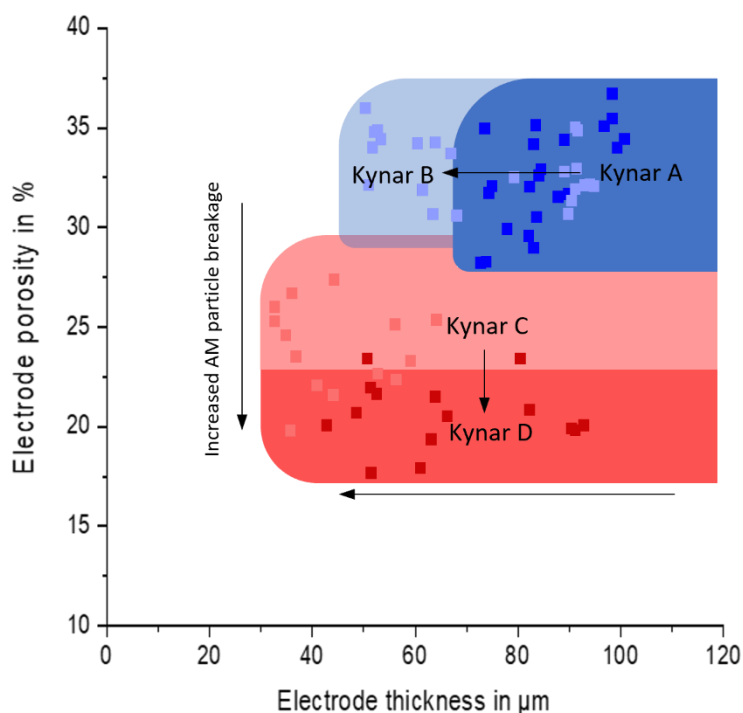
Fig. 46: Qualitative summary of the possible electrode porosity and thickness that can be achieved with the use of the respective binder.

All binders have a maximum porosity of approx. 0.35 for the herein-used process parameters and mixtures. The attempt to produce electrodes with porosities above 0.35 resulted in no electrode formation due to low mechanical strength, indicating, that a critical compaction is necessary to establish a sufficiently high contact interface between the binder and the other solid materials. The Kynar A and B binders have a minimum porosity of approx. 0.28. Higher compaction to reduce porosity is not possible due to the high resistance of the powder against compaction, resulting in gap opening and finally thicker electrodes. The Kynar B binder is able to produce electrodes with a lower thickness compared to the Kynar A, with a minimum thickness of 45 µm compared to 70 µm, respectively. The Kynar C and D binders show a similar processibility window, both being able to produce thin electrodes of 30 µm and low porosities down to 0.19. For all binders and electrodes with the same composition, the mechanical strength decreases for low thicknesses due to the reduction of contact points between the particles. Also, a reduction of the electrode porosity is linked with higher compaction, thus higher stresses on the particles, leading to the plastic deformation of the AM. Particle breakage is especially prominent when electrode porosity is reduced below the tap density of the used material mixture, thus approx. below 28 % porosity.

4.3.1.3 Electrochemical Performance Analysis

Since the properties of the different binders, especially the Kynar A and B, limit electrode production to a specific thickness and porosity range, the comparison of the electrochemical performance of the electrodes is done concerning these limitations. First, the C-rate capability of all electrodes is compared. For this, electrodes with a similar thickness have been cycled in a coin cell setup. The porosity and mass loading of these electrodes vary significantly, as can be seen in Tab. 13. The results of the C-rate capability test are shown in Fig. 47.

Tab. 13: Electrode properties of the cells used for the C-rate capability test.

Electrode	Thickness in µm	Porosity	AM Mass loading in $\frac{mg}{cm^2}$
Kynar A	71.1 ± 3.9	0.31 ± 0.02	20.1 ± 1.2
Kynar B	85.9 ± 0.5	0.33 ± 0.01	24.2 ± 0.4
Kynar C	81.4 ± 6.2	0.21 ± 0.02	27.2 ± 2.7
Kynar D	73.3 ± 0.2	0.26 ± 0.02	22.8 ± 0.5
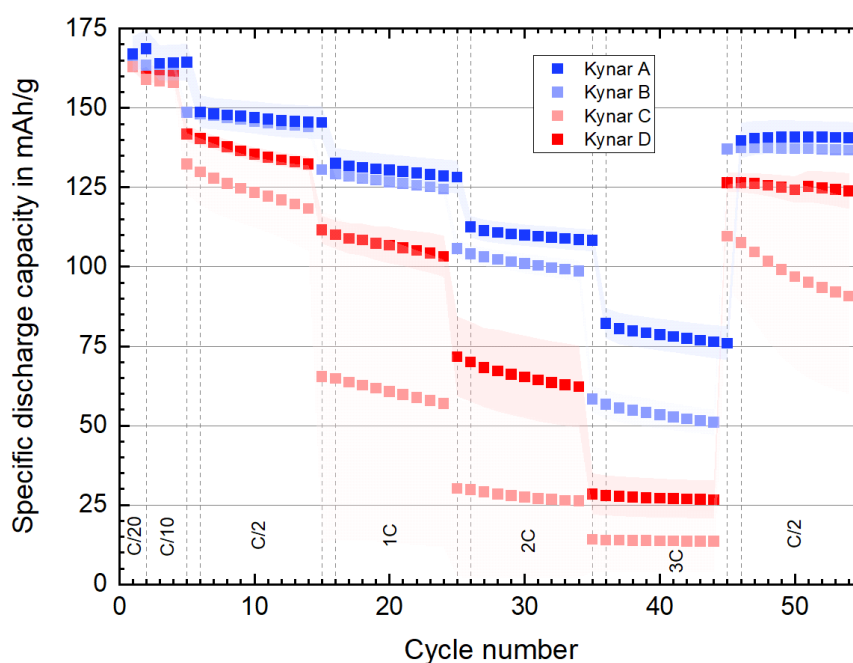
Fig. 47: Results of the rate capability test comparing electrodes produced with different binders. Maximum of 1C charging used at higher discharge rates. CV step with a cutoff current of C/20 included.

All tested electrodes start with similar SDCs of approx. 165 mAh/g. With increasing C-rates the Kynar A and B electrodes retain a higher SDC compared to the Kynar C and D electrodes. First differences in SDC between the Kynar A and B electrodes can be observed at C-rates of 2C and higher. Here, the difference in AM mass loading between the Kynar A and B electrodes has to

be noted. For the Kynar C and D electrodes, the SDC is decreasing already at C/2 significantly, with the Kynar D electrode performing better than the Kynar C electrode. The very high AM mass loading and low porosity of the Kynar C electrode have to be noted. Taking into account the morphology of the electrodes, a correlation between low porosity, high mass loading, and decreasing discharge capacities can be seen.

As demonstrated in Fig. 46, the porosity of the electrodes cannot be controlled precisely by the process, since the major factor influencing the electrode porosity is the binder type and its mechanical behavior during shearing in the roll gap. Therefore, a comparison of all four different types of electrodes at similar porosities is not possible. To further investigate the influence of mass loading on rate capability, it was necessary to compare electrodes with different mass loading but as similar porosity as possible from one specific electrode type. For this, Kynar D electrodes have been compared, due to the most similar achieved porosities. Thus, the mass loading and consequently also the electrode thickness varies. The cell characteristics are given in Tab. 14 and the results of their C-rate capability analysis are shown in Fig. 48.

Tab. 14: Electrode properties of the Kynar D cells used for the investigation of the influence of the mass loading on the rate performance.

Electrode	Thickness in µm	Porosity	AM Mass loading in $\frac{mg}{cm^2}$
Low mass loading	30.4 ± 0.8	0.26 ± 0.02	9.5 ± 0.01
Medium mass loading	45.5 ± 1.8	0.31 ± 0.03	13.3 ± 0.01
High mass loading	73.4 ± 0.5	0.29 ± 0.01	22.0 ± 0.01
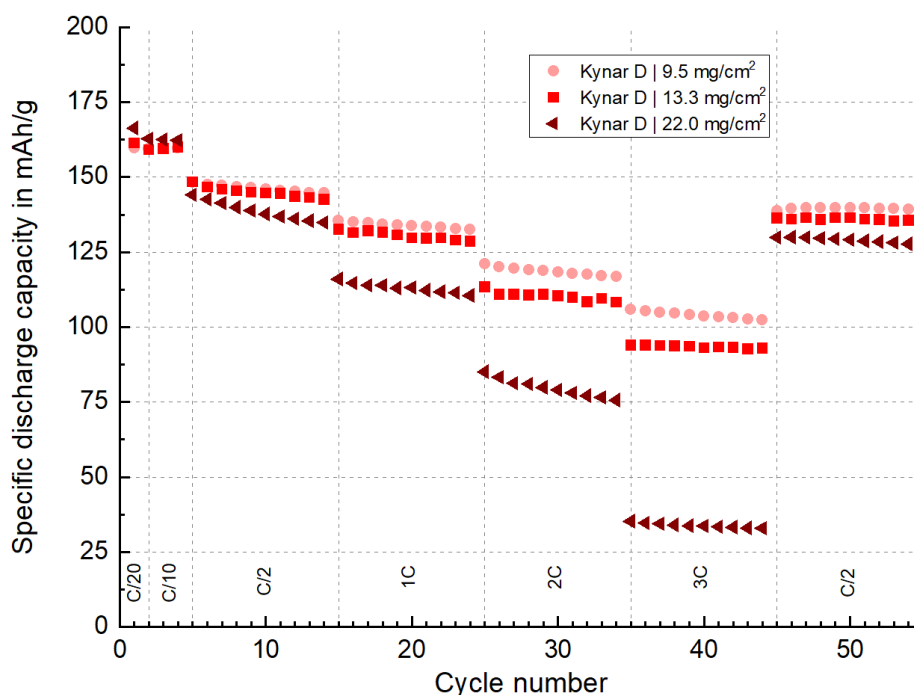
Fig. 48: C-rate capability test of Kynar D electrodes with similar porosities but different AM mass loadings.

The initial SDC during the formation step is highest for the high mass loading electrode with 166 mAh/g compared to the low and medium mass loading electrode with 161 mAh/g,. With increasing C-rate, all electrodes decrease in their SDC. Relatively seen, the high mass loading electrode has a higher capacity fade at a C-rate of C/2, while a difference in capacity fade between the medium and low mass loading electrode is observed only for C-rates of 2C or higher. At 3C the difference in SDC between the medium and low mass loading electrodes is still small. The SDCs at 3C are at approx. 103 mAh/g, 92 mAh/g, and 33 mAh/g for the low, medium, and high mass loading electrodes, respectively.

To further investigate the influence of the mass loading on cell performance, the dQ/dV plots of the same measurement at different C-rates have been constructed and shown in Fig. 49 for a C-rate of C/10 and C. It is helpful to better characterize the cause for the discharge capacity fade of the electrodes.
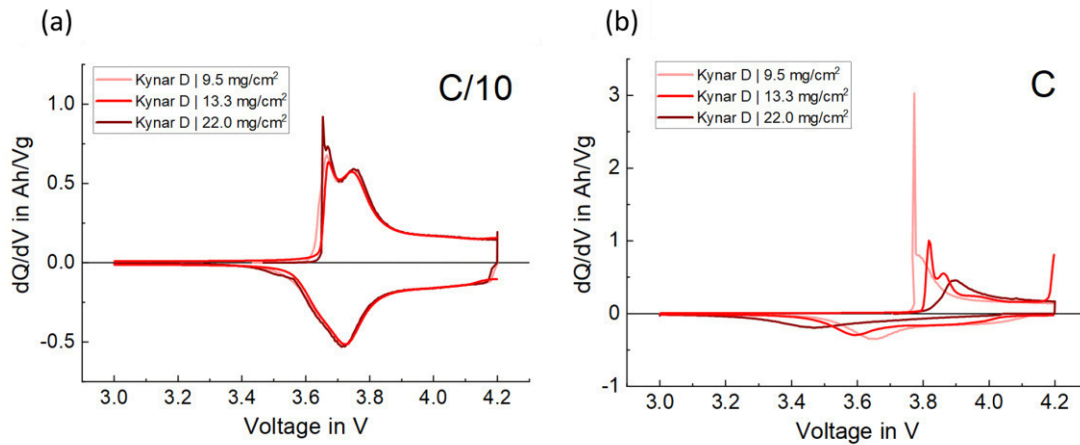
Fig. 49: Analysis of the current evolution along the cell potential in the form of a dQ/dV plot constructed from the C-rate capability test of the Kynar D electrodes. Comparison at a C-rate of C/10 (a) and 1C (b).

At low C-rates, such as C/10, the current peaks during charging and discharging of all the electrodes with different mass loadings lie at almost the same potential, meaning no overpotentials at this specific C-rate. No electrode experiences any limitations in the form of additional resistances, that differentiate it from the others. At a higher C-rate of 1C, the current peaks during charging shift to higher potentials with increasing mass loading, while during discharge the current peaks shift to lower potentials, respectively. Therefore, electrodes with a higher mass loading have a higher overpotential, caused by additional resistances during cycling at higher C-rates.

For the investigation of the influence of the electrode porosity on the rate performance, electrodes with very similar thickness and mass loading, but different porosity made of the Kynar D have been compared. Cell characteristics are given in Tab. 15 and the results of the C-rate capability test are shown in Fig. 50.

Tab. 15: Properties of the Kynar D electrodes used for the investigation of the electrode porosity on the rate performance of the cell.

Electrode	Thickness in µm	Porosity	AM Mass loading in $\frac{mg}{cm^2}$
Low porosity	73.0 ± 0.9	0.24 ± 0.01	23.3 ± 0.01
High porosity	73.4 ± 0.5	0.29 ± 0.01	22.0 ± 0.01
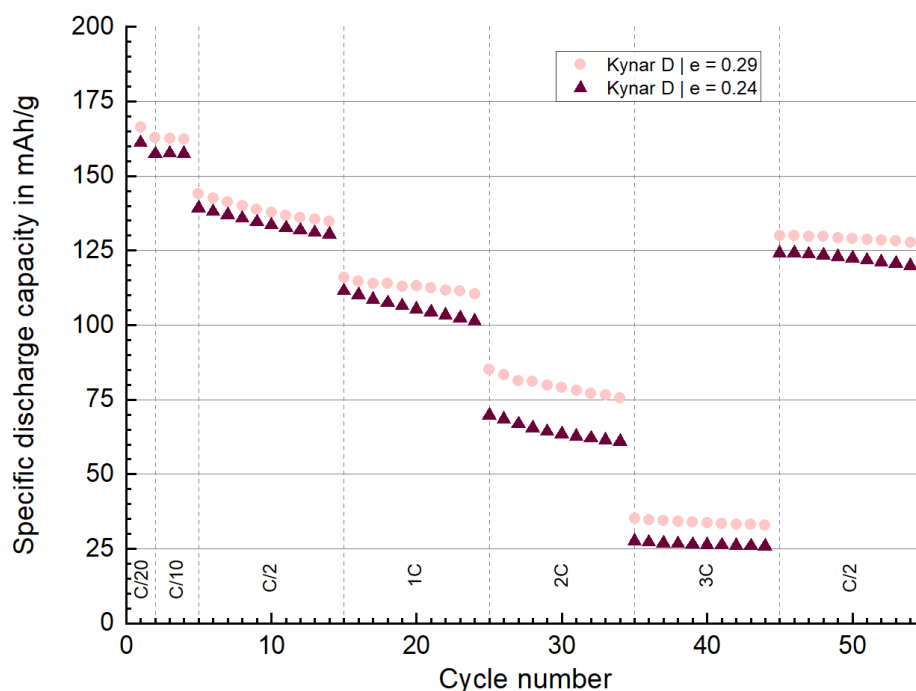
Fig. 50: Rate capability test of Kynar D electrodes with similar mass loading but different porosities.

The electrodes with different porosities have a slightly different initial SDC in the formation step with approx. 166 mAh/g and 161 mAh/g for the high and low porosity electrode, respectively. Taking this difference into account, the first differences in C-rate capability can be seen at 1C, where the SDC of the low porosity electrode is decreasing more rapidly. While the difference in SDC between the electrodes remains at approx. 15 mAh/g during the C-rate of 2C, the difference is decreasing to 7 mAh/g at 3C. This indicates that ion diffusion limitations between these two investigated electrodes are significant at charging rates of 1C and 2C. At 3C both electrodes indicate insufficient ion diffusion, resulting in very similar capacity retention. For a fair comparison, the slightly higher mass loading of the low porosity electrode has to be noted, since the investigations shown in Fig. 48 and Fig. 50 indicate, that mass loading has a stronger influence on rate capability than the electrode porosity.

Although the electrodes made with different binders have quite different morphological properties, a comparison of their long-life cycling has been done to investigate their degradation during cycle life. Fig. 51 shows the specific SDC of the electrodes over 1000 cycles. The cycling program used for the Kynar A electrodes is only different by the relaxation cycle at C/20 once every 50 cycles. The electrode morphologies are given in Tab. 16.

Tab. 16: Properties of the electrodes produced with different binders used in the long-life cycling test.

Electrode	Thickness in μm	Porosity	AM Mass loading in $\frac{mg}{cm^2}$
Kynar A	67.9 ± 1.7	0.33 ± 0.01	19.3 ± 0.6
Kynar B	51.1 ± 3.9	0.35 ± 0.01	14.0 ± 1.1
Kynar C	46.1 ± 0.9	0.22 ± 0.01	15.2 ± 0.5
Kynar D	34.3 ± 4.2	0.20 ± 0.01	11.6 ± 1.3
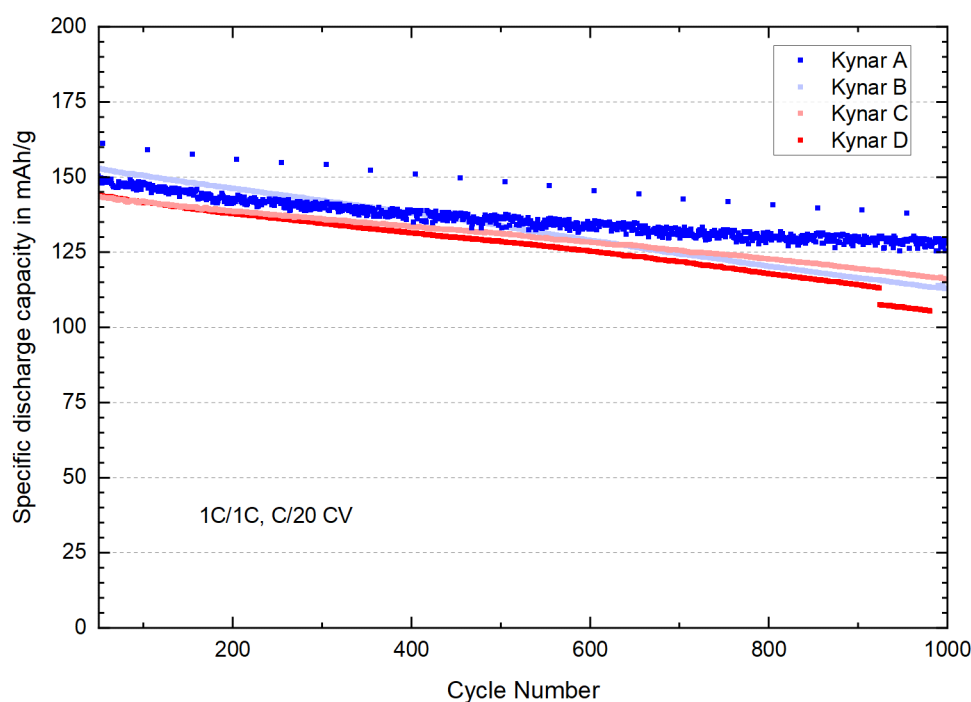
Fig. 51: Long-life cycling test of electrodes produced with different binders. Symmetric cycles at 1C with a CV step at a cutoff current of C/20. For the Kynar A electrode a relaxation step of C/20 every 50th cycle is included.

The Kynar A electrode has an SDC of 149 mAh/g at the start of the cycle life measurement and retains an SDC of 128 mAh/g after 1000 cycles, resulting in a difference of 21 mAh/g. With respect to the high mass loading, the measured SDC is relatively high for 1C, indicating, that no significant limitations occur during charge transfer at this rate.

The Kynar B electrode starts at the highest SDC with 149 mAh/g but ends with an SDC of 113 mAh/g after 1000 cycles, resulting in a loss of 36 mAh/g during cycling. With a higher porosity and lower mass loading than the Kynar A, the high SDC at the start of the measurement falls in line with the results of the previous rate capability tests. Nevertheless, the measured capacity fade of the Kynar B electrode is the highest of all electrodes.

The Kynar C and D start at an SDC of 143 mAh/g. The Kynar D has a slightly higher capacity loss, and the cells terminate prematurely after 925 and 981 cycles, with a terminal discharge capacity

of 113 mAh/g and 105 mAh/g, resulting in a loss of 30 mAh/g and 38 mAh/g, respectively. The Kynar C electrode terminates at 116 mAh/g, thus losing 27 mAh/g after 1000 cycles. It has a slightly higher porosity, but significantly higher mass loading compared to the Kynar D electrode. Therefore, its better cycling performance is surprising, indicating a slightly different degradation mechanism for the Kynar D electrodes.

Overall, the Kynar A electrode shows a significantly better cycle life despite the very high mass loading. With very similar morphologies between the Kynar A and B electrodes, these strong differences in cycle life are surprising. The Kynar B electrode shows a high capacity loss after 1000 cycles, even when compared to the Kynar C and D electrodes despite its significantly higher porosity.

Since the utilization of the different binders with better shear behavior allowed the production of more homogeneous and larger electrodes with the herein-used dry calendering method, electrodes in pouch cell formats were produced. For slightly better comparability, and due to the Kynar A not being able to be processed to a pouch cell format (very wavy electrodes), the remaining electrodes have been produced to have a similar thickness. The porosity of the electrodes cannot be controlled by the process itself since it is a function of the used binder. Therefore, the mass loading of the electrodes differs slightly. The electrode properties are given in Tab. 17 and the cycle life measurements are shown in Fig. 52.

Tab. 17: Properties of the electrodes produced with different binders used in the long-life cycling test of the pouch cells.

Electrode	Thickness in μm	Porosity	AM Mass loading in $\frac{mg}{cm^2}$
Kynar B	55.9 ± 6.2	0.34 ± 0.02	15.8 ± 0.7
Kynar C	50.1 ± 5.6	0.20 ± 0.02	17.0 ± 1.7
Kynar D	50.6 ± 2.2	0.22 ± 0.01	16.7 ± 0.7
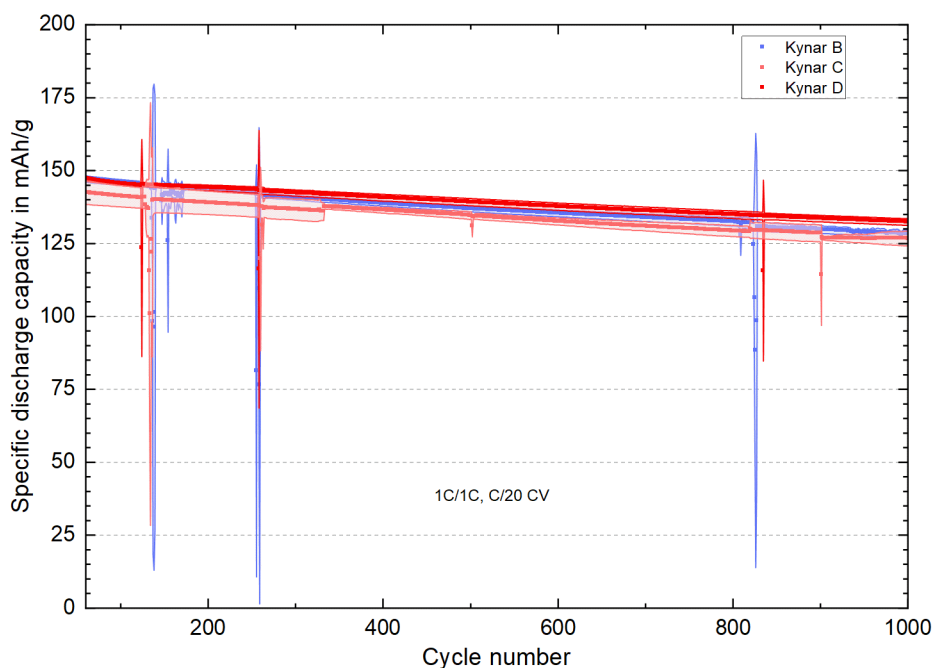
Fig. 52: Long life cycling test of the electrodes produced with different binders in pouch cell format. Symmetric cycling at 1C with a CV step at a cutoff current of C/20.

The electrode thickness and mass loading of the compared electrodes are fairly similar. The porosity and the binder properties are the major differences between these electrodes. The performance of all electrodes is very similar, thus the low porosity of the Kynar C and D electrodes seem not to impede the electrode capacity at a rate of 1C. The Kynar B and the Kynad D electrodes start with an initial SDC of 147 mAh/g, while the Kynar C electrode starts with 142 mAh/g. In terms of capacity loss during cycle life, the obtained results are similar to the coin cell cycle life measurements. The Kynar B electrode shows the highest capacity loss of 19 mAh/g compared to that of the Kynar C and D electrodes with a loss of 15 mAh/g. Although the trend in capacity loss is the same as for the coin cells, the differences between the electrodes are smaller than in coin cell measurements. Also, here, the Kynar C and D electrodes do show identical capacity fade after 1000 cycles in contrast to coin cell tests, where the Kynar C electrode retained a higher terminal SDC. Due to a higher electrode surface, pouch cell tests typically are more representative of the electrode performance and, thus should carry more weight compared to coin cell tests.

4.3.2 Discussion

The influence of the binder properties and its distribution already became evident during the analysis of the powder mixing homogeneity. This influence is not surprising when the viscoelastic properties of the polymeric binders are compared to the material properties of the other solid battery components, such as the NMC622, CB, and graphite. These strong differences in mechanical behavior make the direct comparison of shear behavior between the materials difficult but has been attempted in this chapter by the measurement of the powder mixture shear strength at room temperature and above the melting temperature of the binder in Fig. 40. At low normal loads the mixture at 200 °C has a significantly higher shear strength due to the dominance of the cohesive and adhesive forces in this low-pressure region. Electrode binders are optimized to have high adhesion, thus by adhering to the AM particles, as well as the shear cell walls, a very high shear strength of the powder bulk is achieved. The adhesive and cohesive forces do not increase once the powder bulk is consolidated and a maximum contact interface between the binder and solid particles is reached [95]. With further increasing normal loads, the friction forces become the dominant contributor to the shear strength of the powder. The shear strength of the mixture at 200 °C decreases for high normal loads until it reaches a similar value as the mixture measured at room temperature. Thus, the strong adhesive forces of the binder do not significantly impact the shear strength of the mixture at such high normal loads as 150 kPa.

Furthermore, considering the viscoelastic properties of the binder, the shear strength of the PVDF is not expected to change strongly with increasing pressure, especially, since the PVDF is processed above its melting temperature in a liquid state. Although some works show a pressure dependence of the polymer melt shear strength [120, 122], the effect of very large pressures such as 35 MPa leads to relatively small increases of polymer shear strength by factors of 2-5 [120]. On the other hand, powder shear strength increases linearly with increasing pressures, the friction coefficient being the ratio between the normal load and the shear strength of the sample. The comparison of the shear rate-dependent shear strength of the PVDF melt and the pressure-dependent shear strength of the NMC622 AM for a constant friction coefficient has been done in Fig. 41. This comparison shows that the shear strength of the solid sample exceeds the shear strength of the PVDF already at normal loads of 1.3 MPa for the presented materials. Since the normal load acting on the materials during compaction is in the range of 23 MPa, thus at significantly higher pressures, the PVDF shear strength is lower than that of the solids. Upon shear deformation, the PVDF is able to undergo plastic deformation more easily, therefore it acts as a lubricant.

On this basis, by the utilization of binders with different complex viscosities, the influence of PVDF shear strength on the powder processibility has been directly investigated. The analysis of the roll mill gap width in Fig. 43 can be directly correlated with the viscosity of the used binders. The mixture with the high viscosity binder (Kynar A) shows the strongest shear strength due to the gap opening at process parameters that are very shear-promoting. By gradually decreasing the speed difference between the two rolls, the mixture containing the Kynar B starts to open

the gap, then the low viscosity binders Kynar C and D. Therefore, the viscosity of the binder is directly linked to the shear strength of the battery mixture and the utilization of low viscosity binders increases the processibility window during calendering.

Apart from the viscosity, other binder properties influence the calendering process and the electrode morphology. Differences in the binder morphology are observed in the SEM analysis of the electrode cross sections in Fig. 44. The homopolymeric binders Kynar A and B result in electrodes, where the binder is present in the form of filaments that are stretched in one direction and connect several AM particles. These filaments have been observed also in chapter two, where the analysis of the additive distribution has been investigated. Such filaments are not detected in any electrodes made with the Kynar C and D binders. Additionally, after comparing the possibly achievable electrode thicknesses and porosities for each respective binder in Fig. 46, clear differences in electrode porosity can be observed. The homopolymeric Kynar A and B are limited to producing electrodes with a porosity of 28 % or higher where no AM particle breakage is observed, while the copolymeric Kynar C and D are only able to produce electrodes below 28 % porosity. This means, that the electrode structure caused by the filamentation of Kynar A and B has a higher porosity, but also has a higher mechanical strength since they resist further compaction. It is assumed, that the filaments in these electrodes are connecting and stabilizing the AM particles in a porous binder network, increasing the mechanical strength of the electrode while also ensuring a high porosity. The crucial binder property enabling filament formation is expected to be the peculiar molecular weight distribution of the Kynar A and B. They not only have a high mean molecular weight, but they also have a bimodal molecular weight distribution, with a low mass percentage having an enormously high molecular weight, that can hardly be determined by measurements. These super high chain length molecules can undergo elastic shear deformation and build the basis of the observed filaments.

The Kynar C and D have a monomodal molecular weight distribution, that is lower in molecular weight than the Kynar A and B, causing them to have lower melt viscosities but also rendering them unlikely to form filaments. Thus, the copolymers are more easily plastically deformed under the shearing process in the calender gap and result in thinner electrodes with more smooth surfaces as can be seen in the surface analysis in Fig. 45. On the other hand, the electrodes have a lower porosity and upon high compaction particle breakage can occur.

With the differences in electrode morphology caused by the binder properties, a separate comparison of the binder influence on the electrochemical performance of the cells is rather difficult. Nonetheless, the analysis of the electrochemical performance of the cells shows the indirect consequences of the binder properties caused by differences in electrode thickness, mass loading, and porosity. Rate capability tests of electrodes with quite high mass loadings of above 20 mg/cm^2 in Fig. 47. Show, that at very low charge and discharge rates the specific discharge capacity (SDC) of the cells is comparable and close to the theoretically achievable SDC of the utilized NMC622. With increasing rates, low porosity, and high mass loading both reduce the capacity retention of the cells, due to increasing limitations in ion diffusion to and from reaction sites of the active materials, as can be seen in the evolution of the overpotential in Fig. 49. A

combination of both, low mass loading and high porosity are beneficial for high charge and discharge rates. Nevertheless, for applications running at very low rates, the use of dense and thick electrodes is a good possibility to increase the energy density of the battery.

The negative effect of high mass loading on the capacity retention at high charge and discharge rates seems to be more influential than low porosities as the analysis in Fig. 48 and Fig. 50 indicate. Cells with rather similar porosities but different mass loadings show a strong reduction in capacity retention with increasing mass loading, while cells with similar mass loading but different porosities differ only slightly. This is mainly caused by the relative changes to the investigated parameters. Doubling the mass loading of an electrode can easily be done and investigated, while doubling the porosity of the electrode is not as easy for slurry-based processes, nonetheless for dry manufacturing where electrode structure is strongly influenced by binder properties. Thus, the differences investigated here are not equal in terms of changes induced by ion diffusion and permeability. Nevertheless, the results show, that mass loading is the more easily controlled parameter to manage the rate capability of the electrode and that small changes in electrode porosity easily become redundant compared to big changes in mass loading. Optimization of both parameters remains necessary, but it is suggested, to begin with the mass loading according to the specific needs in terms of the energy density of the desired electrode.

Long-life cycling tests in Fig. 51 at an intermediate C-rate of 1C show small differences in capacity retention for the electrodes produced with different binders. At this charge and discharge rate, ion diffusion limitations are small since the SDC of all measured electrodes is in the range of approx. 150 mAh/g, thus only slightly below the theoretical SDC of 175 mAh/g of the NMC622. The Kynar A electrode shows the best capacity retention after 1000 cycles. Also, the mass loading of this electrode is significantly higher than for the other electrodes, and still, no ion diffusion limitations can be observed. The Kynar B has the highest SDC fade of the measured electrodes, which is surprising when the similar electrode morphology to the Kynar A is considered. All previously conducted analysis of the electrode structure have revealed no differences between the Kynar A and B electrodes, even the binder properties are expected to be identical except for the slightly higher molecular weight of the Kynar A. Therefore, the observed difference in cycle life behavior between these two electrodes can not be traced back to a specific cause. It is assumed, that limited reproducibility of the dry calendering process led to inhomogeneities in the produced electrodes, which can introduce small differences to the electrochemical performance in the scale it is observed here. Additionally, Fig. 51 shows the cycle life performance of coin cells, which as well are more prone to inhomogeneities in the utilized electrodes.

To have more reliable data for the comparison of the cycle life behavior of the electrodes, pouch cells were analyzed with the same test procedure in Fig. 52. The Kynar A electrode could not be included in this comparison since the dry manufacturing of electrodes with sufficient size was not possible due to the low processability of the Kynar A containing powder. The electrodes made with the binder that have lower viscosities have similar thickness and quite similar mass loading. The porosity is significantly different since they are dominantly influenced by the binder

properties rather than the utilized process parameters. All electrodes have very similar SDC from start to end of the cycle life test. The Kynar D electrode slightly outperforms the other electrodes but has the same absolute capacity fade as the Kynar C after 1000 cycles, with a loss of 15 mAh/g. The results for both cycle life tests, with coin and pouch cells, indicate that the discharge capacity fade is quite independent of the binder properties and even independent of the electrode properties indirectly influenced by the binder such as porosity and binder filamentation.

Overall, the lubricating effect of the binder could be confirmed and correlated to its melt viscosity, where lower viscosities lead to improved processability of the powder blend. The ability to form filaments was attributed to the existence of very high molecular weight polymer chains. Thus, filamentation is not necessarily linked to high melt viscosities, but indirectly since high molecular weight polymer chains induce higher viscosities. The filaments form a network in the electrode structure, incorporating the CB and connecting the AM particles, increasing the mechanical strength, but also the material resistance towards deformation and compaction. This results in electrodes with significantly higher porosities compared to the electrodes produced with binder unable to form filaments. By influencing the electrode morphology, the electrochemical performance of the produced electrodes is indirectly influenced. These observations show the significance of polymer selection when used in dry electrode manufacturing by direct powder compaction. Depending on the desired electrode properties such as rate performance, mass loading, or electrode thickness, the correct choice of binder is necessary.

5 Conclusion

The thorough investigation of process and material parameters in direct powder calendering for dry LIB electrode production has revealed a strong interrelation between the parameters that influence the granular shear mechanics during compaction in the calender roll gap. The shear displacement of the particles determines the processibility of the powder and the resulting electrode morphology. With the promotion of granular shear, strong compaction of the powder can be avoided, reducing the risk of AM particle breakage. Additionally, a more versatile electrode formation is possible by the reduction of electrode thickness and increase of electrode porosity. With increasing shear displacement of the particles, they can be more easily formed to the desired electrode morphology.

Key process parameters are the temperature, which is responsible for the softening of the binder, and the speed difference between the rolls, which introduces a shear profile to the granular material. High roll pressures increase the normal load onto the material during processing, thus shearing is impeded. Nevertheless, a minimum roll pressure is necessary to compact the material sufficiently to establish good contacting between the electrode material species, ensuring electric conductivity and mechanical strength through the binder.

As a key material parameter, the internal friction coefficient of the powder blend bulk has been identified. The shear displacement of granular media under load is facilitated by low internal friction, thus the processibility of such powders is improved. This allows a more versatile adjustment of the process parameters, resulting in a wider range of possible electrode morphologies and higher reproducibility of electrode properties. The internal friction of granular media is very complex as the evaluation of the presented literature shows. Many material and particle properties influence the friction coefficient of a material. Additionally, in LIB cathode production a multitude of different materials can be used, adding to the complexity of the system. As a general rule, low surface roughness and round-shaped particles have lower friction coefficients. Furthermore, the addition of angular particles can improve steady-state shear deformation by introducing a material that can rotate rather than shear. Also, solid lubricants like graphite, which can additionally delaminate can promote and stabilize the shear deformation of the powder bulk.

The polymeric binder has turned out to not only be necessary due to its role as a binding additive, but it also promotes the shear deformation of the powder blend by its ability to easily undergo plastic deformation under shear. Compared to the friction of the solid components under normal load, the shear strength of the binder is significantly lower, rendering the binder a lubricant in this specific application. Low melt viscosities correlate with improved powder processibility and more versatile electrode production. Other than that, binder molecular length seems to determine whether binder filamentation takes place upon shear deformation. These filaments form a special binder network improving the mechanical strength of the powder blend and also of the electrode. On one hand, this impedes the shear deformation of the powder

blend, making processing more difficult. On the other hand, it enables the production of electrodes with a higher porosity, capable of higher rate performances during cell cycling.

Using these insights, the direct powder calendering process has been further developed throughout this work. Electrode manufacturing has been improved to the point, that a versatile production of electrodes is possible for different materials. The resulting electrode morphology has a wide range from thin (<50 µm) to very thick (>500 µm) electrodes with porosities typical for industrial electrodes (20-35 %). The electrochemical performance of the produced electrodes is good and with respect to the electrode morphology, they can be competitive with slurry-based electrodes.

Nevertheless, the main merit of this work lies in revealing the importance of the shear deformation of the powder blend during calendering and the interrelation of the process and material parameters that influence the shear mechanics of the process. This understanding allows the adaptation of the process according to the desired electrode properties or the used materials. A toolbox has been put together to influence powder processibility and manage both, electrode morphology and its resulting electrochemical performance.

Appendix

Supplementary Results
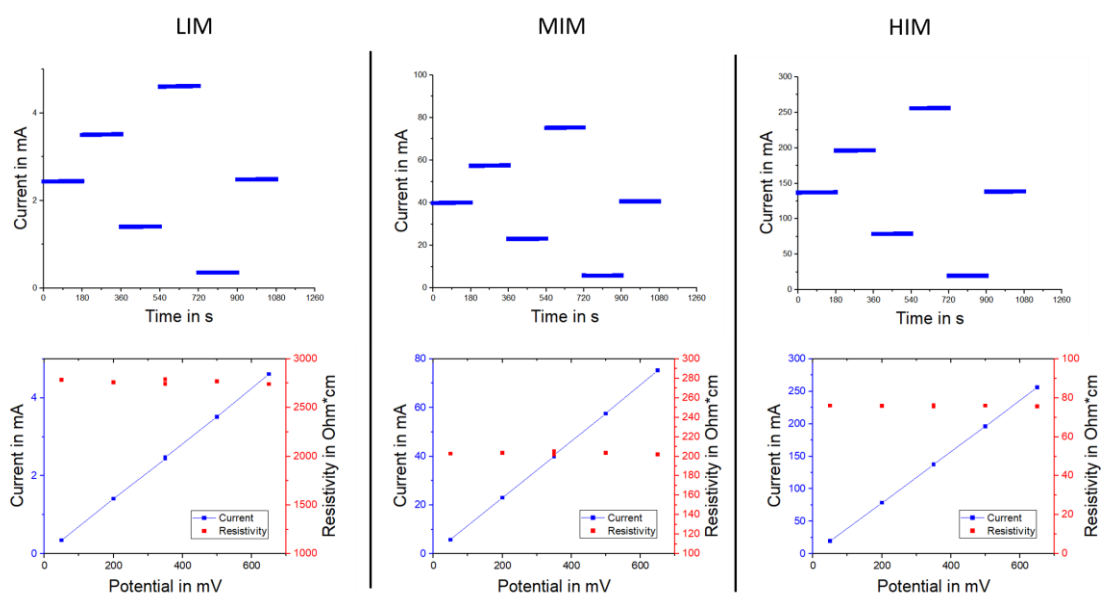
Fig. A. 1: DC polarization measurement of the powder blends made by different mixing intensities. Current shows linear response to potential changes and no lags in the responses are noticed.

The measured current shows no signs of time dependence upon changes in the applied potential. Also, the relationship between current and potential are linear. No signs of polarization have been found for the powder bulk resistivity measurements.
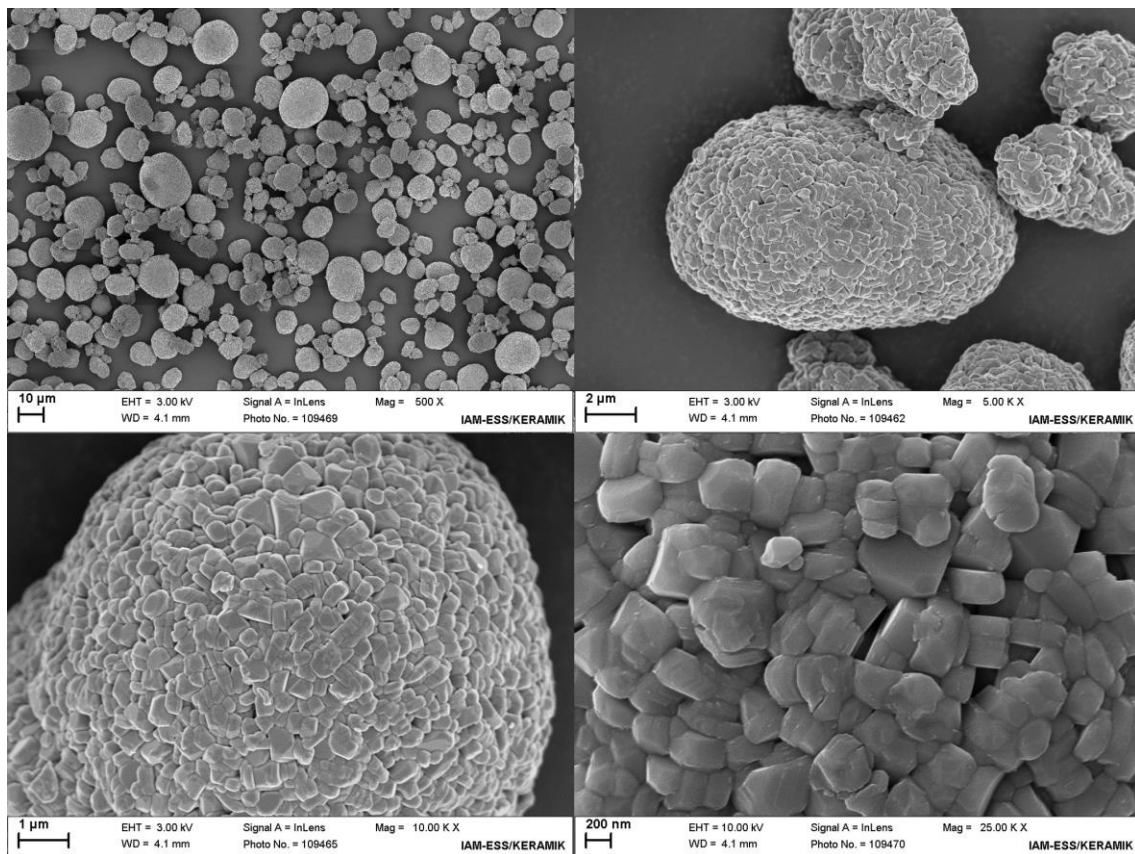
Fig. A. 2: Pristine NMC622 particles at different magnifications

The NMC622 active material consists of roughly spherical particles with a diameter in the range of 5-20 µm. The particles consist of many small primary crystals, which are sintered together.
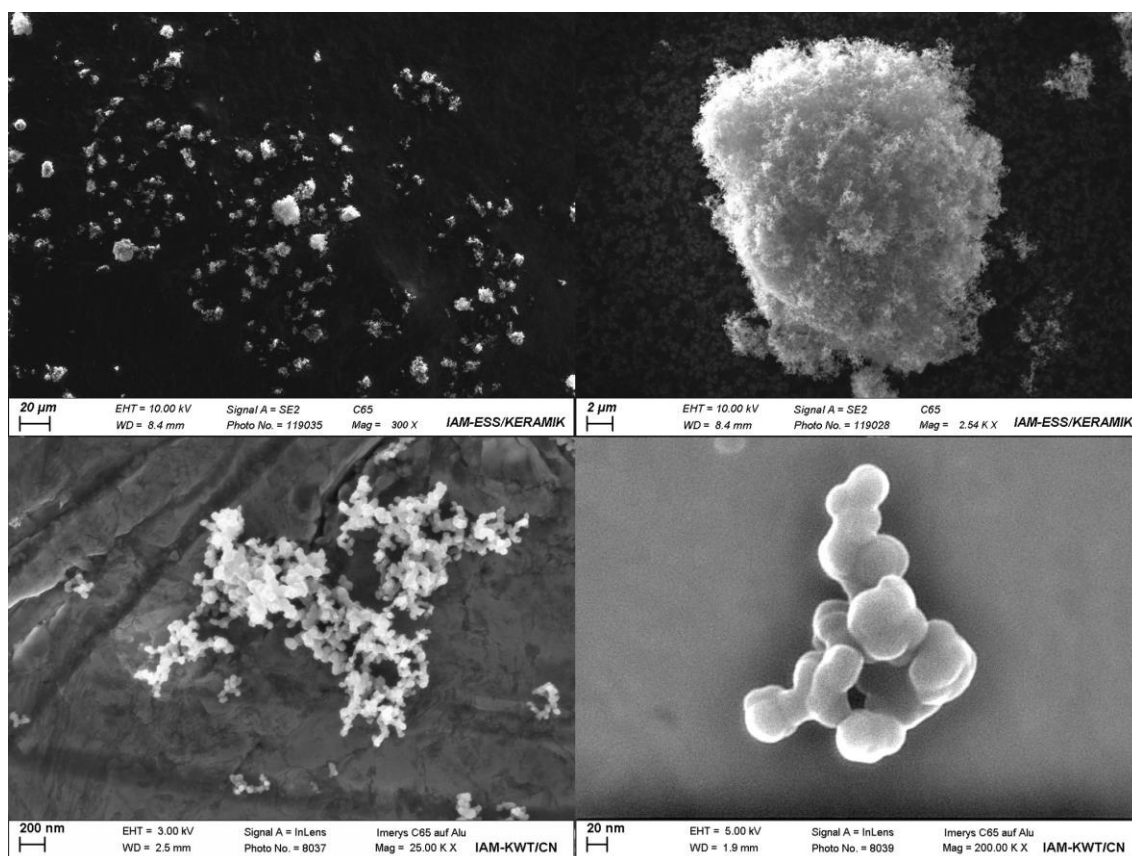
Fig. A. 3: CB (C65) particles at different magnifications. Agglomerate particles of various sizes formed by smaller aggregates. Primary particles are very small and irregularly structured.

The C65 is a powder consisting of agglomerates with a wide range of sizes and shapes. These agglomerates consist of smaller aggregate particles with a very fine and also irregular structure. The agglomerates can be deagglomerated to their comprising aggregates with the introduction of sufficiently high shear and/or impact forces.
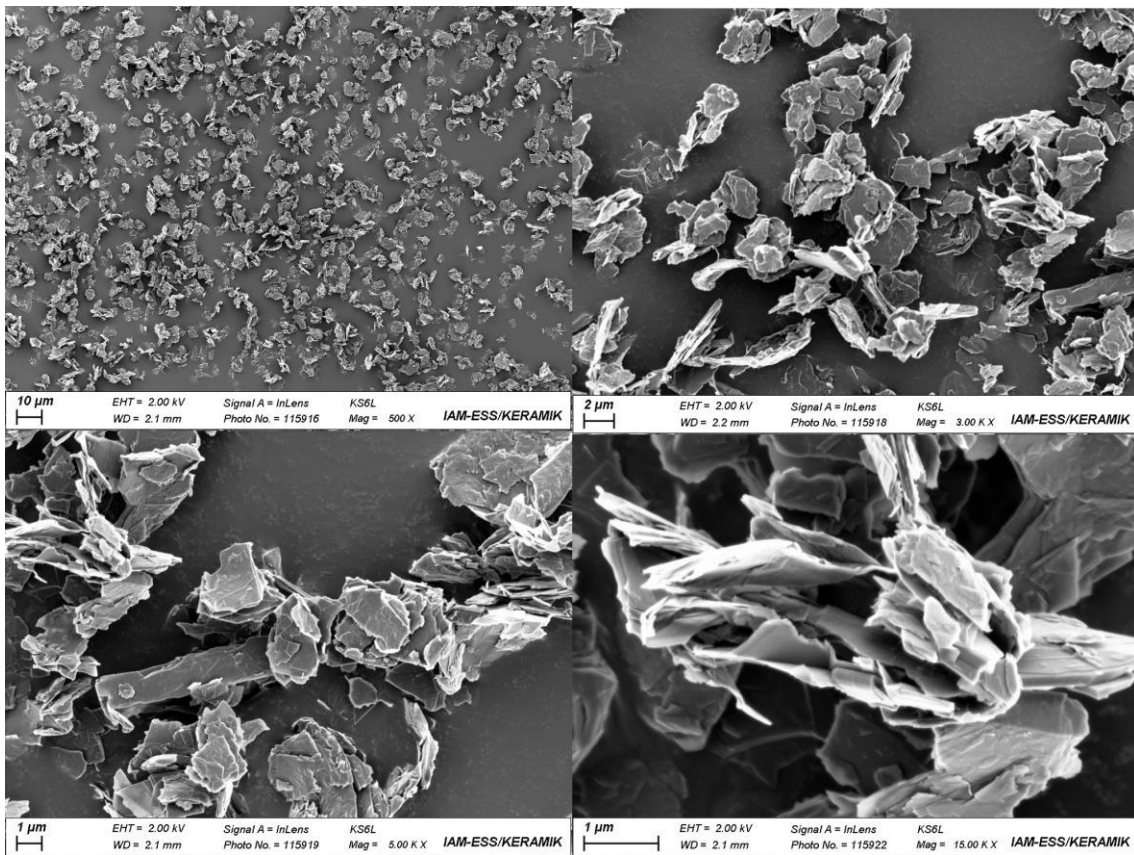
Fig. A. 4: Graphite conductive and lubricating additive (KS6L). Plate-like structured particles with a size of approx. 6 μm.

The KS6L graphite has a plate-like structure. Irregularities in the arrangement of its constituting graphene layers cause the particles to have a low shear strength. Shear deformation at their junctions is easily possible, rendering this material useful as a solid lubricant.
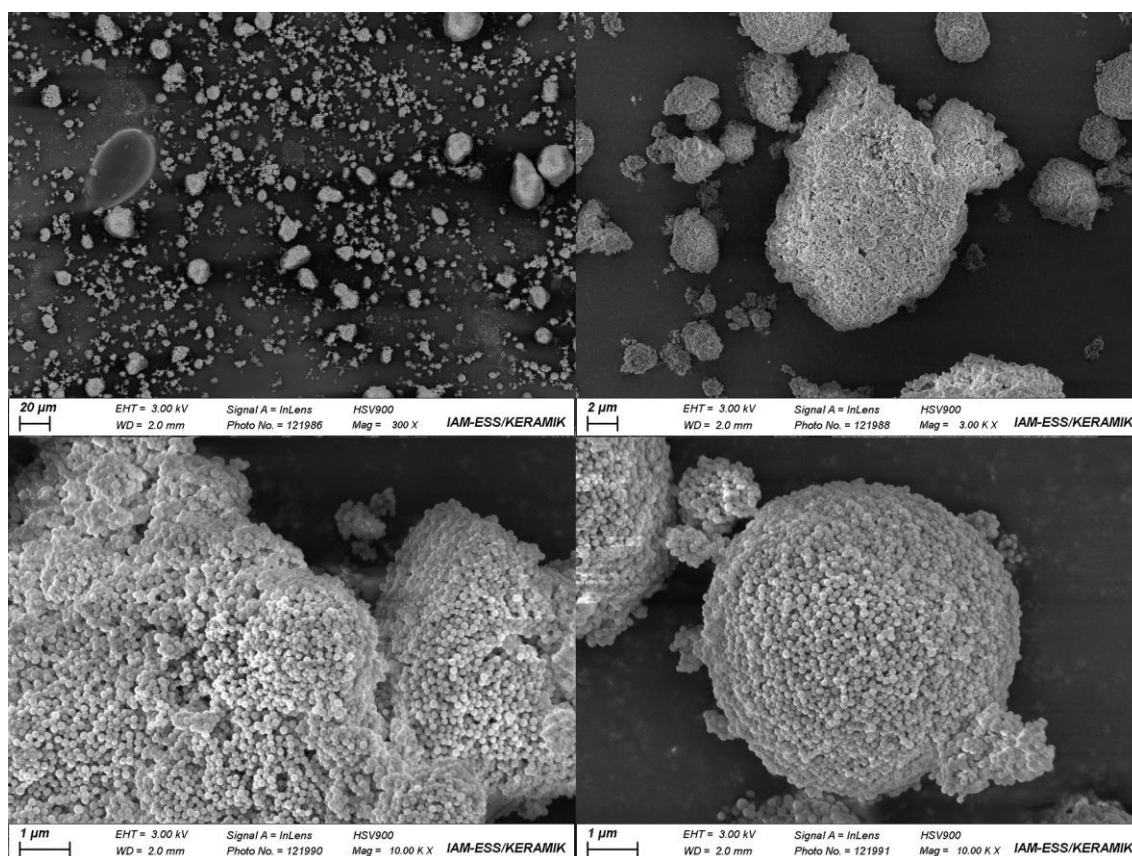
Fig. A. 5: PVDF (Kynar A) particles at different magnifications. Agglomerates of various sizes are formed by spherical primary particles of approx. 200 nm diameter.

All Kynar PVDFs used in this work show the same particle morphology. The particles are agglomerates of small spherical primary particles with a diameter of approx. 200 nm. The shape and size of the Agglomerate particles can vary. With the input of sufficient shear and/or impact forces, the agglomerated can be deagglomerated. Although, the material is visco-elastic. High temperatures or low shear rates upon deformation can lead to viscous deformation or even melting.
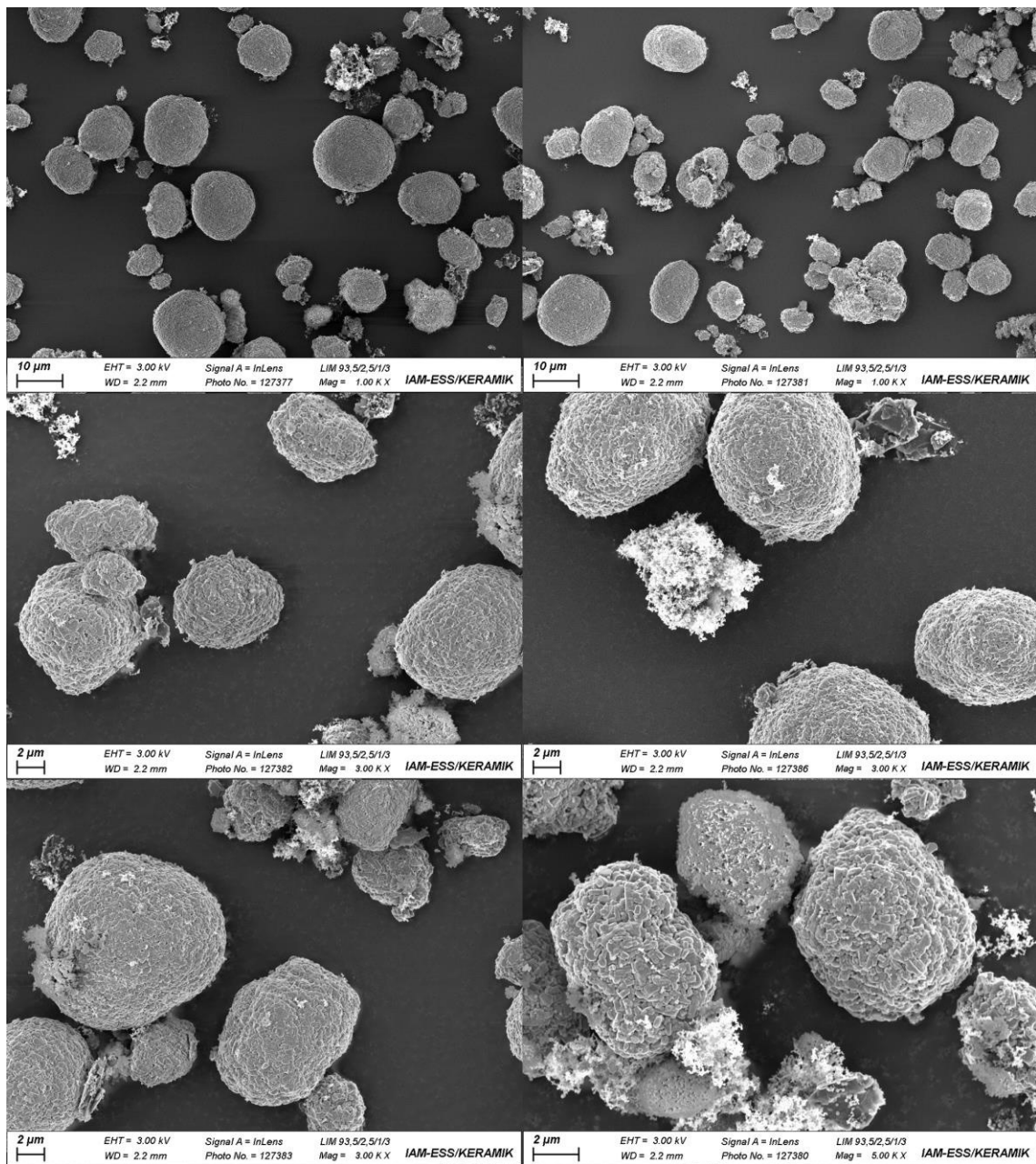
Fig. A. 6: SEM micrographs of the LIM at different magnifications. Materials are homogenized but not deagglomerated.

A mixture of NMC622, Kynar A, C65, and KS6L was produced at low mixing intensities. At low magnifications, a homogeneous distribution of the respective agglomerate particles throughout the bulk of the mixture can be observed. But no deagglomeration of the additives is observed. Thus, at high magnifications, the pristine particles can be seen, leading to a very inhomogeneous distribution of the components at microscopic scale.
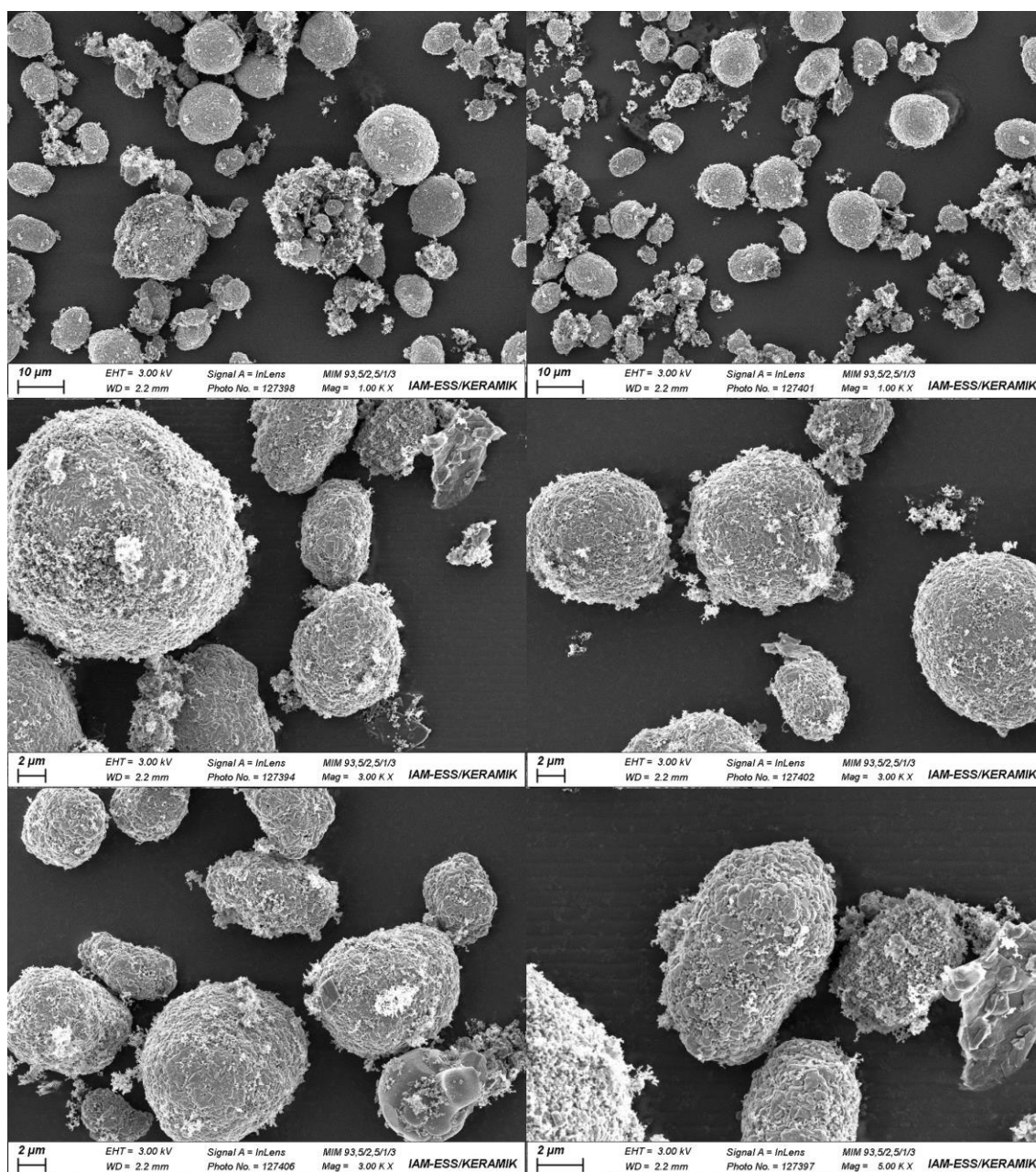
Fig. A. 7: SEM micrographs of the MIM at different magnifications. Partial deagglomeration of CB and PVDF additives. Some reagglomeration on few AM particles.

A mixture of NMC622, Kynar A, C65, and KS6L was produced at medium mixing intensities. At low magnifications, the distribution of the respective particles is homogeneous through the bulk of the powder. At high magnifications small fractions and aggregates of the additives can be identified, but also large additive agglomerate particles can be found. This indicates, that a part of the additive particles has been deagglomerated. The deagglomerated fraction is found to be partly redistributed on some of the AM particles. Still, many AM particles are devoid of additives on their surface.
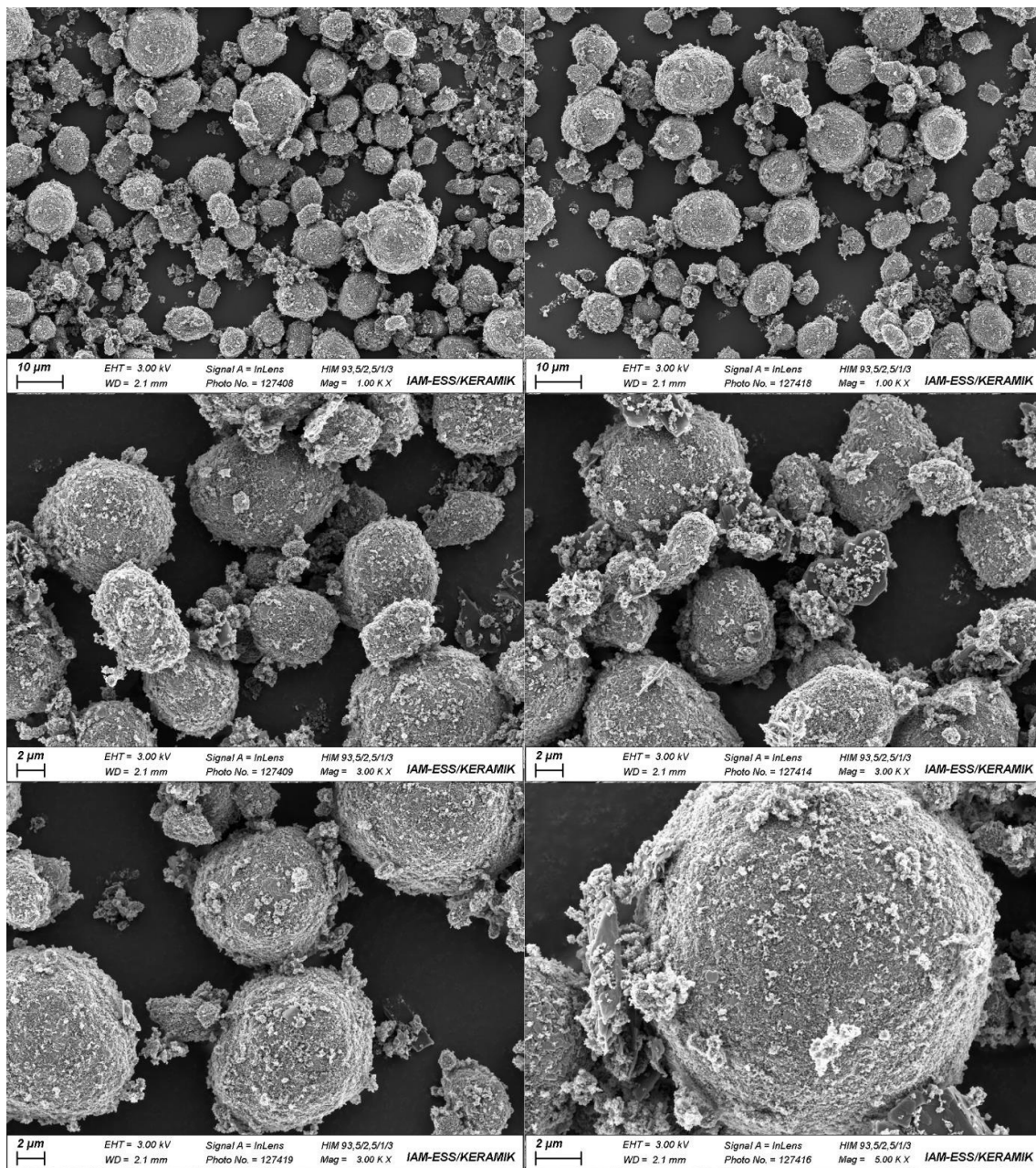
Fig. A. 8: SEM micrographs of the HIM at different magnifications. Complete deagglomeration of CB and PVDF additives and redistribution on AM surface. A small degree of reagglomeration.

A mixture of NMC622, Kynar A, C65 and KS6L produced at high mixing intensities. The Additive agglomerate particles have been deagglomerated thoroughly. Some aggregates and primary particles have reformed into small agglomerates consisting of a mixture of the material species. This powder mixture thus shows a homogeneous distribution at low magnifications, as well as at high magnifications, since the additives cover the surface of most AM particles.

List of Equations

List of Physical Operators

α	Angularity
α_F	Feed zone angle
α_N	Nip zone angle
γ_0	Strain amplitude
δ	Phase shift
ε_q	Horizontal strain
η	Dynamic viscosity
μ	Friction coefficient
μ_k	Kinetic friction coefficient
μ_s	Static friction coefficient
μ^*	Macroscopic friction coefficient
$\sigma(t)$	Stress (time dependent)
σ_0	Stress amplitude
τ	Shear stress
ω	Angular frueqency
F_N	Normal force
F_S	Shear force
G	Shear modulus
G'	Storage modulus
G''	Loss modulus
h_E	Final gap width (distance)
$h_{Nip1,2}$	Gap width at nip zone angle α_N for different roll diameters
P	Pressure
P_α	Pressure perpendicular to roll surface

Q	Resistance force
$\dfrac{q}{p}$	Also μ_s; static friction coefficient
s	Length of volume element in the nip zone
t	Time
U	Velocity
$u_{i,x,y,z}$	Velocity in i/x/y/z direction
$u_{1,2}$	Circumferential velocity of the roll surface of the respective rolls

List of Abbreviations

AM   Active material

PVDF   Polynivylidene fluoride

CB   Carbon black

GHG   Greenhouse gas

LIB   Lithium-ion battery

CBD   Carbon binder domain

NMP   N-Methyl-2-pyrrolidone

ESD   Electrostatic spray deposition

SSB   Solid-state battery

PTFE   Polytetrafluoroethylene

DIFC   Dynamica internal friction coefficient

SIFC   Static internal friction coefficient

LIM   Low-intensity mixture

MIM   Medium-intensity mixture

HIM   High-intensity mixture

CV   Constant voltage

SEM   Scanning electron microscopy

EDS   Energy-dispersive X-ray spectroscopy

SDC   Specific discharge capacity

Sources

1. IEA (2018), *Global EV Outlook 2018*, IEA, Paris, https://www.iea.org/reports/global-ev-outlook-2018, License: CC BY 4.0.
2. European Commion, *EU transport in figures : statistical pocketbook 2021*. 2021: Publications Office, https://transport.ec.europa.eu/media-corner/publications/statistical-pocketbook-2021_en
3. IEA (2022), *Global Supply Chains of EV Batteries*, IEA, Paris, https://www.iea.org/reports/global-supply-chains-of-ev-batteries, License: CC BY 4.0.
4. Schmuch, R., Wagner, R., Hörpel, G., Placke, T., Winter, M., *Performance and cost of materials for lithium-based rechargeable automotive batteries.* Nature Energy, 2018. **3**(4), p. 267-278.
5. Armand, M., Axmann, P., Bresser, D., Copley, M., Edström, K., Ekberg, C., Guyomard, D., Lestriez, B., Novák, P., Petranik, M., Porcher, W., Trabesinger, S., Wohlfahrt-Mehrens, M., Zhang, H., *Lithium-ion batteries -Current state of the art and anticipated developments.* Journal of Power Sources, 2020. **479**, 228708.
6. Bryntesen, S. N., Strømman, A. H., Tolstorebrov, I., Shearing, P. R., Lamb, J. J., Stokke Burheim, O., *Opportunities for the State-of-the-Art Production of LIB Electrodes—A Review.* Energies, 2021. **14**(5), p. 1406.
7. Nelson, P. A., Ahmed, S., Gallagher, K. G., Dees, D. W*., Modeling the Performance and Cost of Lithium-Ion Batteries for Electric-Drive Vehicles, Third Edition*. 2019: United States.
8. Wood, D. L., Quass, J. D., Li, J., Ahmed, S., Ventola, D., Daniel, C., *Technical and economic analysis of solvent-based lithium-ion electrode drying with water and NMP.* Drying Technology, 2018. **36**(2), p. 234-244.
9. Degen, F., Krätzig, O., *Future in Battery Production: An Extensive Benchmarking of Novel Production Technologies as Guidance for Decision Making in Engineering.* IEEE Transactions on Engineering Management, 2022, p. 1-19.
10. Al-Shroofy, M., Zhang, Q., Xu, J., Chen, T., Kaur, A. P., Cheng, Y.-T., *Solvent-free dry powder coating process for low-cost manufacturing of LiNi$_{1/3}$Mn$_{1/3}$Co$_{1/3}$O$_2$ cathodes in lithium-ion batteries.* Journal of Power Sources, 2017. **352**, p. 187.
11. Zhu, C., Fu, Y., Yu, Y., *Designed Nanoarchitectures by Electrostatic Spray Deposition for Energy Storage.* Advanced Materials, 2019. **31**(1), 1803408.
12. Schälicke, G., Landwehr, I., Dinter, A., Pettinger, K.-H., Haselrieder, W., Kwade, A., *Solvent-Free Manufacturing of Electrodes for Lithium-Ion Batteries via Electrostatic Coating.* Energy Technology, 2020. **8**(2), 1900309.
13. Ludwig, B., Liu, J., Chen, I. M., Liu, Y., Shou, W., Wang, Y., Pan, H., *Understanding Interfacial-Energy-Driven Dry Powder Mixing for Solvent-Free Additive Manufacturing of Li-Ion Battery Electrodes.* Advanced Materials Interfaces, 2017. **4**(21), 1700570.
14. Liu, J., Ludwig, B., Liu, Y., Zheng, Z., Wang, F., Tang, M., Wang, J., Wang, J., Pan, H., Wang, Y., *Scalable Dry Printing Manufacturing to Enable Long-Life and High Energy Lithium-Ion Batteries.* Advanced Materials Technologies, 2017. **2**(10), 1700106.
15. Hippauf, F., Schumm, B., Doerfler, S., Althues, H., Fujiki, S., Shiratsuchi, T., Tsujimura, T., Aihara, Y., Kaskel, S., *Overcoming binder limitations of sheet-type solid-state cathodes using a solvent-free dry-film approach.* Energy Storage Materials, 2019. **21**, p. 390-398.
16. Kim, G.-T., Appetecchi, G. B., Alessandrini, F., Passerini, S., *Solvent-free, PYR1ATFSI ionic liquid-based ternary polymer electrolyte systems: I. Electrochemical characterization.* Journal of Power Sources, 2007. **171**(2), p. 861-869.

17. Appetecchi, G. B., Croce, F., Hassoun, J., Scrosati, B., Salomon, M., Cassel, F., *Hot-pressed, dry, composite, PEO-based electrolyte membranes: I. Ionic conductivity characterization.* Journal of Power Sources, 2003. **114**(1), p. 105-112.

18. Verma, P., Hippchen, S., Netz, A., *Verfahren zur Herstellung einer Elektrode eines Lithiumi-onenakkumulators*, 2017, DE 10 2015 214 577 A1, DPMA.

19. Tschöcke, S., Althues, H., Schumm, B., Kaskel, S., Schult, C., Fritsche, D., Schönherr, K., *Verfahren zum Herstellen eines Trockenfilms sowie Trockenfilm und mit dem Trockenfilm beschichtetes Substrat*, 2018, DE 10 2017 208 220 A1, DPMA.

20. Murray, V., Hall, D., Dahn, J., *A Guide to Full Coin Cell Making for Academic Researchers.* Journal of The Electrochemical Society, 2019. **166**, p. A329-A333.

21. Yoo, S., Hong, C., Chong, K. T., Seul, N. *Analysis of Pouch Performance to Ensure Impact Safety of Lithium-Ion Battery*. Energies, 2019. **12**(15), p. 2865.

22. Birke, K. P., Schweitzer, D. N., *Fundamental Aspects of Achievable Energy Densities in Electrochemical Cells*, in *Modern Battery Engineering*. 2018, p. 1-30.

23. Hambitzer, G., Pinkwart, K., Ripp, C., Schiller, C., *Thermodynamics and Mechanistics*, in *Handbook of Battery Materials*, 1998, p. 1-17.

24. Ghiji, M., Novozhilov, V., Moinuddin, K., Joseph, P., Burch, I., Suendermann, B., Gamble, G., *A Review of Lithium-Ion Battery Fire Suppression,* Energies, 2020. **13**, p. 5117.

25. Kraytsberg, A., Ein-Eli, Y., *Conveying Advanced Li-ion Battery Materials into Practice The Impact of Electrode Slurry Preparation Skills,* Advanced Energy Materials, 2016. **6**(21), p. 1600655.

26. Liu, G., Zheng, H., Song, X., Battaglia, V. S., *Particles and Polymer Binder Interaction: A Controlling Factor in Lithium-Ion Electrode Performance,* Journal of The Electrochemical Society, 2012. **159**(3), p. A214-A221.

27. Hawley, W. B., Li, J., *Electrode manufacturing for lithium-ion batteries—Analysis of current and next generation processing.* Journal of Energy Storage, 2019. **25**, 100862.

28. Schmitt, M., Baunach, M., Wengeler, L., Peters, K., Junges, P., Scharfer, P., Schabel, W., *Slot-die processing of lithium-ion battery electrodes—Coating window characterization,* Chemical Engineering and Processing: Process Intensification, 2013. **68**, p. 32-37.

29. Jaiser, S., Funk, L., Baunach, M., Scharfer, P., Schabel, W., *Experimental investigation into battery electrode surfaces: The distribution of liquid at the surface and the emptying of pores during drying,* Journal of Colloid and Interface Science, 2017, **494**, p. 22-31.

30. Shkrob, I. A., Gilbert, J. A., Phillips, P. J., Klie, R., Haasch, R. T., Bareno, J., Abraham, D. P., *Chemical weathering of layered Ni-rich oxide electrode materials: Evidence for cation exchange, J. Electrochem. Soc.,* 2017. **164** A1489.

31. Zhang, X., Jiang, W. J., Zhu, X. P., Mauger, A., Qilu, Julien, C. M., *Aging of LiNi1/3Mn1/3Co1/3O2 cathode material upon exposure to H2O,* Journal of Power Sources, 2011. **196**(11), p. 5102-5108.

32. Thomitzek, M., von Drachenfels, N., Cerdas, F., Herrmann, C., Thiede, S., *Simulation-based assessment of the energy demand in battery cell manufacturing,* Procedia CIRP, 2019, **80**, p. 126-131.

33. Yuan, C., Deng, Y., Li, T., Yang, F., *Manufacturing energy analysis of lithium ion battery pack for electric vehicles,* CIRP Annals, 2017. **66**(1), p. 53-56.

34. Ludwig, B., Zheng, Z., Shou, W., Wang, Y., Pan, H., *Solvent-Free Manufacturing of Electrodes for Lithium-ion Batteries,* Scientific Reports, 2016. **6**(1), 23150.

35. Verdier, N., Foran, G., Lepage, D., Prébé, A., Aymé-Perrot, D., Dollé, M., *Challenges in Solvent-Free Methods for Manufacturing Electrodes and Electrolytes for Lithium-Based Batteries* Polymers, 2021. **13**, p. 323.

36. Wiegmann, E., Kwade, A., Haselrieder, W., *Solvent Reduced Extrusion-Based Anode Production Process Integrating Granulate Coating, Drying, and Calendering,* Energy Technology, 2022. **10**(6), 2200020.

37. Thiry, J., Krier, F., Evrard, B., *A review of pharmaceutical extrusion: Critical process parameters and scaling-up.* International Journal of Pharmaceutics, 2015. **479**(1): p. 227-240.

38. Haarmann, M., Grießl, D., Kwade, A., *Continuous Processing of Cathode Slurry by Extrusion for Lithium-Ion Batteries,* Energy Technology, 2021. **9**(10), 2100250.

39. Dreger, H., Bockholt, H., Haselrieder, W., Kwade, A., *Discontinuous and Continuous Processing of Low-Solvent Battery Slurries for Lithium Nickel Cobalt Manganese Oxide Electrodes,* Journal of Electronic Materials, 2015. **44**(11), p. 4434-4443.

40. Haarmann, M., Haselrieder, W., Kwade, A., *Extrusion-Based Processing of Cathodes: Influence of Solid Content on Suspension and Electrode Properties,* Energy Technology, 2020. **8**(2), 1801169.

41. Gray, F. M., Vincent, C. A., Kent, M., *Dielectric studies of poly(ethylene oxide)-based polymer electrolytes using time-domain spectroscopy,* Solid State Ionics, 1988. **28-30**: p. 936-940.

42. Brochu, F., Duval, M., *Additives for extruding polymer electrolytes,* 1998, US005622792A, USPTO.

43. Duval, M., *Process of coating by melt extrusion a solid polymer electrolyte on positive electrode of lithium battery*, 1994, US005348824A, USPTO.

44. Bauer, H., Reinsch, B., Weydanz, W., Glanz, L., Wurm, C., *Elektrodenherstellungsverfahren mittels Binderfibrillierung mit partikulärem Fribrillierungshilfsmittel*, DE 10 2017 213 388 A1, DPMA.

45. Steinhoff, B. D., Dong, J., Mashtalir, O., Amin-Sanayei, R., Hong, K., Li, J., *High Throughput Solvent-Free Manufacturing of Battery Electrodes.* ECS Meeting Abstracts, 2022. **MA2022-02**(6), p. 633.

46. El Khakani, S., Verdier, N., Lepage, D., Prébé, A., Aymé-Perrot, D., Rochefort, D., Dollé, M., *Melt-processed electrode for lithium ion battery.* Journal of Power Sources, 2020. **454**, 227884.

47. MacFarlane, D. R., Zhou, F., Forsyth, M., *Ion conductivity in amorphous polymer/salt mixtures.* Solid State Ionics, 1998. **113-115**, p. 193-197.

48. Forsyth, M., Jiazeng, S., MacFarlane, D. R., *Novel high salt content polymer electrolytes based on high Tg polymers,* Electrochimica Acta, 2000. **45**(8), p. 1249-1254.

49. German, R. M., *Chapter Ten - Sintering With External Pressure*, in *Sintering: from Empirical Observations to Scientific Principles*, R.M. German, 2014, Butterworth-Heinemann: Boston, p. 305-354.

50. de la Torre-Gamarra, C., Sotomayor, M. E., Sanchez, J.-Y., Levenfeld, B., Várez, A., Laïk, B., Pereira-Ramos, J.-P., *High mass loading additive-free LiFePO4 cathodes with 500 μm thickness for high areal capacity Li-ion batteries* Journal of Power Sources, 2020. **458**, 228033.

51. Lai, W., Erdonmez, C. K., Marinis, T. F., Bjune, C. K., Dudney, N. J., Xu, F., Wartena, R., Chiang, Y.-M., *Ultrahigh-Energy-Density Microbatteries Enabled by New Electrode Architecture and Micropackaging Design,* Advanced Materials, 2010. **22**(20), p. E139-E144.

52. Astafyeva, K., Dousset, C., Bureau, Y., Stalmach, S.-L., Dufour, B., *High Energy Li-Ion Electrodes Prepared via a Solventless Melt Process,* Batteries & Supercaps, 2020. **3**(4), p. 341-343.

53. Mitchell, P., Xi, X., Zhong, L., *Method of Manufacturing an Electrode Product*, 2011, US007883553B2, USPTO.

54. Daniels, J., Daniels, C., *The Origin of the Sugarcane Roller Mill,* Technology and Culture, 1988. **29**(3), p. 493-535.

55. Schönert, K., Ohe, W. v. D., Rumpf, H., *Technische Feinzerkleinerung mit Einzelkornbeanspruchung zwischen zwei Flächen,* Chemie Ingenieur Technik, 1965. **37**(3): p. 259-264.

56. Senthil Kumar, R., Sundaresan, S., *6 - Mechanical finishing techniques for technical textiles*, in *Advances in the Dyeing and Finishing of Technical Textiles*, Gulrajani M. L., 2013, Woodhead Publishing. p. 135-153.

57. Chaussy, D., Guerin, D., *Calendering of Papers and Boards: Processes and Basic Mechanisms,* in *Lignocellulosic Fibers and Wood Handbook: Renewable Materials for Today's Environment, Belgacem, N., Pizzi, A.,* 2016, Scrivener Publishing, p. 493-529.

58. Vinogradov, G. A., Katashinskii, V. P., *The angle parameters of the metal-powder rolling process,* Soviet Powder Metallurgy and Metal Ceramics, 1965, **4**(9), p. 722-726.

59. Fairbairn, R. A., *Calendered Thermoplastics*, in *Plastics: Surface and Finish*, Whelan A., et al., 1995, The Royal Society of Chemistry.

60. Ceccato, C., Brandberg, A., Kulachenko, A., Barbier, C., *Micro-mechanical modeling of the paper compaction process,* Acta Mechanica, 2021. **232**(9): p. 3701-3722.

61. Mitsoulis, E., *11 - Calendering of polymers*, in *Advances in Polymer Processing*, Thomas S., Weimin Y., 2009, Woodhead Publishing. p. 312-351.

62. Tracey, V. A., *The roll-compaction of metal powders,* Powder Metallurgy, 1969. **12**(24): p. 598-612.

63. Meyer, C., Bockholt, H., Haselrieder, W., Kwade, A., *Characterization of the Calendering Process for Compaction of Electrodes for Lithium-Ion Batteries,* Journal of Materials Processing Technology, 2017. **249**.

64. Li, J., Fleetwood, J., Hawley, W. B., Kays, W., *From Materials to Cell: State-of-the-Art and Prospective Technologies for Lithium-Ion Battery Electrode Processing,* Chemical Reviews, 2022. **122**(1), p. 903-956.

65. Bryntesen, S. N., Strømman, A. H., Tolstorebrov, I., Shearing, P. R., Lamb, J. J., Stokke Burheim, O., *Opportunities for the State-of-the-Art Production of LIB Electrodes—A Review,* Energies, 2021. **14**(5).

66. Kwade, A., Haselrieder, W., Leithoff, R., Modlinger, A., Dietrich, F., Droeder, K., *Current status and challenges for automotive battery production technologies,* Nature Energy, 2018. **3**(4), p. 290-300.

67. Schmidt, D., *Einfluss der Kompaktierung auf die Elektrodenmikrostruktur und elektrochemische Performance bei Lithium-Ionen-Zellen*, 2021, Karlsruhe Institute of Technology.

68. Wang, C., Yi, Y. B., Sastry, A., Shim, J., Striebel, K. A., *Particle Compression and Conductivity in Li-Ion Anodes with Graphite Additives,* J. Electrochem. Soc., 2004. **151**(9), A1489.

69. Li, T., Yuan, X.-Z., Zhang, L., Song, D., Shi, K., Bock, C., *Degradation Mechanisms and Mitigation Strategies of Nickel-Rich NMC-Based Lithium-Ion Batteries,* Electrochemical Energy Reviews, 2020. **3**(1), p. 43-80.

70. Samal, P., Newkirk, J., *Direct Powder Rolling,* 2015, ASM International.

71. Wang, W., Liu, X., Liu, K., *Experimental Research on Force Transmission of Dense Granular Assembly Under Shearing in Taylor–Couette Geometry,* Tribology Letters, 2012. **48**(2), p. 229-236.

72. Herrmann, W., *Das Verdichten von Pulvern zwischen zwei Walzen*. 1973. Weinheim: Verlag Chemie.

73. Duong, H., Shin, J., Yudi, Y. *Dry electrode coating technology*, *48th Power Sources Conference*. 2018.

74.   Johanson, J. R., *A Rolling Theory for Granular Solids,* Journal of Applied Mechanics, 1965. **32**(4), p. 842-848.

75.   vinogradov, G. A., *Method of Calculating the Density and Thickness of Porous Rolled Strip,* Poroshkaya Metallurgiya, 1962. **5**, p. 15-20.

76.   Orowan, E. *The Calculation of Roll Pressure in Hot and Cold Flat Rolling,* Proceedings of the Institution of Mechanical Engineers, 1943. **150**.

77.   Lippmann, H., Mahrenholtz, O., *Walzen*, in *Plastomechanik der Umformung metallischer Werkstoffe: Erster Band*, Lippmann H., Mahrenholtz O., 1967. Springer Berlin Heidelberg, p. 110-187.

78.   Troost, A., *Grundlagen des Bandwalzens*, in *Grundlagen der bildsamen Formgebung*, 1966. Verlag Stahleisen mbH: Düsseldorf.

79.   Mair, K., Frye, K. M., Marone, C., *Influence of grain characteristics on the friction of granular shear zones,* Journal of Geophysical Research: Solid Earth, 2002. **107**(B10), p. ECV 4-1-ECV 4-9.

80.   Tundermann, J. H., *The flow of iron powder during roll compaction,* Powder Metallurgy, 1968. **11**, p. 261-294.

81.   Mueth, D. M., Debregeas, G. F., Karczmar, G. S., Eng, P. J., Nagel, S. R., Jaeger, H. M., *Signatures of granular microstructure in dense shear flows,* Nature, 2000. **406**(6794), p. 385-389.

82.   Kabir, M. A., Lovell, M. R., Higgs, C. F., *Utilizing the Explicit Finite Element Method for Studying Granular Flows,* Tribology Letters, 2008. **29**(2), p. 85-94.

83.   Howell, D., Behringer, R. P., Veje, C., *Stress Fluctuations in a 2D Granular Couette Experiment: A Continuous Transition,* Physical Review Letters, 1999. **82**(26), p. 5241-5244.

84.   Ozaki, S., Matsuura, T., Maegawa, S., *Rate-, state-, and pressure-dependent friction model based on the elastoplastic theory,* Friction, 2020. **8**(4), p. 768-783.

85.   Kraus, M., Lenzen, M., Merklein, M., *Contact pressure-dependent friction characterization by using a single sheet metal compression test,* Wear, 2021. **476**, 203679.

86.   Hurley, R. C., Hall, S. A., Andrade, J. E., Wright, J., *Quantifying Interparticle Forces and Heterogeneity in 3D Granular Materials,* Physical Review Letters, 2016. **117**(9).

87.   Baumgart, F., *Stiffness — an unknown world of mechanical science?,* Injury, 2000. **31**: p. 14-84.

88.   Mosayebi, M., Zarrinkolah, F., Farmanesh, K., *Calculation of stiffness parameters and vibration analysis of a cold rolling mill stand,* The International Journal of Advanced Manufacturing Technology, 2017. **91**.

89.   Mayer, D., Wurba, A.-K., Bold, B., Bernecker, J., Smith, A., Fleischer, J., *Investigation of the Mechanical Behavior of Electrodes after Calendering and Its Influence on Singulation and Cell Performance,* Processes, 2021. **9**, p. 2009.

90.   Binaree, T., Azéma, E., Estrada, N., Renouf, M., Preechawuttipong, I., *Combined effects of contact friction and particle shape on strength properties and microstructure of sheared granular media,* Physical Review E, 2020. **102**(2), 022901.

91.   Feng, J., Wang, L., Chen, Y., Wang, P., Zhang, H., He, X., *PEO based polymer-ceramic hybrid solid electrolytes: a review,* Nano Convergence, 2021. **8**(1), p. 2.

92.   Cheng, X., Xiao, S., Cao, A. S., Hou, M., *A review and analysis of granular shear experiments under low effective stress conditions,* Granular Matter, 2019. **21**(4): p. 104.

93.   Kozlowski, R., Zheng, H., Daniels, K. E., Socolar, J. E. S., *Stick-Slip Dynamics in a Granular Material With Varying Grain Angularity,* Frontiers in Physics, 2022. **10**.

94.   Anthony, J. L., Marone, C., *Influence of particle characteristics on granular friction,* Journal of Geophysical Research: Solid Earth, 2005. **110**(B8).

95. Schulze, D., *Flow properties of bulk solids*, in *Powders and Bulk Solids: Behavior, Characterization, Storage and Flow*, Schulze D., 2008. Springer Berlin Heidelberg, p. 35-74.

96. Hurley, R. C., *Force chains, friction and flow: Behavior of granular media across length scales*, 2016. California Institute of Technology: Pasadena, California.

97. Sun, Q., Jin, F., Liu, J., Zhang, G., *UNDERSTANDING FORCE CHAINS IN DENSE GRANULAR MATERIALS,* International Journal of Modern Physics B, 2010. **24**(29), 5743-5759.

98. Azéma, E., Linero, S., Estrada, N., Lizcano, A., *Shear strength and microstructure of polydisperse packings: The effect of size span and shape of particle size distribution,* Physical Review E, 2017. **96**(2), 022902.

99. Vangla, P., Gali, M., *Influence of Particle Size on the Friction and Interfacial Shear Strength of Sands of Similar Morphology,* Int. J. of Geosynth. and Ground Eng, 2014. **1**: p. 1-6.

100. Di Gianfrancesco, A., *8 - Technologies for chemical analyses, microstructural and inspection investigations*, in *Materials for Ultra-Supercritical and Advanced Ultra-Supercritical Power Plants*, Di Gianfrancesco A., 2017. Woodhead Publishing. p. 197-245.

101. Thomas, T. R., *Characterization of surface roughness,* Precision Engineering, 1981. **3**(2): p. 97-104.

102. Svahn, F., Kassman-Rudolphi, Å., Wallén, E., *The influence of surface roughness on friction and wear of machine element coatings,* Wear, 2003. **254**(11), p. 1092-1098.

103. Li, Y., Otsubo, M., Kuwano, R., Nadimi, S., *Quantitative evaluation of surface roughness for granular materials using Gaussian filter method,* Powder Technology, 2021. **388**, p. 251-260.

104. Zheng, J., He, H., Alimohammadi, H., *Three-dimensional Wadell roundness for particle angularity characterization of granular soils,* Acta Geotechnica, 2021. **16**(1), p. 133-149.

105. Blau, P. J., *Experimental Aspects of Friction Research on the Macroscale*, in *Fundamentals of Tribology and Bridging the Gap Between the Macro- and Micro/Nanoscales*, Bhushan B., 2001, Springer Netherlands: Dordrecht. p. 261-278.

106. Frye, K., Marone, C., *Effect of humidity on granular friction at room temperature,* J. Geophys. Res, 2002. **107**.

107. Bos, B., Peach, C. J., Spiers, C. J., *Frictional-viscous flow of simulated fault gouge caused by the combined effects of phyllosilicates and pressure solution,* Tectonophysics, 2000. **327**(3), p. 173-194.

108. Qi, X., Blizanac, B., DuPasquier, A., Oljaca, M., Li, J., Winter, M., *Understanding the influence of conductive carbon additives surface area on the rate performance of LiFePO4 cathodes for lithium ion batteries,* Carbon, 2013. **64**, p. 334-340.

109. Huai, W., Zhang, C., Wen, S., *Graphite-based solid lubricant for high-temperature lubrication,* Friction, 2020. **9**, p. 1660-1672.

110. Van Krevelen, D. W., Te Nijenhuis, K., *Chapter 1 - Polymer Properties*, in *Properties of Polymers (Fourth Edition)*, Van Krevelen D.W., Te Nijenhuis K., 2009. Elsevier: Amsterdam. p. 3-5.

111. Ferry, J. D., Myers, H. S., *Viscoelastic Properties of Polymers.* Journal of The Electrochemical Society, 1961. **108**(7), p. 142C.

112. Van Krevelen, D. W., Te Nijenhuis, K., *Chapter 6 - Transition Temperatures*, in *Properties of Polymers (Fourth Edition)*, Van Krevelen D.W., Te Nijenhuis K., 2009. Elsevier: Amsterdam. p. 129-188.

113. Polymerdatabase, *Rubbery Plateau and Entanglements*, https://polymerdatabase.com/polymer%20physics/RubberyPlateau.html (visited 04.07.2023)

114. Shaw, M. T., MacKnight, W. J., *Introduction to polymer viscoelasticity*, 2018. John Wiley & Sons.

115. Majeste, J.-C., Montfort, J. P., Allal, A., Marin, G., *Viscoelasticity of low molecular weight polymers and the transition to the entangled regime,* Rheologica Acta, 1998. **37**(5), p. 486-499.
116. *A Basic Introduction to Rheology*, Whitepaper, 2016. Malvern Instruments Worldide
117. Jenike, A. W., *Storage and flow of solids*, 1964: Bulletin No. 123 of the Utah Engineering Experiment Station.
118. Gyulai, A., Bauer, W., Ehrenberg, H., *Dry Electrode Manufacturing in a Calender: The Role of Powder Premixing for Electrode Quality and Electrochemical Performance*, ACS Applied Energy Materials, 2023. **6**(10), p. 5122-5134.
119. Ouyang, J.-H., Li, Y.-F., Zhang, Y.-Z., Wang, Y.-M., Wang, Y.-J. *High-Temperature Solid Lubricants and Self-Lubricating Composites: A Critical Review*, Lubricants, 2022. **10**.
120. Binding, D. M., Couch, M. A., Walters, K., *The pressure dependence of the shear and elongational properties of polymer melts,* Journal of Non-Newtonian Fluid Mechanics, 1998. **79**(2), p. 137-155.
121. Wang, J.-s., Porter, R. S., *On the viscosity-temperature behavior of polymer melts,* Rheologica Acta, 1995. **34**(5), p. 496-503.
122. Pantani, R., Gualtieri, A., Sorrentino, A., Speranza, V., Titomanlio, G., *Effect of Pressure on the Viscosity of Polymers: Measurements and Relevance in the Injection Molding of Thermoplastics*, 6th ESAFORM Conference on Material Forming, 2003.

Publications

Scientific paper

Gyulai, A., Bauer, W., Ehrenberg, H., *Dry Electrode Manufacturing in a Calender: The Role of Powder Premixing for Electrode Quality and Electrochemical Performance*, ACS Applied Energy Materials, 2023. **6**(10), p. 5122-5134.

Conference Poster

Gyulai, A., Bauer, W., Ehrenberg, H., *Dry Processing of Lithium-Ion Cathodes: Powder Preparation and Calendering*, International Battery Production Conference, Braunschweig, 2020.

Gyulai, A., Bauer, W., Ehrenberg, H., *Importance of the Surface Structure of Dry Processed Self-Supported Cathodes*, International Battery Production Conference, Braunschweig, 2021.

Gyulai, A., Bauer, W., Ehrenberg, H., *Influence of Mixing Intensity and Additive Redistribution on the Processibility and Performance of Dry Manufactured Electrodes for Lithium-Ion Batteries*, 21st International Meeting on Lithium Batteries, Sydney, 2022.

Supervised student thesis

Koch, P., Supervised by: Gyulai, A., Bauer, W., *Einfluss der Binderstruktur auf die elektrochemischen und mechanischen Eigenschaften von trockenproduzierten LIB Kathoden*, Vertiefungsarbeit, Institute for Applied Materials – Energy Storage Systems, KIT, 2022.